

Technische Universität München

Max-Planck-Institut für Physik  
Werner-Heisenberg-Institut

**Development of Scintillating Calorimeters for  
Discrimination of Nuclear Recoils and Fully  
Ionizing Events**

Torsten FRANK

Vollständiger Abdruck der von der Fakultät für Physik der Technischen Universität München zur Erlangung des akademischen Grades eines  
Doktors der Naturwissenschaften  
genehmigten Dissertation.

Vorsitzender:	Univ.-Prof. Dr. M. Lindner
Prüfer der Dissertation:	1. Hon.-Prof. Dr. N. Schmitz 2. Univ.-Prof. Dr. L. Oberauer

Die Dissertation wurde am 19.8.2002 bei der Technischen Universität München eingereicht und durch die Fakultät für Physik am 28.10.2002 angenommen.

## Übersicht

Im Rahmen dieser Arbeit wurde ein 300 g Phononen/Licht Detektor für die zweite Phase des CRESST Experiments entwickelt. Diese Detektoren ermöglichen die Unterscheidung von Elektronrückstößen ( $\gamma$ 's &  $\beta$ 's), die den Hauptuntergrund des Experiments ausmachen, und Kernrückstößen (WIMPs & Neutronen) durch die gleichzeitige Messung eines Licht- und eines Phononensignals. Eine Energiedeposition im szintillierenden Absorber erzeugt ein Phononensignal, das von einem direkt auf dem Absorber aufgedampften Phasenübergangsthermometer ausgelesen wird. Zusätzlich wird das Szintillationslicht von einem ähnlichen, aber wesentlich sensitiveren zweiten Tieftemperaturdetektor gemessen. Das Verhältnis der beiden Signale ist charakteristisch für die Art des Ereignisses im Absorber. Da nur ein kleiner Teil der deponierten Energie in Licht umgewandelt wird (wenige Prozent), muss dieses effektiv gesammelt und nachgewiesen werden. Die Aufgabe dieser Doktorarbeit war die Entwicklung von einem ersten Prinzipaufbau [Meu99] zu einem 300 g Prototypen, der die Basis für einen 10 kg Detektor für die zweite Phase von CRESST bildet.

Ein neuer Halter, der für die Sammlung des Szintillationslichts optimiert ist, wurde hierfür entwickelt. Verschiedene Arten und Größen von Lichtdetektoren wurden damit getestet. Das beste Ergebnis wurde mit einem  $3 \times 3 \text{ cm}^2$  (0.4 mm Dicke) großen Siliziumlichtdetektor erzielt. 1.3 % der im Absorber deponierten Energie konnten im Lichtkanal nachgewiesen werden. Verschiedene Versuche wurden durchgeführt, um den Einfluss von möglichen Ortsabhängigkeiten und der Kristallqualität auf die Lichtausbeute zu untersuchen. Eine erzielte Auflösung von 10 % für die beiden Linien einer  $^{60}\text{Co}$  Quelle lässt eine geringe Ortsabhängigkeit erkennen. Der Vergleich verschiedener Kristalle zeigte deutliche Unterschiede in der Lichtausbeute (Faktor 2). Dies kann von einer unterschiedlichen Selbstabsorption oder Szintillationsausbeute der Kristalle herrühren.

Für die Lichtdetektoren wurde ein neues Thermometerdesign mit Phononenkollektoren entwickelt, das sehr kleine und sensitive Thermometer mit einer variablen thermischen Ankopplung ermöglicht. Die beste Schwelle eines Detektors mit  $4 \text{ cm}^2$  Fläche mit diesem Thermometer war 30 eV ( $5\sigma$ ).

Eine Monte Carlo Simulation des kompletten Detektors ermöglicht ein genaues Verständnis der Detektorantwort und erlaubt es, die limitierenden Komponenten zu identifizieren und weiter zu entwickeln. Zusätzlich kann die Simulation verwendet werden, um die Trennschwelle möglicher Detektoren zu berechnen. Basierend auf den bereits für die einzelnen Komponenten gemessenen Daten ist eine 99.7 %ige Trennung bis 13 keV möglich. Verbesserungen in naher Zukunft können sogar eine Trennung bis 9 keV ermöglichen. Diese Schwelle ist bereits unter der bei der Planung angenommenen [pro01] 99.7 %igen Trennung oberhalb von 15 keV.

Erste Tests der Detektoren am Gran Sasso konnten durchgeführt werden. Der Untergrund vor Unterdrückung lag hierbei bei ca. 10 Ereignissen/kg/keV/Tag.

## Summary

This work reports on the development of a 300 g scintillating calorimeter for the second phase of the CRESST cryogenic dark matter search experiment. These calorimeters can discriminate between electronic recoils ( $\gamma$ 's &  $\beta$ 's), that cause the main background in the experiment, and nuclear recoils (WIMPs & neutrons) by a simultaneous measurement of a phonon and scintillation light signal. The sensitivity for a possible WIMP signal can be drastically increased with this technique. An energy deposit in the scintillating absorber leads to a phonon signal that is read out via a superconducting phase transition thermometer directly on the absorber. Additionally the interaction in the crystal produces some scintillation light that is detected with a second very sensitive low temperature detector of the same type. The ratio of scintillation signal to phonon signal is characteristic for the type of interaction in the absorber. The challenge in such a type of detector is the small amount of light generated (few % of the deposited energy). To achieve a good discrimination down to low energies this light has to be efficiently collected and detected. In this work a 6 g proof-of-principle detector [Meu99] was scaled up to a full 300 g prototype that will be used as a basic unit for the CRESST II detector with a total mass of 10 kg.

A new holder with a highly reflective inner surface was developed for this new type of detector to optimize the light collection. Different sizes and types of light detectors were investigated. The best result was achieved with a  $3 \times 3 \text{ cm}^2$  (0.4 mm thick) silicon light detector. It detected 1.3 % of the deposited energy. Various investigations were made with this module to check the influence of possible spatial dependencies and the crystal quality on the light yield. The resolution of the two lines of a  $^{60}\text{Co}$  source was 10 % in the light channel, indicating no significant spatial dependence. The comparison of different crystals showed up to a factor of two difference in light yield. This is attributed to a difference in the self absorption and scintillation efficiency of the crystals.

For the light detectors a new thermometer design with phonon collectors was developed that allows to build very small and sensitive thermometers with adjustable thermal coupling. The best threshold achieved with a detector ( $4 \text{ cm}^2$  surface area) equipped with such a thermometer was 30 eV ( $5\sigma$ ).

A Monte Carlo simulation of the full detector module was programmed to gain a better understanding of the detector and to identify the factors that limit its performance. Future improvements can be based on these results. Additionally the simulation can be used to evaluate the possible discrimination threshold of the detector. Based on the performances already shown for individual parts, a 99.7 % discrimination down to 13 keV seems possible at the moment with a potential of 9 keV in the future. This is better than the proposed goal of 99.7 % discrimination down to 15 keV [pro01].

Some first tests of the complete module were done at Gran Sasso. The measured background before discrimination at 10 keV was  $\approx 10$  counts/kg/keV/day.

# Contents

Übersicht . . . . .	i
Summary . . . . .	ii
<b>1 Introduction</b>	<b>1</b>
1.1 Dark Matter . . . . .	1
1.1.1 Indirect Evidence . . . . .	1
1.1.2 Non-baryonic Candidates . . . . .	2
1.1.3 WIMP Direct Detection . . . . .	4
1.2 The CRESST Experiment . . . . .	5
1.3 CRESST Phase II . . . . .	7
<b>2 Detector Principles</b>	<b>11</b>
2.1 Cryogenic Detectors . . . . .	12
2.1.1 Basics . . . . .	12
2.1.2 Readout . . . . .	13
2.1.3 Noise . . . . .	16
2.1.4 Heat Capacities . . . . .	18
2.2 Detector model . . . . .	20
2.2.1 Phonon Physics . . . . .	20
2.2.2 Thermal Coupling . . . . .	22
2.2.3 Calorimeter Model . . . . .	25
2.3 Phonon Collectors . . . . .	28
2.4 Scintillation & Event Discrimination . . . . .	30
<b>3 Scintillating Detector Module</b>	<b>33</b>
3.1 Light Detector . . . . .	33
3.1.1 Substrates . . . . .	35
3.1.2 Film Geometry . . . . .	35
3.2 Phonon Detector . . . . .	37
3.3 Holder . . . . .	38
3.3.1 Requirements . . . . .	39
3.3.2 Design . . . . .	44
<b>4 Fabrication &amp; Experimental Techniques</b>	<b>47</b>

4.1	Fabrication of Detectors . . . . .	47
4.1.1	Evaporation of Films . . . . .	48
4.1.2	Structuring of Detectors . . . . .	48
4.1.3	Absorption Layers . . . . .	53
4.2	Setup in Cryostat . . . . .	56
4.2.1	Cryostat & Data Acquisition System . . . . .	57
4.2.2	Holders & Sources . . . . .	62
<b>5</b>	<b>Results</b>	<b>65</b>
5.1	Light Collection . . . . .	65
5.1.1	Trapped light . . . . .	65
5.1.2	Reflector . . . . .	67
5.1.3	Absorption . . . . .	67
5.2	Light Detectors . . . . .	70
5.2.1	Uniformity . . . . .	71
5.2.2	Threshold . . . . .	72
5.3	Phonon & Light . . . . .	83
5.3.1	Coincident Measurements in Munich . . . . .	84
5.3.2	Measurements at Gran Sasso . . . . .	86
<b>6</b>	<b>Simulation</b>	<b>91</b>
6.1	Detector Simulation & Possible Performance . . . . .	91
6.1.1	Geometry . . . . .	91
6.1.2	Parameters . . . . .	92
6.1.3	Results . . . . .	95
6.1.4	Performance . . . . .	97
6.1.5	Conclusions . . . . .	101
<b>7</b>	<b>Conclusions &amp; Perspectives</b>	<b>105</b>
7.1	Status . . . . .	105
7.2	Next Steps . . . . .	106
7.3	Future . . . . .	107
	<b>Bibliography</b>	<b>107</b>
	<b>Danksagung</b>	<b>115</b>

# Chapter 1

## Introduction

### 1.1 Dark Matter

The question of what makes up the world we are living in is probably as old as mankind itself. And usually the things that we see at first glance are not the whole truth. In astronomy this became clear in the early stages of extragalactic observations. The kinematics of galaxy cluster dynamics suggested that the dynamic mass involved is far greater than the observable luminous mass [Zwi33]. Until now more and more evidence, the most prominent being the flat rotation curves of galaxies, indicates that there is far more matter in the universe than is visible, the Dark Matter. Later when sufficiently accurate models of big bang nucleosynthesis (BBN) allowed a precise calculation of the expected baryon density in the universe ([Sar96, Sch98, Oli97]) it became apparent that the lower limit for the baryonic matter in the universe is indeed more than the luminous matter, but still the total amount of matter needed on galaxy scales and above is larger than the upper limit of baryonic matter allowed by BBN.

#### 1.1.1 Indirect Evidence

The contribution of a given population or species of mass density  $\rho$  to the cosmic density is usually expressed by the parameter  $\Omega = \rho/\rho_c$  in units of the “critical density” of the universe  $\rho_c = 3H^2/8\pi G = 1.88 \cdot 10^{-29} h^2 \text{ g cm}^{-3} = 1.05 \cdot 10^{-5} h^2 \text{ GeV cm}^{-3}$ .  $H$  is the Hubble expansion parameter,  $G$  the gravitational constant and  $h = H_0/100 \text{ km s}^{-1} \text{ Mpc}^{-1}$  the scaled value of the present Hubble parameter (Hubble constant)  $H_0$ . The present value from observational determination is  $h = 0.65 \pm 0.15$  [Ber00]. The spatial cosmic geometry is Euclidean (flat universe) for  $\Omega = 1$ . For  $\Omega$  smaller/bigger than 1 it has a negative/positive spatial curvature (open/closed universe).

The observations and theoretical models<sup>1</sup> favour a value of  $\Omega = 1$  [Ber00]. The mechanism of inflation, developed by [Gut81, Lin82, Alb82] to solve the age and horizon problem of the universe [Ber00], even predicts a value of  $\Omega = 1$ .

Until a couple of years ago the theoretically favoured model was a universe where matter contributes 100 % to the total density ( $\Omega = \Omega_M = 1$ ). But observations from supernova explosions indicated a second contribution to the total density, the cosmological constant  $\Lambda$  ( $\Omega = \Omega_M + \Omega_\Lambda = 1$ ) [Bah99]. Recent observations of the cosmic microwave background (CMB) [Sto01, Net02, Jaf01] support this picture. The CMB data suggest a universe with  $\Omega_M = 0.3 \pm 0.2$  and  $\Omega_\Lambda = 0.7 \pm 0.2$ .

However a matter density of  $\Omega_M = 0.3$  is far more than allowed by BBN. Therefore baryonic matter can not be the only contribution to the matter density in our universe. The majority is of, not yet discovered, non-baryonic nature. This non-baryonic particles are usually called Dark Matter. Depending on their velocity at the time when they decoupled from radiation in the early universe one distinguishes two different kinds of dark matter particles. Particles that were still relativistic at that moment of decoupling are called hot dark matter (HDM), candidates with non-relativistic speeds cold dark matter (CDM).

The distinction between HDM and CDM is important for the structure formation in the universe. To explain the today observed distribution of visible matter both types of dark matter must be present, with CDM probably being dominant [Raf97].

For a review on the problem of dark matter see for example [Raf97, Ber00, GB99].

### 1.1.2 Non-baryonic Candidates

Although the existence of non-baryonic dark matter is generally accepted, its nature remains one of the most intriguing questions in contemporary astro and particle physics. There are a couple of ‘well motivated’ (particle physics motivated) candidates like neutrinos, axions and WIMPs (Weakly Interacting Massive Particles).

#### Neutrinos

Of many proposed candidates neutrinos are the only non-baryonic dark matter candidates that, at the present time, are known to exist. In the standard model of particle physics neutrinos are massless. But results from the Super Kamiokande detector and recent results from the SNO collaboration [Fuk98, Ahm02] indicate

---

<sup>1</sup>Any value different from 1 would change rapidly during the evolution of the universe. If there is nothing special about the present moment, the canonical assumption for  $\Omega$  is 1.

a finite mass  $m_\nu$  for neutrinos. In order to give a cosmologically interesting contribution to the mass density  $\Omega_M$ , the neutrino mass  $m_\nu$  must be in the range of 1–50 eV [Ber00]. Heavier neutrinos would lead to  $\Omega_M > 1$  and thus overclose the universe, unless  $m_\nu > 3$  GeV. In this case their relic abundance would be low enough and they could act as CDM. But the upper mass limits for the three<sup>2</sup> known neutrinos are well below 3 GeV, and heavier Dirac neutrinos are excluded by direct detection [Cal88] data up to the TeV range. Although a mass of 1–2 eV is not yet strictly excluded by experimental data, the ‘natural’ scale as suggested from the measured mass differences  $\Delta m^2$  is below 1 eV. In this regime neutrinos only give a small, dynamically not important contribution to  $\Omega_M$ .

In the case of neutrinos being the only dark matter in the universe an important lower bound for the mass comes from the Tremaine-Gunn limit [Tre79]. It uses a phase space argument to obtain a lower limit. For dwarf galaxies this mass is a few 100 eV [Sal97], which is not compatible with the before mentioned mass range. Therefore neutrinos can not be the only dark matter on all scales. But even if neutrinos do not contribute the main part of the dark matter, they may still play an important role for structure formation in a CDM dominated universe [Raf97].

## Axions

The axion was postulated [Pec77] to explain the absence of CP violation in strong interactions of quantum chromodynamics. Its mass  $m_a$  is constrained by laboratory experiments and astrophysical arguments to be below 0.01 eV [Mur98]. As they are weakly interacting and non-relativistic since their appearance in the universe they are a CDM candidate. There is considerable uncertainty in the relation between mass and the relic density of axions. If they exist they could well form a considerable part of the dark matter. Two experiments are presently looking for axions in our galaxy and can probe much of the interesting parameter space in the next few years [Hag98, Oga96].

## WIMPs

WIMP is a general term for a class of particles that show weak interaction with ordinary matter and have a mass in the range of 1 GeV up to a few TeV [Ber00]. The most promising candidate is the lightest supersymmetric particle, the neutralino [Ell84]. Supersymmetric particles differ from normal particles by a quantum number called R-parity. If R-parity is conserved the lightest supersymmetric particle cannot decay, and a relic density would still be around today. This relic density

---

<sup>2</sup>From the decay width of the  $Z^0$ -boson the number of families is restricted to three up to a mass of  $m_{Z^0}/2 \approx 46$  GeV.



could be in the interesting range for CDM if the breaking of supersymmetry was related to the electro-weak scale [Ber00].

### 1.1.3 WIMP Direct Detection

Obviously direct detection of WIMPS, if they exist, is only possible in our own galaxy. Luckily there is strong observational evidence for dark matter in spiral galaxies like our Milky Way, with WIMPs being gravitationally bound to the galaxy and forming a halo around it. Their velocities should obey a Maxwellian distribution with a most probable velocity  $\bar{v}_W = 270$  km/s and a cutoff given by the escape velocity of the Milky Way ( $\approx 650$  km/s). From the measured rotational curve a local density of  $\rho_0 = 0.3$  (GeV/c<sup>2</sup>)/cm<sup>3</sup> can be derived [Raf97, Ber00]. The flux of dark matter particles on earth therefore is

$$\Phi = \frac{\rho_0 \langle v_W \rangle}{m_W} = 10^7 \frac{\text{GeV}/c^2}{m_W} \frac{1}{\text{cm}^2 \text{s}}, \quad (1.1)$$

with  $m_W$  being the WIMP mass and  $\langle v_W \rangle$  an average velocity.

Direct detection is based on the elastic scattering of WIMPs off the nuclei of the target material. If  $m_r = m_W m_N / (m_W + m_N)$  is the reduced mass of the WIMP-nucleus system ( $m_N$  = mass of nucleus), the laboratory energy  $E_r$  of the recoiling nucleus is

$$E_r = \frac{m_r^2}{m_N} v_W^2 (1 - \cos \theta), \quad (1.2)$$

where  $\theta$  is the scattering angle in the centre of mass system. The recoil energy  $E_r$  varies with the scattering angle  $\theta$  and is in the order of keV for WIMP masses of a few GeV/c<sup>2</sup>. This recoil energy already is at the sensitivity limit of conventional semiconductor or scintillation detector technology, especially as the event rate rapidly decreases towards higher energies.

The expected event rate  $R$  is determined by the incoming WIMP flux and the cross section  $\sigma$  for elastic WIMP-nuclei scattering. The cross section  $\sigma$  is model dependent and varies over many orders of magnitude. Typical rates are  $R \leq 1$  event/kg/day. All direct detection experiments (CDMS, DAMA, CRESST, Edelweiss, IGEX, Rosebud, UKDM) therefore are low background experiments usually situated at a deep underground site, well shielded from any radiation.

Despite the low energy transfers, it was the DAMA collaboration, using a conventional, segmented  $\simeq 100$  kg NaI(Tl) detector set-up, who in 1999 reported a positive WIMP signal [Ber99] (see figure 1.1). They derived a most probable WIMP mass of  $m_W \sim 60$  GeV with a cross section per nucleon of  $\sigma_{\text{nucleon}} \sim 7.0 \cdot 10^{-6}$  pb. Their signal signature was a  $\simeq 7\%$  annual variation of the detection rate due to the motion of the earth around the sun.

About 1.5 years later the CDMS experiment was able to exclude the DAMA positive evidence at a 75 % confidence level [Abu02]. The detectors used in CDMS are cryogenic detectors based on Germanium and Silicon single crystals. Recently the Edelweiss collaboration, using cryogenic detectors similar to the CDMS germanium detectors, could exclude the DAMA region at a higher confidence level of 99.8 % [Ger02, Ben02].

The important fact to notice is the exposure needed for the different experiments to reach a comparable sensitivity in their results. The DAMA exposure was 19511 kg days, whereas the two cryogenic experiments accumulated an exposure of  $\sim 10$  kg days each. This vast difference is due to the background suppression possible with cryogenic detectors. The only signature to distinguish the WIMP signal from background in the DAMA detector is the small annual modulation of the rate, whereas cryogenic detectors can actively reduce the background by discrimination. This and the possible very low threshold make cryogenic detectors particularly suited for WIMP direct detection. The most stringent limits on WIMP masses and cross sections at present are set by cryogenic detector setups [Abu02, Ben02].

## 1.2 The CRESST Experiment

The aim of the CRESST<sup>3</sup> experiment is a direct detection of WIMP dark matter using cryogenic detectors. The experiment is located at the Gran Sasso Underground Laboratory in Italy inside a special low background environment. The Gran Sasso Laboratory is situated inside the Gran Sasso mountain with a minimum rock overburden of 1400 m (3150 m.w.e.<sup>4</sup>). This rock overburden reduces the cosmic muon flux by about 6 orders of magnitude to  $\approx 1$  muon per square metre and hour. The CRESST experiment uses a specially designed cryostat with a separated cold box (see figure 1.2) housing the detectors. The rather complicated design is necessary to block any line of sight between the cryostat and not radiopure materials used for its construction, and the detectors in the cold box. The cold box is made out of low background copper. Around it additional copper and lead shields screen the detectors from surrounding radioactivity. The shields are enclosed in a gas-tight radon box. The entire cryostat is situated in a clean room which again is inside a Faraday cage.

The first phase of the CRESST experiment used four sapphire crystals of 262 g each, equipped with tungsten superconducting thermometers, as detectors. A threshold as low as 580 eV and a background of 0.73 counts/keV/kg/day (15–25 keV) was achieved with this setup. Figure 1.1 shows the exclusion plot for spin

---

<sup>3</sup>Cryogenic Rare Event Search with Superconducting Thermometers

<sup>4</sup>metre water equivalent

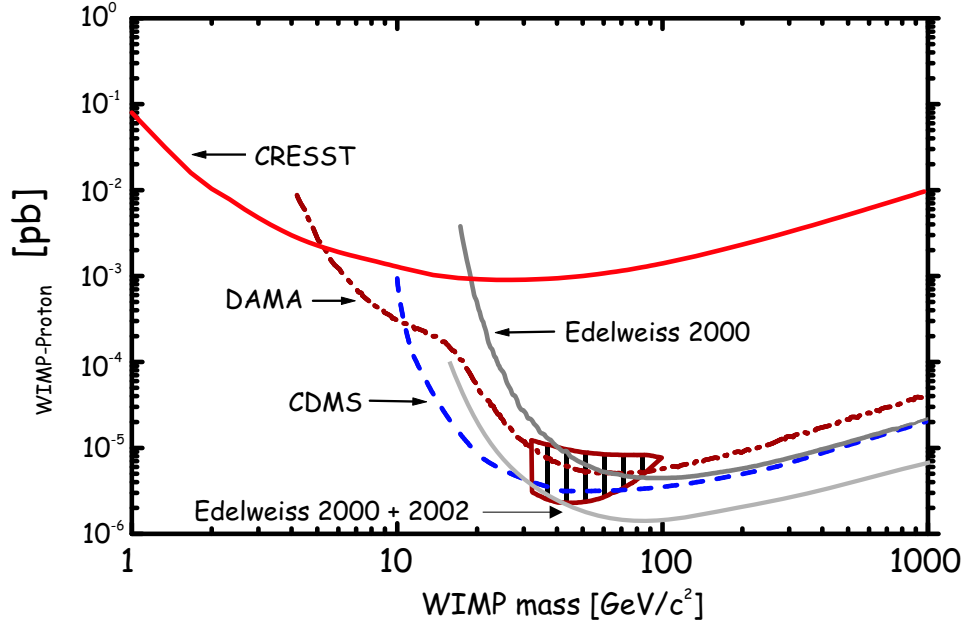


Figure 1.1: Exclusion limits of several experiments for spin independent interaction. The closed contour indicates the DAMA positive evidence. As the mass and the cross section of the WIMPs are not known the exclusion curves are plotted in the mass/cross section plane. The parameters above the indicated lines are excluded by the experiments. To be able to compare experiments using different absorbers, the cross section is normalized to ‘per proton’.

independent (coherent) interaction derived from these results. The plot shows the result from CRESST I and the before mentioned other direct search experiments. The contour represents the DAMA positive evidence. Due to its low threshold the CRESST experiment sets the best limits for WIMP masses below 5 GeV. A special focus of CRESST I was the detection of WIMPs with spin dependent interaction. Plot 1.3 shows the limit in comparison with other experiments. Again CRESST sets the best limits below a WIMP mass of about 5 GeV.

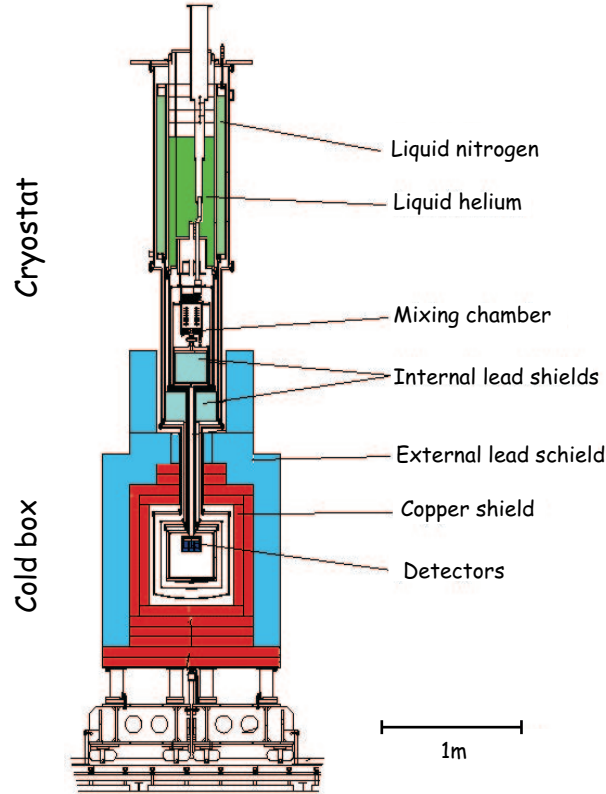


Figure 1.2: The CRESST cryostat at the Gran Sasso Underground Laboratory

### 1.3 CRESST Phase II

The reached sensitivity of CRESST phase I for a possible WIMP signal is limited by the residual background in the detector. Big improvements are not possible with passive shielding alone, but require the possibility to actively distinguish between radioactive background and a possible WIMP interaction in the absorber.

The remaining background is dominated by  $\beta$  and  $\gamma$  emissions from radioactive contaminants inside and in the surrounding of the detectors. These interact via

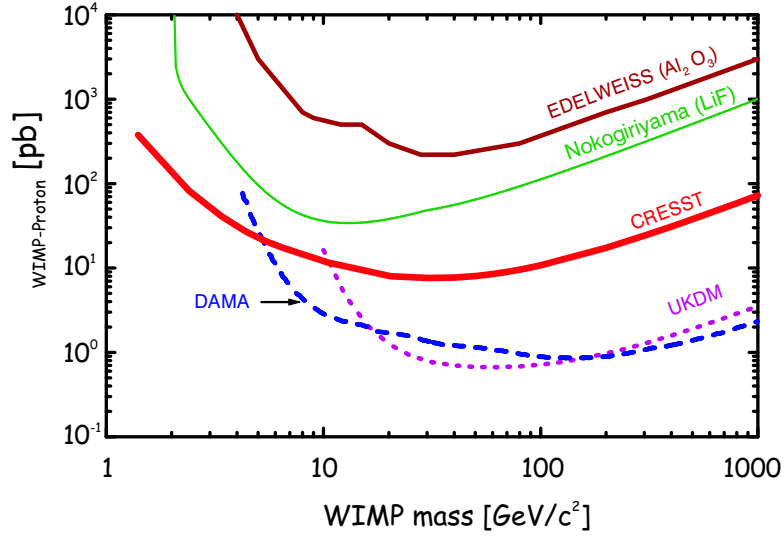


Figure 1.3: Exclusion limits of CRESST I and other experiments for spin dependent interaction.

electron recoil in the detector. WIMPs and neutrons on the other hand lead to nuclear recoils. If the detector is capable of distinguishing these two different types of interaction a large part of the background can be rejected. Together with the usual passive shielding and an additional neutron shield dramatic improvements in sensitivity can be achieved in this way.

Other dark matter search experiments already use the simultaneous detection of a phonon and charge signal for a Si or Ge single crystal target [Abu02, Ger02], and could thereby improve their sensitivity. However this particular technique has one major drawback. Surface near events may lead to an incomplete charge collection, resulting in a missidentification of events. The CRESST collaboration has therefore chosen to exploit a different technique to identify the event type.

In a scintillating crystal a particle interaction in general produces phonons and a small (few %) amount of scintillation light. Nuclear recoils, however, produce much less light than electron recoils of the same energy. By measuring the ratio of scintillation light and phonon signal one can identify the type of interaction. Exploitation of this technique for new high performance particle detectors, especially for dark matter experiments, was first proposed by [GM88]. The CRESST-II detectors will use this mechanism to increase their sensitivity.

A first proof-of-principle detector with a  $\text{CaWO}_4$  scintillating crystal was developed [Meu99]. In this detector a large calorimeter with a scintillating absorber is placed close to a second much smaller calorimeter which detects the scintillation light. Figure 1.4 shows the spectrum obtained with the detector when irradiating

it with  $\beta$ ,  $\gamma$  and neutron sources. Surface near events ( $\beta$ 's) showed the same light output as interactions in the bulk ( $\gamma$ 's) [Meu99]. Another advantage of this type

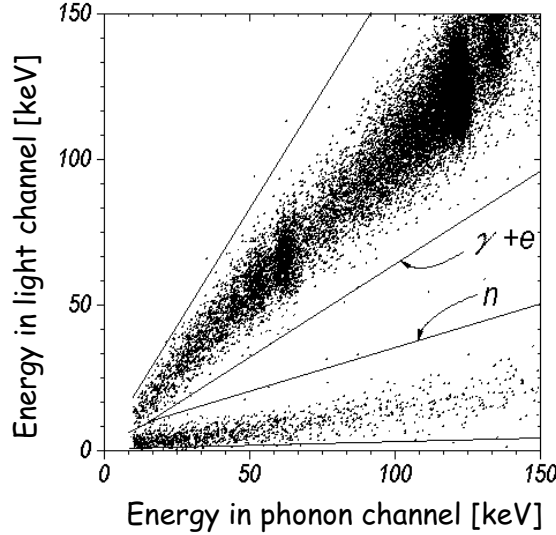


Figure 1.4: Scatter plot of the pulse height in the phonon detector versus the pulse height in the light detector for the proof-of-principle detector. The events group in two clearly separated bands for electron and nuclear recoils. The quenching for nuclear recoils with respect to electron recoils was 7.4. From these experiments a rejection for  $\gamma$  and  $\beta$  events of better than 99.7 % for energies above 15 keV could be derived.

of detector, besides the absence of surface effects, is the wider choice of materials. Whereas the phonon/charge discrimination is restricted to semiconducting materials (Si & Ge), the phonon/light technique works with many different scintillating crystals ( $\text{CaWO}_4$ , BGO,  $\text{BaF}_2$ ,  $\text{PbWO}_4$  ...).

The big challenge in this kind of detector is the small amount of light that has to be detected. Only a few percent (for  $\gamma$  interactions) of the total energy deposited are converted into scintillation light. The light detector therefore has to be roughly a factor of 100 more sensitive than the phonon detector to reach the same threshold.

The aim of this work was to proceed from the 6 g proof-of-principle detector to a 300 g prototype module that can be the building block of a segmented 10 kg detector which is projected for the second phase of the CRESST experiment. The main focus was hereby on the light detection, as this is the bottleneck for a detector with a big scintillating absorber. The final goal was a 300 g module with a discrimination of better than 99.7 % down to energies of 15 keV, similar to the

already shown performance of the small 6 g detector.

## Chapter 2

### Detector Principles

The low temperature detectors used in this work consist of three basic parts, an absorber, a thermometer and a coupling to the heat bath (see figure 2.1). An interaction in the absorber deposits an energy  $\Delta E$  in the absorber and leads to a temperature increase  $\Delta T$ , that is measured by the thermometer. The energy flows out of the system via the link to the heat bath and the system relaxes back to its equilibrium state. In a strictly calorimetric model the temperature increase can be expressed by  $\Delta T = \Delta E/C$ , where  $C$  is the heat capacity of the detector (absorber+thermometer). The temperature increase is thus a direct measure for the deposited energy.

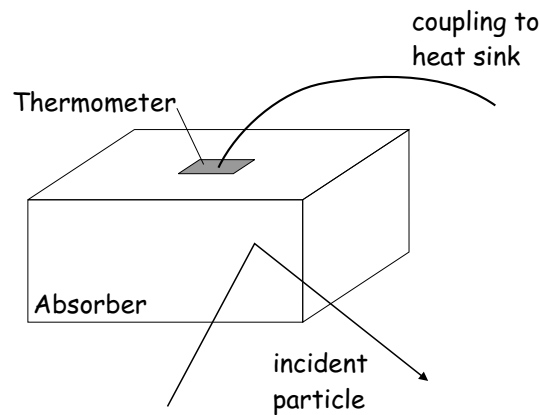


Figure 2.1: Schematic view of calorimetric detector



## 2.1 Cryogenic Detectors

### 2.1.1 Basics

A main part of the detectors developed for CRESST is the superconducting phase transition thermometer (SPT). The SPT is a thin (typically  $0.5\text{--}2\text{ k}\text{\AA}$ ) superconducting tungsten film with an area of a few  $\text{mm}^2$ . It is stabilized in the normal to superconducting phase transition. The transition temperature of bulk tungsten is at  $15\text{ mK}$ . Figure 2.2 shows a typical measured transition curve. For the W-films evaporated on sapphire crystals the transitions usually occur at

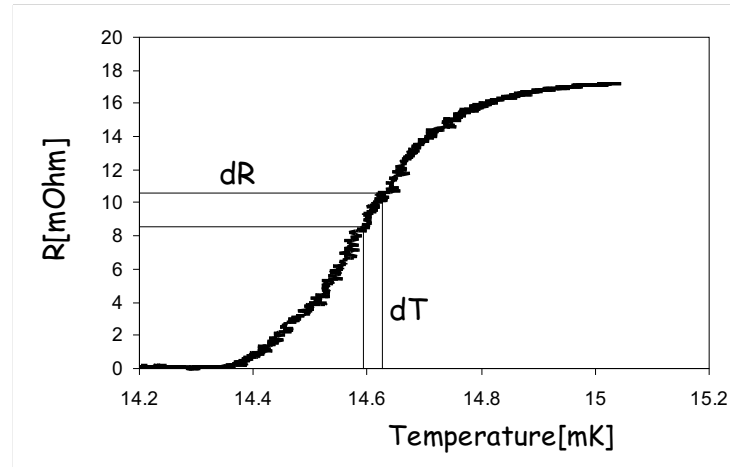


Figure 2.2: Typical measured transition curve of a tungsten film on a sapphire substrate

$10\text{--}20\text{ mK}$ . The typical width of the transition is  $1\text{ mK}^{-1}$  or below. The normal conducting resistance of the film depends on the geometry and ranges from  $10\text{--}100\text{ m}\Omega$ . In the region of the transition the resistance depends strongly on the temperature. A small temperature increase leads to a relatively large increase of resistance. This can be transformed into a current signal that can be read out (see below) with a **S**uperconducting **Q**uantum **I**nterference **D**evice (SQUID [Lou74]).

After an energy deposition one expects an (instantaneous) increase of temperature  $\Delta T = \Delta E/C$ . The coupling to the heat bath leads to an exponential decay back to the equilibrium state. The time constant of the decay  $\tau = C/G$  is given by the heat capacity  $C$  of the system and the thermal coupling strength  $G$  to the heat bath. In figure 2.3 a typical signal (as measured with a SQUID) of a low temperature calorimeter after the absorption of a  $6\text{ keV}$  X-ray is shown.

---

<sup>1</sup>This holds if the transition is measured with low currents ( $\leq 1\text{ }\mu\text{A}$ ). Higher currents broaden the observed transition due to self heating and critical current effects in the film.

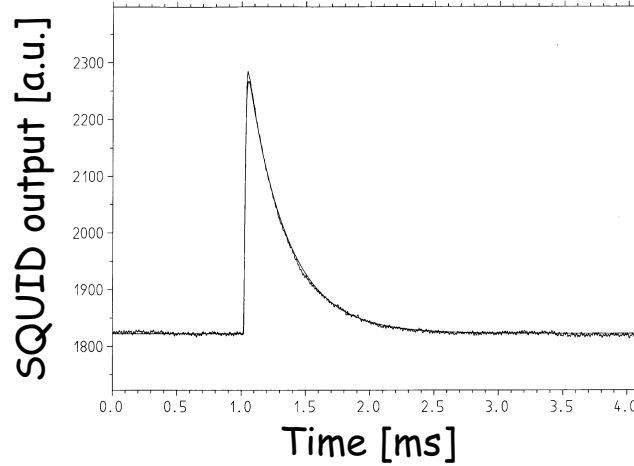


Figure 2.3: Typical pulse of a low temperature calorimeter after the absorption of a 6 keV photon from a  $^{55}\text{Fe}$  source. The event occurred at  $t = 1$  ms. The smooth line is a fit to the pulse. The calorimeter consisted of a sapphire absorber with a tungsten film.

In most cases this simple picture of pulse formation does not match reality. The rise time is not infinitely fast but is limited by several processes in the thermometer and the read out circuit. The decay usually is not a simple exponential, but has two components with different time constants. These are commonly referred to as thermal and non-thermal component. They originate from different phonon processes in the detector. To get a more precise description of the pulse shape two main effects have to be taken into account:

- The absorption of radiation in the absorber leads to a non-equilibrium state of the detector. The signal develops during the subsequent relaxation processes. These processes determine the signal shape.
- At the low operating temperatures the individual parts of the calorimeter are not coupled infinitely well. This leads to different temperatures in the components, which again has a major influence on the signal.

A detailed discussion of these processes and couplings will be given in section 2.2. A model for the calorimeter will be introduced that reproduces the observed signal shapes.

### 2.1.2 Readout

The readout circuit for the detectors (figure 2.4) consists of two parallel branches. On one side there is the thermometer with the temperature dependant resistance

$R_f(T)$ , on the other the shunt resistor  $R_s$  and the SQUID input coil. The resis-

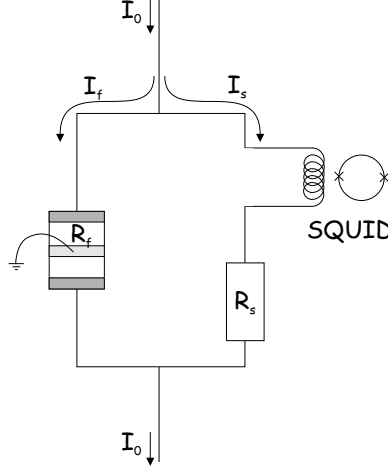


Figure 2.4: Readout circuit

tances of thermometer and shunt are of the same order ( $R_s \leq R_f(T)$ ). For the read out, a constant bias current  $I_0$  is passed through the circuit. It branches according to the ratio of the resistances. The current through the SQUID branch is given by:

$$I_s = I_0 \frac{R_f(T)}{R_f(T) + R_s} \quad (2.1)$$

The increase of the film resistance  $R_f$  after an energy deposit increases the current  $I_s$  on the SQUID side. The input coil transforms the current into a magnetic flux  $\Phi$ . This flux is coupled into the input loop (superconducting ring with two Josephson junctions) of the SQUID. Usually the SQUIDS are operated in a flux locked mode. This means a separate feedback coil is used to keep the flux through the loop constant. This feedback current is the output signal of the SQUID electronics. When the SQUID is operated in a flux locked mode the relation between current  $I_s$  and output voltage  $V_s$  is linear. In this way the SQUID acts as a current meter.

Important for the performance of the detector is the sensitivity  $\delta R_f / \delta E$  (resistance change per energy change) of the thermometer film and the responsivity  $\delta I_s / \delta R_f$  (current change per resistance change) of the readout circuit. The responsivity of the readout can be written as:

$$\frac{\delta I_s}{\delta R_f} = I_0 \frac{R_s}{(R_f + R_s)^2} \quad (2.2)$$

The sensitivity together with the responsivity determines the amplitude of the current signal for a given energy deposit (total sensitivity)  $\delta I_s / \delta E$  in the absorber.

$$\frac{\delta I_s}{\delta E} = \frac{\delta R_f}{\delta E} \cdot \frac{\delta I_s}{\delta R_f} \quad (2.3)$$

The sensitivity of the thermometer is different for every film. It depends on the slope of the transition curve and the heat capacity of the thermometer at the operating point. The sensitivity varies over the transition. It is zero above and below the transition and has one or more maxima in between. The sensitivity not only depends on the position in the transition but also on the read out current. Critical current effects and self heating in the film broaden the transition and decrease the sensitivity at higher currents. For high currents  $I_0$ , however, equation 2.2 shows that the responsivity increases. This means there is a maximum for the total sensitivity.

Besides the optimum operating point  $R_{op}$  and the readout current through the film  $I_F$  one can define the shunt resistance  $R_s$  that gives the maximal responsivity of the readout circuit. For constant  $I_0$  equation 2.2 has a maximum for  $R_s = R_f$ . If one wants to keep the current through the film constant the bias current  $I_0$  has to be increased with decreasing bias resistor:

$$I_0 = I_F \frac{R_f + R_s}{R_s} \quad (2.4)$$

Together with 2.2 this results in

$$\frac{\delta I_s}{\delta R_f} = \frac{I_F}{R_f + R_s}, \quad (2.5)$$

showing that the responsivity improves with lower values of the shunt resistor. Compared with the situation  $R_s = R_f$  a factor of two can be gained for  $R_s \rightarrow 0$ .

Choosing the shunt resistor smaller than the thermometer resistance at the operating point has an additional benefit. The current flowing through the detector causes some resistive heating  $P_f = R_f I_f^2$  in the film. Changes in the resistance, and consequently in the current, due to disturbances or signals, change the dissipated heating power.

$$\begin{aligned} P_f(R_f, I_0) &= R_f \left( \frac{I_0 R_s}{R_f + R_s} \right)^2 \\ \frac{\delta}{\delta R_f} P_f(R_f, I_0) &= \underbrace{\frac{(I_0 R_s)^2}{(R_f + R_s)^3}}_{>0} \underbrace{(R_s - R_f)}_{(*)} \end{aligned} \quad (2.6)$$

For shunt resistors smaller than the film resistance expression  $(*)$  in equation 2.6 is negative. An increasing flux of energy into the thermometer with a consequent temperature/resistance rise of the thermometer leads to a decreased electrical heating in the film and vice versa. This negative feedback also has a self stabilizing effect on the operating point.

In the other case when the bias resistor is larger than the resistance of the thermometer the positive feedback has a destabilizing effect on the detector.

### 2.1.3 Noise

The number that eventually determines the performance (resolution and threshold) of a detector is not the signal height but the ratio of signal amplitude to noise amplitude (signal to noise). In a low temperature detector there are various sources for this noise.

- Fluctuations of the energy content of the calorimeter (Phonon noise)
- Current fluctuations in the readout circuit (Johnson noise)
- SQUID noise
- Temperature fluctuations of the heat bath
- Other noise sources (“excess noise”, external disturbances)

#### Phonon noise

A random energy flow through the weak thermal link to the heat bath leads to fluctuations of the energy content of the calorimeter. This phonon noise gives a physical lower limit for the achievable energy resolution. Assuming poisson statistics for the phonons, the number of phonon modes in the calorimeter ( $C/k_b$ ) and the mean energy per mode ( $k_b T$ ) the mean energy fluctuation  $\Delta E$  [McC93] is

$$\Delta E_{Phonon} = \sqrt{k_B T^2 C} \quad (2.7)$$

$k_B$  ... Boltzmann’s constant

$T$  ... Temperature of heat bath and calorimeter

$C$  ... Heat capacity of calorimeter

For the detector sizes and mK operating temperatures used in this work  $\Delta E$  is below 1 eV for the light detectors or below 100 eV for the phonon channel. This is well below the thresholds of the detectors and can be neglected.

#### Johnson noise

The Johnson noise of a resistor originates from the random scattering of electrons while passing through the resistor. Every scattering dissipates energy. Since this scattering is a random process and the thermal conductance is not infinite, a stochastic change in thermometer temperature and current is created. The spectral current density of Johnson noise is white and is given by [Mat82]

$$N_{Johnson} = \frac{4k_B T}{R} \quad (2.8)$$

$T$  ... Temperature of resistor  
 $R$  ... Resistance

For the readout circuit with two resistors one gets:

$$N_{Johnson} = 4k_B \frac{T_f R_f + T_s R_s}{(R_f + R_s)^2} \quad (2.9)$$

In a read out circuit with a  $50 \text{ m}\Omega$  film and a  $10 \text{ m}\Omega$  shunt resistor at  $15 \text{ mK}$  the Johnson noise generates a mean current fluctuation of about  $3.7 \text{ pA}/\sqrt{\text{Hz}}$ .

### SQUID noise

A SQUID system experiences a noise which is created by the magnetic flux lines in the input coil. The spectral power density of this noise can be assumed white as well. The level depends on the setup. The SQUIDS used for the measurements are commercially available systems from Applied Physics Systems. They have a current noise as low as  $1\text{--}2 \text{ pA}/\sqrt{\text{Hz}}$ . This is of the same order or lower than the Johnson noise. The ‘energy’ this corresponds to depends on the signal height in the individual detector.

### Temperature fluctuations

Temperature fluctuations of the heat bath lead to temperature fluctuations of the operating point. Fast changes of the temperature show up as noise on the detector baseline, whereas slow variations lead to drifts of the operating point. Depending on how strong the sensitivity of the thermometer varies in the region around the operating point this has more or less an effect on the measured pulse height. In a ‘perfect’ detector the transition curve has a constant slope and the sensitivity is (almost) not dependent <sup>2</sup> on the operating point. In a real detector the sensitivity can vary a lot and one has to take care to stabilize the heat bath temperature on a level comparable to the signals in the detector ( $O(\mu\text{K})$ ).

### Other noise sources

Other possible noise sources are external disturbances like vibrations or electrical interferences that reach the detector setup. This excess noise appears as ‘current like’ noises if it couples into the readout circuit or ‘energy like’ if it dissipates

---

<sup>2</sup>Of course the heat capacity of the detector varies with temperature and thus affects the pulse height. Additionally the responsivity of the readout circuit is influenced by the film resistance.

energy in the detector. These noise sources however are not ‘fundamental’ and can be avoided by a proper design of the setup.

Despite all efforts to avoid excess noise some groups [Tie01, Lin01] report noise in their detectors that cannot be explained by the above mentioned fundamental sources. It occurs towards the bottom of the transition. Its origin is not yet clarified. Although no systematic studies of the noise contributions in the CRESST sapphire detectors have been carried out this is compatible with empirical findings from the operation of various detectors. The best operating points (with respect of signal to noise) are usually not at the bottom of the transition where the relative resistance changes and the responsivity are large (equation 2.5), but typically at the top [Sis99, Mei99].

It is important to notice the different manifestations of the noises. Current like noise (Johnson & SQUID noise) gets less severe as the detector gets more sensitive. It is a constant ‘background’ against which the signal has to compete. The bigger the signals the more they rise above this noise. ‘Energy like’ noise (Phonon noise) on the other hand originates in the detector itself and is amplified in the same way as the signals when the detector gets more sensitive.

The limitations for the detectors at the moment (especially for the light detectors) seem to arise from current like noise. Therefore a higher sensitivity of the detectors can increase the performance. To get an understanding of how the sensitivity can be improved the next sections will discuss all parts of the detector and the signal formation process in the calorimeter in detail.

### 2.1.4 Heat Capacities

The heat capacities of the different parts play an important role for low temperature calorimeters. They define the amplitude of the temperature signal  $\Delta T$  that can be obtained. The contributions of dielectrics, semiconductors, metals and superconductors to the total heat capacity of the calorimeters will be shown.

#### Dielectrics & semiconductors

In non-magnetic dielectrics the heat capacity is dominated by the lattice specific heat or the excited phonon states. At low temperatures it is well described by the Debye-model [Deb12]:

$$c_{ph} = \frac{12\pi^4}{5} n_a k_B \left( \frac{T}{\Theta_D} \right)^3 = AT^3 \quad (2.10)$$

$c_{ph}$  ... Lattice specific heat

$n_a$  ... Lattice atoms per mol  
 $\Theta_D$  ... Debye temperature  
 $A$  ... Material constant

There is no electronic contribution to the heat capacity due to the lack of free electrons. The same formula is valid for very pure semiconductors at low temperatures ( $T < 1$  K), when all the conducting electrons are frozen out. They are dominated by their lattice specific heat as well.

Due to the  $T^3$  dependence the phononic heat capacity is very small at low temperatures. This makes dielectrics and semiconductors suitable absorbers for large calorimeters.

### Metals

The thermometers of the detectors are metal films. In metals the electronic part of the heat capacity dominates at low temperatures:

$$c_e = \frac{\pi^2}{2} n_e k_B \frac{T}{T_F} = \gamma T \quad (2.11)$$

$n_e$  = Conducting  $e^-$  per mol  
 $T_F$  = Fermi temperature  
 $\gamma$  = Material specific constant

The electronic specific heat depends linearly on the temperature. The phononic part exists in metals as well, but is negligible at mK temperatures.

For a superconductor the specific heat has a discontinuity at the critical temperature  $T_c$ . It increases to the 2.43 fold of the normal conducting value [Tin79]. In reality the phase transitions of the films have a finite width and one can use a linear approximation for the heat capacity in the transition. Taking the ratio of actual resistance  $R_{op}$  to normal conducting resistance  $R_n$  as a measure for the fraction of the film in the superconducting phase, the heat capacity  $C_{op}$  at the operating point can be written as:

$$C_{op} = C_e \left( 2.43 - 1.43 \frac{R_{op}}{R_n} \right) \quad (2.12)$$

At temperatures well below  $T_c$  the heat capacity of a superconductor decreases exponentially. Below  $T_c/2$  it can be described with the BCS-theory by:

$$c_e = 1.34 \gamma T_c \left( \frac{\Delta}{k_B T} \right)^{\frac{3}{2}} \exp \left( \frac{-\Delta}{k_B T} \right) \quad (2.13)$$



$\Delta$  ... Superconducting energy gap

For temperatures below  $T_c/10$  the electronic part of the heat capacity in a superconductor can be neglected and the small lattice specific heat capacity (equation 2.10) dominates. This vanishing of the electronic heat capacity is important for the concept of the phonon collectors described later on. Table 2.1 compiles the values for  $T_c$ ,  $T_F$  and  $\Theta_D$  of the materials commonly used in this work.

		Tungsten	Gold	Aluminium
$T_c$	[mK]	15	–	1180
$T_F$	[K]	27000	63900	134900
$\Theta_D$	[K]	400	165	428
$\gamma$	[mJ mol <sup>-1</sup> K <sup>-2</sup> ]	1.0	0.729	1.356

		Sapphire	Silicon	CaWO <sub>4</sub>
$\Theta_D$	[K]	1041	645	247*

Table 2.1: Constants for the used materials. Values from [Kit88, Kop89, Tri73], \* calculated from elastic constants [Prö02].

## 2.2 Detector model

In the following section the processes how the excitations (phonons) generated after an energy deposition in the absorber are transformed into a signal will be discussed. The first section deals with the propagation of the phonons in the absorber and the transmission into the thermometer, where they interact with the electrons and lead to a temperature rise of the electron system that can be detected via the resistance increase of the thermometer. In the next section a theoretical model of the detector will be presented, that explains and reproduces the observed pulse shapes. The two different decay times are attributed to different processes in the detector. The fast component is due to the absorption of high frequency phonons in the thermometer itself, whereas the slow component represents the temperature increase of the absorber.

### 2.2.1 Phonon Physics

The absorption of ionizing radiation as well as nuclear recoils, caused by WIMPs or neutrons, in the dielectric absorber, create high frequency phonons ( $O(\text{THz})$ ). Nuclear recoils directly produce a broad frequency distribution of non-thermal

acoustic phonons via the local deformation of the crystal lattice. Ionizing radiation first generates high energetic electrons in the absorber. They spread their energy with the help of electron-electron coupling. Once the energy of the excited electrons is lower than twice the energy gap in the dielectric, this process is impossible and the electrons relax within 10 ps to the band edge through emission of optical phonons or photons<sup>3</sup>. The optical phonons decay very rapidly ( $O(100\text{ ps})$ ) into acoustical phonons of about half the Debye frequency  $\nu_D$  (for sapphire  $\nu_D = k_B\Theta_D/h \approx 21.7\text{ THz}$ ) [Mar80].

After  $\approx 100\text{ ps}$  the energy is transferred into high frequency phonons. Both processes, nuclear recoils and ionizing events, produce acoustic phonons, but with a different phonon spectrum. Recoils result in a broad distribution, whereas ionizing interactions lead to almost monoenergetic phonons. These phonon populations are not in an equilibrium state and will start to decay towards a thermal distribution.

There are three polarizations of acoustic phonons, two transverse and one longitudinal mode. Transversal acoustic phonons occupy the lowest energetic branch. They do not decay in an ideal isotropic crystal. But even in real anisotropic crystals their decay rate can be neglected [Tam84]. Longitudinal acoustical phonons have two<sup>4</sup> main decay channels:

- two transversal acoustical phonons (dominant)
- one longitudinal and one transversal acoustical phonon

The decay rate is strongly frequency dependent. For an isotropic medium this rate can be written as [Tam85a, Mar90]:

$$\Gamma_{dec} = \gamma_{dec} \omega_D \left( \frac{\omega}{\omega_D} \right)^5 \quad (2.14)$$

$$\begin{aligned} \omega & \dots \text{Phonon frequency} \\ \omega_D & \dots \text{Debye frequency } \omega_D = 2\pi\nu_D \\ \gamma_{dec} & \dots \text{Material constant} \end{aligned}$$

Besides the decay of longitudinal phonons, all phonons can scatter elastically on isotopes in the crystal lattice (<sup>16</sup>O, <sup>17</sup>O and <sup>18</sup>O for sapphire). This scattering rate can be written as [Mar90]:

$$\Gamma_{iso} = \eta_{iso} \omega_D \left( \frac{\omega}{\omega_D} \right)^4 \quad (2.15)$$

---

<sup>3</sup>This scintillation process is very important for the concept of event discrimination and will be treated in the section 2.4.

<sup>4</sup>A third decay channel into two longitudinal phonons is possible but strongly suppressed [Tam85a].

$\omega$	...	Phonon frequency
$\eta_{dec}$	...	Material constant

The scattering on crystal imperfections adds to the above rate as long as it is elastic (no phonon excitable states). The elastic scattering leads to a phonon mode conversion and thus opens an effective decay channel for transversal phonons. Usually the rate for isotope scattering  $\Gamma_{iso}$  is higher than the decay  $\Gamma_{dec}$ . This means the ratio between longitudinal and transversal phonons in the absorber remains constant according to their density of states. For sapphire and silicon about 10 % are longitudinal and 90 % are transversal phonons. But as only longitudinal phonons can decay the effective decay rate for all phonons is 1/10 of the rate given by equation (2.14).

Simulating the time development of the phonon population using the formulas above shows that the initial phonons rapidly ( $10 \mu\text{s}$ ) decay to a distribution with a mean frequency of about 400–600 GHz. After these first rapid decays all differences in the phonon spectrum caused by ionizing events and nuclear recoils are washed out. Due to the strong frequency dependence of the decay, this phonon generation remains constant for a few ms. During this time they spread ballistically over the crystal.

600 GHz is roughly the maximum of a 10 K Planck distribution. These non-thermal phonons are thermalized via inelastic scattering processes with the crystal surface. On a perfect surface phonons are reflected elastically into one of three possible modes (“acoustic mismatch” model [And81]). In real crystals imperfections and adsorbates cause a diffuse reflection. Most of these reflections are elastic and lead to a uniform phonon distribution in the crystal. Nonetheless inelastic reflections through surface excitations totally thermalize the phonons on a time scale of a few ms.

### 2.2.2 Thermal Coupling

After an energy absorption in the absorber the individual parts of the detector will assume different temperatures. These temperature differences will lead to heat flows until a new thermal equilibrium is established.

The temperature that leads to the signal is the temperature of the electron system in the thermometer film. To understand the time dependence of this signal one has to have a closer look at the couplings of the different parts of the detector. First the coupling of two phonon systems will be discussed and then the coupling of a electron-phonon system.

### Kapitza coupling

When an acoustic phonon hits a boundary between two materials the probabilities for transmission and reflection can be calculated within the theory of anisotropic elastic continua. The energy transmission can be calculated by averaging over all angles and modes [Prö95]:

$$\frac{\dot{Q}_{1 \rightarrow 2}}{A} = \dot{q}_{1 \rightarrow 2} = \frac{1}{2} \frac{E_1}{V_1} \langle \alpha v_{g\perp} \rangle_{1 \rightarrow 2} \quad (2.16)$$

$\dot{Q}_{1 \rightarrow 2}$	...	Energy flow from material 1 to material 2
$A$	...	Contact area
$E_1$	...	Total energy in material 1
$V_1$	...	Volume of material 1
$\alpha$	...	Transmission probability
$v_{g\perp}$	...	Group velocity perpendicular to surface
$\langle \rangle$	...	Average over an angular distribution of all $\vec{k}$ vectors and phonon modes according to the density of states

In a continuum the transmission probability  $\alpha$  is frequency independent and the product  $\alpha v_{g\perp}$  depends only on the direction.

For two phonon systems in thermal contact one can write for the total heat flow over the boundary:

$$\dot{q} = \dot{q}_{1 \rightarrow 2}(T_1) - \dot{q}_{2 \rightarrow 1}(T_2) \quad (2.17)$$

For small  $\Delta T$  and  $\dot{q}_{1 \rightarrow 2}(T_1) - \dot{q}_{2 \rightarrow 1}(T_1) = 0$  the heat flow from material 1 to material 2 becomes:

$$\dot{Q} = A \frac{C_1}{2V_1} \langle \alpha v_{g\perp} \rangle_{1 \rightarrow 2} \Delta T \quad (2.18)$$

$C_1$  ... Heat capacity of the phonon system of ‘material 1’

This is the Kapitza resistance between two materials. Usually it is expressed with a temperature independent parameter  $g_K$ :

$$\dot{Q} = g_K A T^3 \Delta T \text{ with } g_K = \frac{C}{2V T^3} \langle \alpha v_{g\perp} \rangle_{1 \rightarrow 2} \quad (2.19)$$

The  $T^3$  dependence of the Kapitza resistance comes from the  $T^3$  term in the phonon heat capacity.

For a large temperature difference  $\Delta T$  equation (2.17) has to be evaluated for both directions individually. One gets a heat flow of the form:

$$\dot{Q} = A(g_{K1} T_1^4 - g_{K2} T_2^4) \quad (2.20)$$

For the transmission of non-thermal phonons, equation 2.16 can be used to calculate the transmitted power:

$$P = \frac{1}{2} \frac{E}{V} A \langle \alpha v_{g\perp} \rangle \quad (2.21)$$

$E$  is the energy in non-thermal phonons. Because of the surface and isotope scattering one can assume a  $\vec{k}$  distribution according to the density of states for  $\langle \alpha v_{g\perp} \rangle$ .

### Electron-phonon coupling

The electron-phonon interaction is very important for an understanding of the behaviour of the detector. It determines the thermal coupling  $G_e$  of the absorber to the thermometer and it is responsible for the efficient absorption of the high frequency phonons. For small phonon frequencies (thermal phonons) and in the ‘dirty limit’ ( $q \cdot l_e \ll 1$ ,  $q$  phonon wave vector,  $l_e$  electron mean free path) one can show [Liu91, DiT92] that:

$$G_e = \beta T^5 \quad (2.22)$$

$\beta$  is an experimental parameter<sup>5</sup>. The  $T^5$  dependence results in a effective thermal decoupling of the electron system in the thermometer from the phonon system and thus the absorber. For non-thermal phonons the situation is very different. Longitudinal non-thermal phonons are absorbed efficiently in the metal film. Assuming total absorption for longitudinal and no absorption for transversal phonons one can calculate typical average overall absorption efficiencies of 20–30 % [Prö95] in the film. Absorbed phonons thermalize in the thermometer and increase the temperature of the electron system. Together with the decoupling for thermal phonons this can lead to a strong overheating of the thermometer with respect to the absorber. In this case the sensitivity of the detector is governed by the heat capacity of the thermometer and is almost independent of the heat capacity of the absorber.

### Coupling to the heat sink

The detector is thermally coupled to the heat sink via a gold bond wire. The coupling strength defines the time constant  $\tau = C/G$  of the detector. Table 2.2 gives approximate values for the thermal conductance of commonly used gold wires. When using a bonded wire it has to be kept in mind that a good contact between bond wire and detector is required. The film thickness has to be large to avoid that the contact resistance dominates the thermal resistance. For very

---

<sup>5</sup>In principle  $\beta$  can be derived theoretically, but experiments sometimes show strong deviations [Har79].

small thermometers the thermal time constants achievable with the bond wire coupling can get too short. In this case a thin evaporated gold strip can be used to define the coupling between the detector and the heat sink (see figure 3.2).

Wire $\varnothing$ 25 $\mu\text{m}$	$[\Omega/\text{mm}] \pm 10 \%$	$G [\text{nW/K}] \pm 10 \%$
HT 95	61	0.6
AuGa	67.4	0.55
AW 23	1.46	25.2
AW 7	1.9	19.6

Table 2.2: Resistance of bond wires (Trade names from Müller Feindraht) @ 4.2 K. Conductance calculated with Wiedemann-Franz-Law for a 1 cm bond wire at 15 mK.

For gold coupling structures the conductance  $G$  can be designed by choosing the length and width of the strip.  $G$  can be calculated from the resistance at helium temperature with the Wiedemann-Franz-Law:

$$G = \frac{LT}{R}, \quad R = \frac{l}{\sigma A} = \frac{R_{300K}}{RRR} \quad (2.23)$$

- $R$  = Resistance at 4.2 K
- $R_{300K}$  = Resistance at room temperature
- $RRR$  =  $R_{300K}/R$
- $L$  = Lorenz number:  $24.5 \text{ nW}\Omega/\text{K}^2$
- $\sigma$  = Electrical conductivity of Gold film at 4.2 K
- $l, A$  = Length and cross section of Gold film

For typical sputtered gold films with a thickness of  $d = 700 \text{ \AA}$  a  $\sigma$  of  $132(12) \cdot 10^6 \text{ 1}/\Omega\text{m}$  was found at 4.2 K. The RRR (residual resistance ratio), a measure for the electron mean free path, was around 3.8. In films of this thickness the mean free path  $l$  for electrons is not limited by scattering on impurities but by scattering on the surface (for very thin films  $l \sim 1/d$ ). This means that for films with the same quality but a different thickness the RRR will change. The conductance will thus exhibit a stronger than linear dependence on the thickness, e.g. halving the thickness of a very thin strip may lead to a fourfold increase of the resistance.

### 2.2.3 Calorimeter Model

The following section will give a short description of a calorimeter model with a dielectric absorber. Figure 2.5 shows a representative picture of the discussed

model. The model only distinguishes between thermal and non-thermal phonons. The energy transport by thermal phonons is modelled by the thermal couplings, heat capacities and temperatures of the different components of the detector. The non-thermal phonons are described as power inputs directly into the thermometer and the absorber.

The electron and phonon system of the thermometer and the phonon system of the absorber are treated as separate systems. The phonon system of the absorber is thermally coupled to the phonon system of the thermometer via the Kapitza coupling  $G_{ph}$ . The phonon and the electron system of the thermometer are thermally coupled by the electron phonon coupling  $G_e$ . The coupling to the heat bath happens in two places. The (defined) link  $G_{be}$  of the thermometer and the coupling  $G_{ba}$  of the absorber through the mechanical support structure of the detector. Neglecting the heat capacity of the phonon system in the thermometer the couplings  $G_{ph}$  and  $G_e$  can be combined to a single coupling constant:

$$G_{ea} = \left( \frac{1}{G_e} + \frac{1}{G_{ph}} \right)^{-1} \quad (2.24)$$

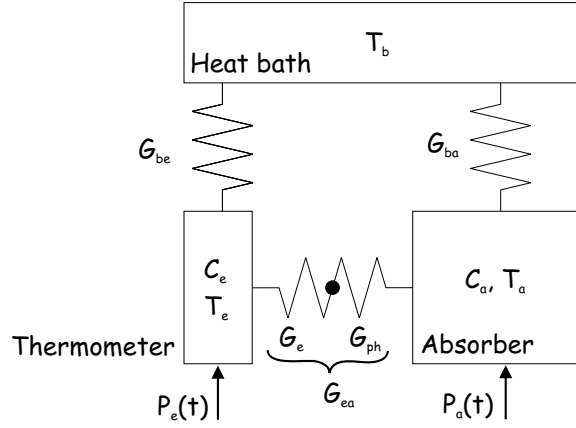


Figure 2.5: Calorimeter model

According to equation 2.21 the non-thermal phonon flux into the thermometer  $P_e$  is described as power input. The part of the non-thermal phonons that thermalizes in the absorber is modelled by a power input  $P_a$  into the absorber.  $P_e$  and  $P_a$  decrease exponentially with time:

$$P_e(t) = P_0 e^{-t/\tau_n}, \quad P_a(t) = \frac{1-\epsilon}{\epsilon} P_e(t), \quad P_0 = \frac{\epsilon \Delta E}{\tau_n} \quad (2.25)$$

$P_0$  ... Initial power input into the thermometer

$\Delta E$  ... Energy deposited in non-thermal phonons in absorber

- $\epsilon$  ... Fraction of energy that thermalizes in thermometer
- $(1 - \epsilon)$  ... Fraction of energy that thermalizes in absorber
- $\tau_n$  ... Effective time constant for thermalization

The effective time constant for the thermalization of non-thermal phonons is a combination of the thermalization in the thermometer and the absorber:

$$\frac{1}{\tau_n} = \lambda_n = \frac{1}{\tau_{film}} + \frac{1}{\tau_{crystal}} \quad (2.26)$$

The time constant  $\tau_{film} \sim V/A$  is proportional to the volume  $V$  of the absorber and indirect proportional to  $A$ .  $\tau_{crystal}$  is a property of the crystal and the crystal surface, and is expected to scale like  $\tau_{crystal} \sim V/O$ , where  $O$  is the surface area of the crystal.

The thermal model of figure 2.5 can be described by two coupled differential equations for the temperature  $T_e$  of the electrons in the thermometer and the temperature  $T_a$  of the phonons in the absorber:

$$C_e \frac{dT_e}{dt} + (T_e - T_a)G_{ea} + (T_e - T_b)G_{be} = P_e(t) \quad (2.27)$$

$$C_a \frac{dT_a}{dt} + (T_a - T_e)G_{ea} + (T_a - T_b)G_{ba} = P_a(t) \quad (2.28)$$

With the initial condition  $T_a(t = 0) = T_e(t = 0) = T_b$  the equations have the following solution for the thermometer signal  $\Delta T(t)$  [Prö95]:

$$\Delta T_e(t) = \Theta(t)[A_n(-e^{-t/\tau_{in}} + e^{-t/\tau_n}) + A_t(e^{-t/\tau_t} - e^{-t/\tau_n})] \quad (2.29)$$

The time between interaction in the absorber and the establishment of a homogeneous distribution of non-thermal phonons was neglected. This is expressed by the step function  $\Theta(t)$ .

The time constants are:

$$\begin{aligned} \tau_{in} &= \frac{1}{\lambda_{in}} = \frac{2}{a + \sqrt{a^2 - 4b}} & \tau_t &= \frac{1}{\lambda_t} = \frac{2}{a - \sqrt{a^2 - 4b}} \\ a &= \frac{G_{ea} + G_{be}}{C_e} + \frac{G_{ea} + G_{ba}}{C_a} & b &= \frac{G_{ea}G_{be} + G_{ea}G_{ba} + G_{be}G_{ba}}{C_e C_a} \end{aligned} \quad (2.30)$$

and the amplitudes:

$$A_n = \frac{P_0(\lambda_{in} - (G_{ba}/C_a))}{\epsilon(\lambda_t - \lambda_{in})(\lambda_{in} - \lambda_n)} \left( \frac{\lambda_t - G_{ba}/C_a}{G_{be} - (C_e/C_a)G_{ba}} - \frac{\epsilon}{C_e} \right) \quad (2.31)$$

$$A_t = \frac{P_0(\lambda_t - (G_{ba}/C_a))}{\epsilon(\lambda_t - \lambda_{in})(\lambda_t - \lambda_n)} \left( \frac{\lambda_{in} - G_{ba}/C_a}{G_{be} - (C_e/C_a)G_{ba}} - \frac{\epsilon}{C_e} \right) \quad (2.32)$$



In equation 2.29  $\tau_{in}$  is the intrinsic time constant of the thermometer and  $\tau_t$  is the thermal relaxation time of the combined system.  $\tau_n$  is the time constant of the non-thermal phonons in the absorber and shows up as the rise time of both signal parts.  $A_n, \tau_{in}$  describe the non-thermal component of the signal. It originates from the direct absorption of non-thermal phonons in the thermometer.  $A_t, \tau_t$  represent the thermal component of the signal, in other words the measured temperature rise of the absorber. Figure 2.6 shows an averaged 6 keV pulse where one can clearly distinguish the two decay times. For a closer discussion of the model and

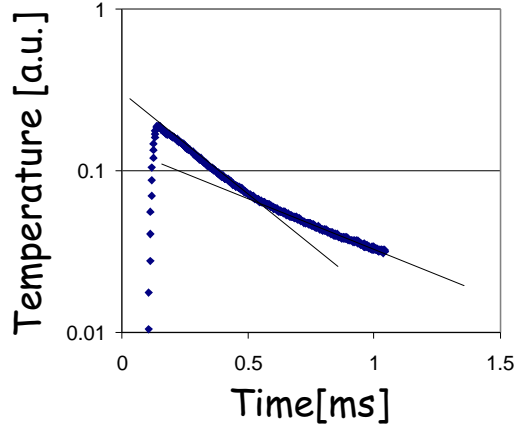


Figure 2.6: Averaged logarithmic plot of a 6 keV pulse with the two decay times indicated.

the solutions see [Prö95].

## 2.3 Phonon Collectors

The high sensitivity of the detectors comes, as already mentioned before, from the fact that the non-thermal phonons mainly heat the small thermometer. This means that the thermometer overheats with respect to the absorber. In the model this is represented by the non-thermal component  $A_n$ . The amplitude  $A_n$  is determined by the heat capacity  $C_e$  of the thermometer and the absorbed energy  $\int P_e dt$ . For small film sizes the thermalization time (2.26) is independent of the area of the thermometer and the absorbed energy per area is constant. The amplitude  $A_n$  for a given film thickness and energy<sup>6</sup> is then independent of the

<sup>6</sup>The thermometer must have a certain thickness to absorb the non-thermal phonons. No systematic studies of the required thickness have been carried out, but calculations of the mean free path [Pip55] suggest that longitudinal non-thermal phonons are totally absorbed in W-films of 2 kÅ thickness.

thermometer size <sup>7</sup>! This means that once the thermometer is small enough that the thermalization time of the non-thermal phonons is dominated by the crystal, the maximum sensitivity for this simple type of thermometer has been reached.

To further increase the sensitivity, heat capacity and collecting area of the thermometer have to be decoupled. This can be achieved with superconducting phonon collectors. They absorb the incoming non-thermal phonon flux and transmit the energy to the thermometer without adding to the heat capacity. This allows to combine a large collecting area with a small heat capacity.

Figure 2.7 illustrates the working principle of the collectors. A high frequency phonon from the absorber breaks a Cooper pair in the aluminium phonon collector and produces excited quasi-particles. The quasi-particles quickly relax to the band gap through the emission of phonons. When their energy is above  $2\Delta$  they can break other Cooper pairs. Phonons below  $2\Delta$  are re-emitted into the absorber. Part of the initially transmitted energy  $E$  is therefore lost. Theoretical [Kur82] and experimental [Joc94] results indicate that about  $E/1.6$  is present in quasi-particles after the relaxation. These results were found with tin, but the mechanisms for aluminium are the same. A typical mean free path of the

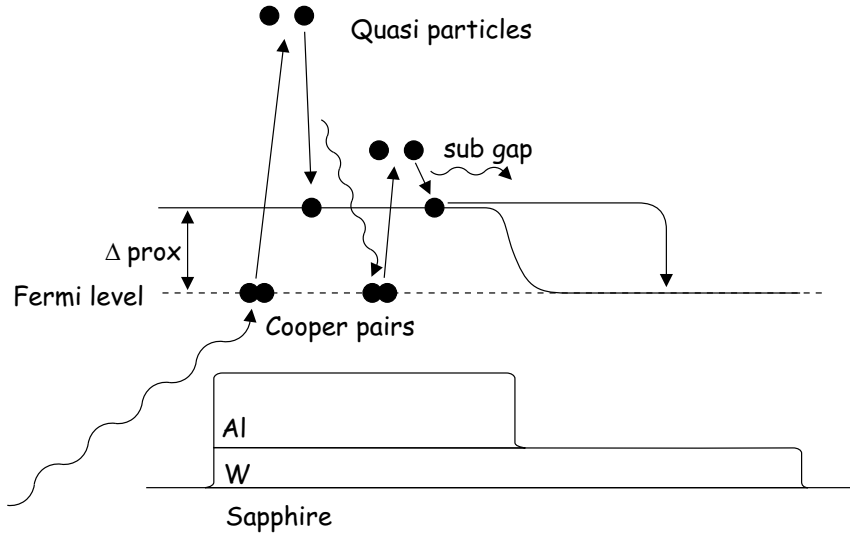


Figure 2.7: Working principle of phonon collectors

high frequency phonons (longitudinal and transversal) in aluminium is a few kÅ [Eis76, Kap76, Loi99]. Phonon collectors with a thickness of 10 kÅ should absorb close to 100 % of all transmitted phonons. This is a factor 3–5 better than for a W-film.

<sup>7</sup>Large thermometers shorten the thermalization time. The absorbed energy per area, and thus the signal, decreases.

After the relaxation the quasi-particles diffuse to the W-film. Here the band gap is zero and they transfer their energy to the electron system of the thermometer. For small losses during this diffusion process a very clean aluminium film is essential. Areas with a reduced energy gap trap the quasi particles and shorten their effective life time. These quasi-particles recombine to Cooper pairs and their energy is lost for the collection.

In a previous work [Loi99] measurements of the diffusion constant  $D$  and the effective life time  $\tau_{quasi}$  of the quasi particles have been carried out. A value of  $D = 2.46 \cdot 10^{-4} \text{ m}^2/\text{s}$  and a life time of  $\tau_{quasi} = 9.0 \text{ ms}$  was found for a W-Al bilayer (the corresponding errors were smaller than the given accuracy). For the average distance the quasi-particles diffuse during their life time one gets  $l = \sqrt{D\tau_{quasi}} \approx 1.5 \text{ mm}$ . Phonon collectors with dimensions below 1 mm are possible without suffering from big quasi-particle losses.

## 2.4 Scintillation & Event Discrimination

The energy deposited in the absorber by an interaction is mostly transferred to the phonon system. But part of it may also escape as photons, or scintillation light. This conversion happens in the luminescent centres of the crystal. These centres may be intrinsic to the crystal lattice (intrinsic scintillators) or ions deliberately doped into the crystal (doped scintillators) [Krö48]. The exact mechanisms that transfer the energy to the luminescent centres (activators) are not finally clarified. The electrons or recoil nuclei excite electron-hole pairs that are captured by the luminescent centres. The following transition can either be radiative or non-radiative. Typically these processes happen on a time scale of 1 ns–50 ns. In a simple picture with a two level system [Krö48] the activator is excited from the equilibrium point A of the ground level to the excited level at point B. From there it relaxes to the new equilibrium C. Now it can decay back to the ground level via a radiative transition (D) or a non-radiative transition at point E if the excited state is given enough thermal energy  $E_Q$ . This leads to the following equations [Kli57] for the scintillation efficiency  $\eta$  and decay time  $\tau$ :

$$\eta = \left(1 + c \cdot \tau_L \cdot \exp\left(\frac{-E_Q}{kT}\right)\right)^{-1} \quad (2.33)$$

$$\tau = c \cdot \exp\left(\frac{-E_Q}{kT}\right) \quad (2.34)$$

- $c$  ... Constant:  $1.6(8) * 10^{10} \text{ sec}^{-1}$
- $\tau_L$  ... Time constant of luminescent transition:  $6.7(7) * 10^{-6} \text{ sec}$
- $E_Q$  ... Energy difference between C & E: 0.34 eV

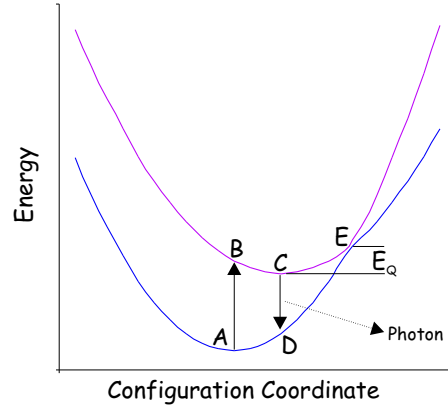


Figure 2.8: Simple two level scheme for activator centre.

Values for  $\text{CaWO}_4$  from [Bea62]

The non-radiative transition leads to a suppression of the scintillation efficiency and shortening of the scintillation time at room temperature. This suppression can be very large at room temperatures. Efficiency increases as much as 4 orders of magnitude have been reported [Ber85].

In the case of doped scintillators the dopant is usually optimized for maximum light output at the chosen operating temperature, e.g. room temperature or liquid nitrogen. Therefore it typically decreases towards low temperatures for commercially available doped crystals. For low temperature detectors where the scintillator is cooled to mK temperatures only intrinsic scintillators are suitable.

The efficiency of the scintillation process is not only dependent on the temperature, but on the density of the deposited energy in the crystal and thus on the initial interaction [Faz98]. For nuclear recoils it is lower than for fully ionizing events. The difference is usually expressed by a quenching factor:

$$QF = \frac{S_{e,\gamma}(E)}{S_{n,W}(E)} \quad (2.35)$$

$S_{e,\gamma}(E)$  and  $S_{n,W}(E)$  are the energy emitted in light (light yield) at a given energy  $E$  for fully ionizing events and nuclear recoils, respectively. The light yield for  $\alpha$ -particles is usually between the two and can show some energy dependence [Dix60, Bea62]. The quenching factor  $QF$  is a property of the crystal type but can even vary slightly from crystal to crystal [Bar00].

The different light yield for the various interactions can be used to separate the event types in the absorber. A simultaneous measurement of the energy that went into the phonon system and the scintillation light identifies the interaction. In a

plot of  $QF$  versus  $E$  the events will group in three bands: recoils, fully ionizing events and alpha particles.

Of course the different interactions in the absorber not only result in different light yields, but the time structure of the emitted scintillation light is also different. This effect is commonly used to discriminate events in scintillators. At room temperatures the time scales of the differences in the light emission for  $\text{CaWO}_4$  are in the order of  $\mu\text{s}$  [Bea62]. This would be too fast to be detected with our type of low temperature detectors. But equation 2.34 predicts a slower scintillation at low temperatures. At mK temperatures the scintillation process in  $\text{CaWO}_4$  seems to be much slower. This may bring the time scales into a range that is still observable with the detectors (see chapter 5).

As mentioned before the mechanisms that transfer the energy to the activators can be quite complex and are not fully understood. The speed of the recoiling nucleus in the case of a nuclear recoil may have an influence on the efficiency of the process. In this case the nuclear recoil band can be split into sub bands if the absorber is composed of different nuclei. This effect is currently under investigation in an neutron scattering experiment [Jag].

# Chapter 3

## Scintillating Detector Module

As already mentioned in chapter 1, the goal for a 300 g  $\text{CaWO}_4$  module is a discrimination threshold of 15 keV at 99.7 % rejection [pro01]. A  $\text{CaWO}_4$  module basically consists of three parts. Two separate detectors, each with its own thermometer and a holder/light collector. The phonon detector measures the heat signal of an event in the  $\text{CaWO}_4$  absorber. The light detector in close proximity but thermally isolated from the  $\text{CaWO}_4$  detects the emitted scintillation light. The holder houses both detectors. It optically isolates one module from the other and serves as a light collector to get as much scintillation light as possible into the light detector. To achieve the desired rejection each part has to fulfil specific requirements. These requirements will be discussed in the following chapter. At the end the design of a prototype module for the setup at Gran Sasso will be introduced.

### 3.1 Light Detector

The discrimination threshold of a module mostly depends on the performance of the light detector. The minimum energy at which scintillation light of a gamma can be detected and distinguished from a nuclear recoil determines this threshold. This means the total energy collected has to be maximized and the threshold of the light detector has to be as low as possible. The fraction of the emitted light energy that is absorbed by the light detector can be influenced by the size and the material of the substrate, whereas the threshold is mainly determined by the thermometer film.

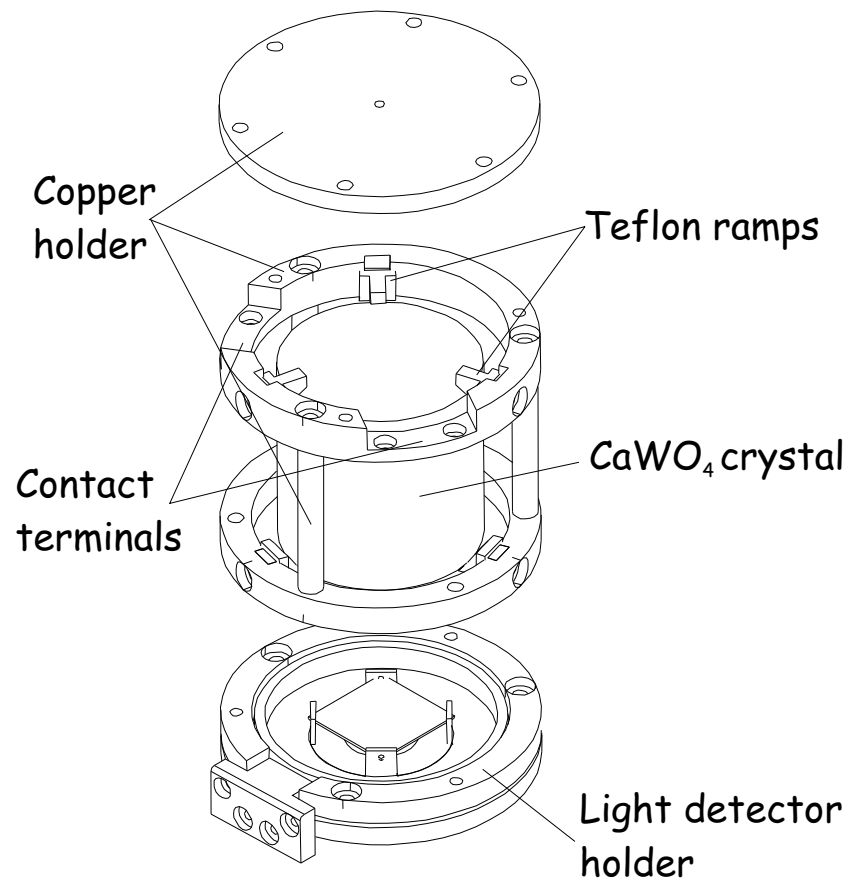


Figure 3.1: Exploded view of the CaWO<sub>4</sub> module with main parts indicated. The light collector around the crystal is not shown.

### 3.1.1 Substrates

To detect the scintillation light the photons have to be absorbed in the substrate and the generated phonons then have to reach the detector film. The number of photons impinging the substrate is proportional to its surface. Whether a photon is absorbed is given by the absorbability of the surface. The size of the substrates can not be increased indefinitely. Practical reasons from the holder design limit the size to about  $20\text{ cm}^2$ . Secondly phonon losses in the thin substrates become significant at a certain size. A detailed discussion of these factors can be found in chapter 5.

The obvious choice as substrate is sapphire. All previous detectors for CRESST were developed on it. The growth of superconducting W-films and subsequent processing steps are well established and substrates of all sizes are readily available. A special coating (absorption layer) has to be evaporated to make the substrates opaque for the scintillation light. Another possibility is silicon. The silicon substrates can be used plain or with a special surface treatment to reduce the reflectivity [Kin91]. An extensive study to evaluate the feasibility of these substrates has been carried out [DiS02].

Measurements to determine the phonon losses in the thin substrates were performed (section 5.2).

### 3.1.2 Film Geometry

The threshold of a detector is given by the point where a signal can be distinguished from the noise. Increasing the sensitivity, i.e. making the signal in the detector larger for a given energy deposition will move this point to lower energies. This is true if the noise remains constant. For Johnson noise and SQUID noise this is usually the case. Noise coming from the detector itself (phonon noise) will generally increase with the sensitivity of the detector. In our case the constant noise sources should dominate the total noise. Therefore one can expect a lower threshold by an increase of the responsivity.

The easiest way to increase the sensitivity of a detector is to decrease its heat capacity  $C$ . A given energy will then lead to a higher temperature rise  $\delta T = \delta E / C$  and thus to a higher signal. The important heat capacity in the CRESST type detectors is the thermometer film itself. This heat capacity can be reduced by decreasing size and thickness of the films. But below certain dimensions three main problems occur.

- Too thin films can not efficiently absorb the non-thermal phonons coming from the substrate (section 2.2).



- The gold bond wires needed for the heater and the thermal ground of the detector will dominate the heat capacity of very small films.
- The thermal coupling strength  $G$  is determined by the bond wire and can not be made sufficiently small. A smaller heat capacity will therefore lead to a shorter intrinsic time constant  $\tau_{in} = G/C$  of the thermometer. When the time constant gets shorter than the time constant of the incoming energy the detector will not be able to integrate the energy any more but only measure the flux, which typically results in a reduced sensitivity.

To overcome these problems a new film geometry was developed (figure 3.2). Its

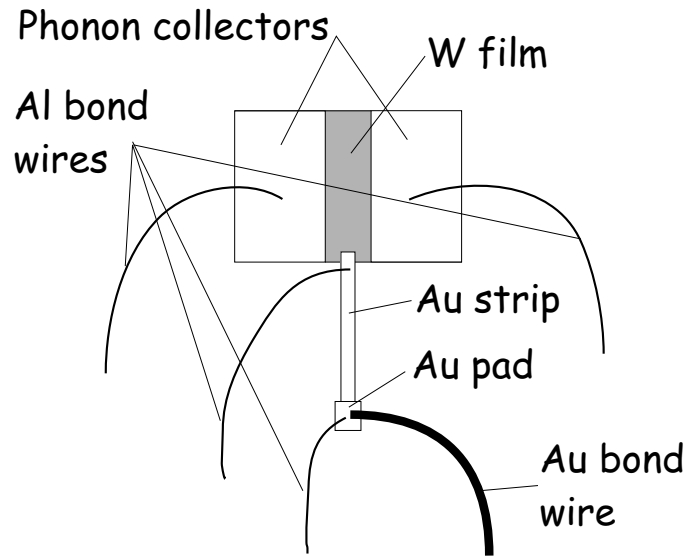


Figure 3.2: Layout of new light detector

key features are:

**Phonon collectors:** The aluminium bond pads were enlarged. They act as heat capacity free phonon collectors.

**Film heaters:** The bond wire heaters were replaced by Au film structures on the substrate with a much smaller heat capacity.

**Film structure coupling:** The gold coupling wire is not bonded directly to the detector but to a gold pad that is connected to the detector via a thin gold strip. This gold strip now defines the coupling strength  $G$ .

The Al pad and the underlying W-film form a proximity bilayer. This bilayer has a transition temperature close to 1.2 K. Therefore the electronic heat capacity at

mK temperatures is negligible. The bond pads collect phonons from the absorber without adding to the total heat capacity of the thermometer.

With this design the phonon collecting area of the thermometer can be kept constant, while at the same time the heat capacity can be greatly reduced. The thickness of the phonon collectors can be optimized to absorb the non-thermal phonons without affecting the heat capacity. The coupling to the heat bath is defined by an evaporated gold film besides the thermometer. The coupling strength can now be chosen to fit the requirements of the detector. At the same time this gold strip serves as a heater. A detailed description of this design can be found in section 5.2.

## 3.2 Phonon Detector

The signal of the phonon detector (heat signal) basically measures the total energy deposited in the absorber, independent of the type of interaction. The ratio of heat signal to light signal then allows to distinguish different types of events. At low energies nuclear recoils may not produce a measurable light signal ('no light' events<sup>1</sup>). In this case the only information to separate real events from spurious (noise) events is the shape of the pulse in the phonon detector. The signal rise time for example is given by the life time of the non-thermal phonons and is expected to be different for fake events from vibrations etc. To reliably extract this shape information the pulses must be well above the noise level of the baseline. This means a threshold that is below the 10 keV of the module is desirable for the phonon detector. As absorber various scintillating crystals ( $\text{CaWO}_4$ ,  $\text{PbWO}_4$ ,  $\text{BaF}_2$ ), BGO) had been tested [Meu99]. Main criteria were the light output (light yield) at mK temperatures and the radiopurity of the crystals. To be sensitive to low WIMP cross sections a large atomic number of the target nuclei is desirable<sup>2</sup>.  $\text{CaWO}_4$  which gave a good light yield compared to the other candidates and has tungsten as a heavy constituent was chosen for the first generation of detectors. Other scintillators work as well and may be used in later stages in case of a positive signal.

A first test detector with the usual CRESST I type thermometer film of  $8 \times 9 \text{ mm}^2$  on a 300 g  $\text{CaWO}_4$  showed a threshold of 10 keV<sup>3</sup> (section 5.3.2). The relatively high threshold can be explained by the high transition temperature

---

<sup>1</sup>The detected light signal may be below the threshold of the light detector. But even with a "perfect" light detector that is sensitive to single photons 'no light' events occur. Very low energetic recoils produce so few photons that with a non zero probability none end up in the light detector (see section 6.1).

<sup>2</sup>For coherent WIMP interactions the cross section is proportional to  $A^2$  ( $A$  = number of nucleons).

<sup>3</sup>The 262 g sapphire detectors had thresholds as low as 580 eV [Coz02a, Alt01].

of the film. Tungsten films directly evaporated onto the surface of  $\text{CaWO}_4$  have their normal- to superconducting transition at 40–50 mK rather than 15 mK for films on sapphire. This phenomenon is still being investigated [Ang01, Fra02]. A diffusion barrier of  $\text{SiO}_2$  evaporated onto the surface prior to tungsten has been found to lower the transition temperature to 15 mK. An improvement of the threshold is expected from this development. Figure 3.3 shows a schematic view of the current design.

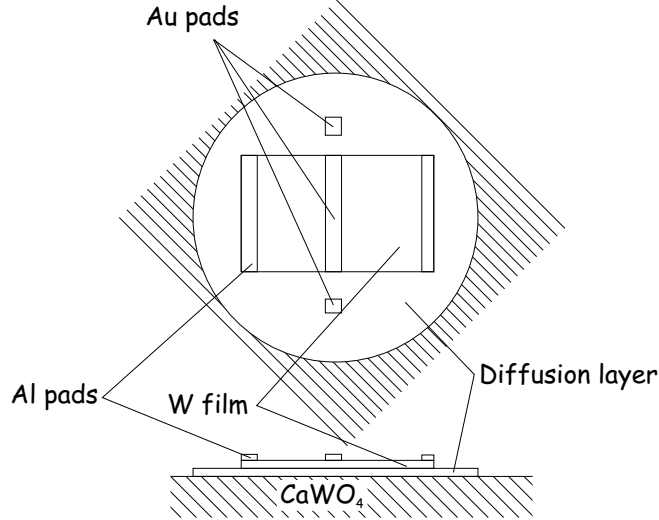


Figure 3.3: Schematic view of the W detectors on  $\text{CaWO}_4$ . The hatched area symbolizes the  $\text{CaWO}_4$  surface. Between the W-film and the crystal a diffusion barrier is evaporated. The detector and all bond pads are structured on this diffusion barrier.

Another problem of  $\text{CaWO}_4$  compared with sapphire is the low speed of sound for the phonons. Taking the Debye temperatures as an estimate for the mean phonon velocity, it is more than a factor of 4.2 slower than in sapphire. This leads to a lower energy flux into the thermometer and can limit the achievable threshold. To compensate that, a new thermometer design with phonon collectors is currently being tested [Sta].

### 3.3 Holder

The crucial point when scaling up the detectors from a 6 g proof-of-principle [Meu99] to a 300 g module is the light collection. The scintillation light is only about 2% (for  $\gamma$ s and  $\beta$ s) of the total energy deposited in  $\text{CaWO}_4$ . In order to be

able to detect light from low energetic interactions ( $10\text{ keV deposited} \rightarrow 200\text{ eV light} \rightarrow 60\text{ photons}$ ) in the absorber one has to efficiently collect the photons.

### 3.3.1 Requirements

The detector holder for the CRESST setup has to fulfil several conditions:

- use exclusively radiopure materials
- provide high reflectivity of inner surface
- hold crystals tightly to minimize the effect of vibrations
- minimize space needed in cryostat

#### Materials

The detector holders are the innermost layer of the CRESST setup. Most of the holder materials directly face the absorber crystals. Therefore very high standards for the radiopurity have to be met. Secondly the materials must allow a stable operation of the detectors at mK temperatures. Because of these reasons the holders in the first phase of CRESST mainly consisted of NOSV copper<sup>4</sup> and small amounts of Teflon [Sis99]. In the new holders copper again serves as the material for the support structure. To avoid soldering, the terminals for the electrical connections of heater and bias current are designed as screw contacts. The superconducting wires from the cryostat are screwed down onto copper pads. From these pads bond wires lead into the inner part of the holder and contact the detectors (figure 3.8). The copper pads are glued to the holder with Araldit. This composite glue is being used by other groups as well and was found to be clean on the required level [Buc00].

Teflon would make a low loss and radiopure reflector. But the large amount needed to achieve a reflectivity of  $> 98\%$  led to problems during cooling and operating the detectors. This makes the use of Teflon reflectors difficult for a large setup with 33 modules. A special sintered Teflon which would allow a thinner reflector did not fulfil the radiopurity requirements. Therefore a special polymeric multilayer foil [Web00] is being used (see next paragraph). The results from measurements of the radioactive background in the foil are compiled in the table 3.1. Taking

---

<sup>4</sup>A special “heat leak” free copper. Normal copper parts have to be annealed after machining to avoid long time constants during cooldown to mK temperatures. This annealing step can diffuse any contaminations present on the surface into the bulk and spoil the radiopurity of the copper. Additionally radioactive elements from the heater filaments can diffuse through the SiO<sub>2</sub> tube and contaminate the copper.

Decay chain/Isotope	Level/Limit	
$^{238}\text{U}/^{234}\text{Th}$	$< 104 \text{ mBq/kg}$	$< 84 \cdot 10^{-10} \text{ g/g}$
$^{238}\text{U}/^{234m}\text{Pa}$	$< 266 \text{ mBq/kg}$	$< 216 \cdot 10^{-10} \text{ g/g}$
$^{238}\text{U}/^{226}\text{Ra}$	$< 8 \text{ mBq/kg}$	$< 7 \cdot 10^{-10} \text{ g/g}$
$^{235}\text{U}$	$< 7 \text{ mBq/kg}$	$< 120 \cdot 10^{-10} \text{ g/g}$
$^{232}\text{Th}$	$< 11 \text{ mBq/kg}$	$< 27 \cdot 10^{-10} \text{ g/g}$
$^{40}\text{K}$	$(76 \pm 34) \text{ mBq/kg}$	$(2.5 \pm 1.1) \cdot 10^{-6} \text{ g/g}$
$^{137}\text{Cs}$	$(4 \pm 2) \text{ mBq/kg}$	
$^{60}\text{Co}$	$< 5 \text{ mBq/kg}$	

Table 3.1: Radioactivity limits for 3M foil. 52 g foil measured on a low background germanium detector in  $2.8 \cdot 10^6 \text{ s}$ .

into account the low mass needed per detector these levels meet the requirements. Assuming 1.2 g of foil needed for one detector the levels found for  $^{40}\text{K}$  and  $^{137}\text{Cs}$  result in  $(8.2 \pm 3.8)$  counts/day from these nuclei. For the mounting and handling of the foil the main problems are expected from a electrical charging up of the foil. This will then attract decay products from the surrounding atmosphere. This can be avoided by minimizing exposure to ambient air.

### Reflector

The ratio of light detector surface ( $1 \text{ cm}^2 - 9 \text{ cm}^2$ ) to inner surface of the holder ( $\approx 120 \text{ cm}^2$ ) means an average photon has to be reflected 15 – 100 times before it hits the light detector. This and the small number of photons require a high overall reflectance of the light reflector of well above 95%. To achieve this a special polymeric multilayer foil [Web00] is being used. At room temperatures it has a reflectivity of  $> 98 \%$  for wavelengths from 400 to 1000 nm for all incident angles and polarizations. This reflectivity is superior to commonly used aluminized Mylar foil [Ste02]. The multilayer foil has a small window below 400 nm where it is transparent. To extend the reflection band to shorter wavelength and cover a larger fraction of the emission peak of  $\text{CaWO}_4$  (figure 3.4) a second layer of aluminized Mylar foil is used. The aluminium foil is behind the multilayer foil and reflects any transmitted light. Figure 3.5 shows the measured reflectivity of pure aluminium and a reflector bilayer. For wavelengths above 390 nm it reflects better than 98 %. This bandwidth covers 87 % of the emission peak<sup>5</sup>.

Parts of the holder that extend inside the reflector (for holding the crystals) need to be as reflective as possible. Otherwise they act as parasitic absorbers and degrade the overall performance of the reflector. Teflon proved to be an ideal

<sup>5</sup>A new foil currently under development at 3M will extend the reflection band to 300 nm [Str01]. This foil will cover the entire emission peak of  $\text{CaWO}_4$ .

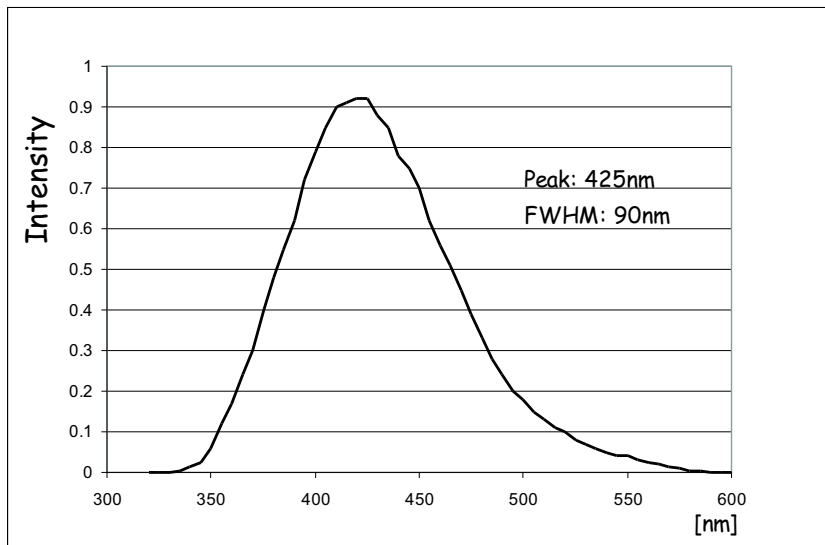


Figure 3.4: Scintillation light peak of  $\text{CaWO}_4$  at 20 K. From room temperature to 4 K a 1.5 fold increase of the emission is observed [Kee01].

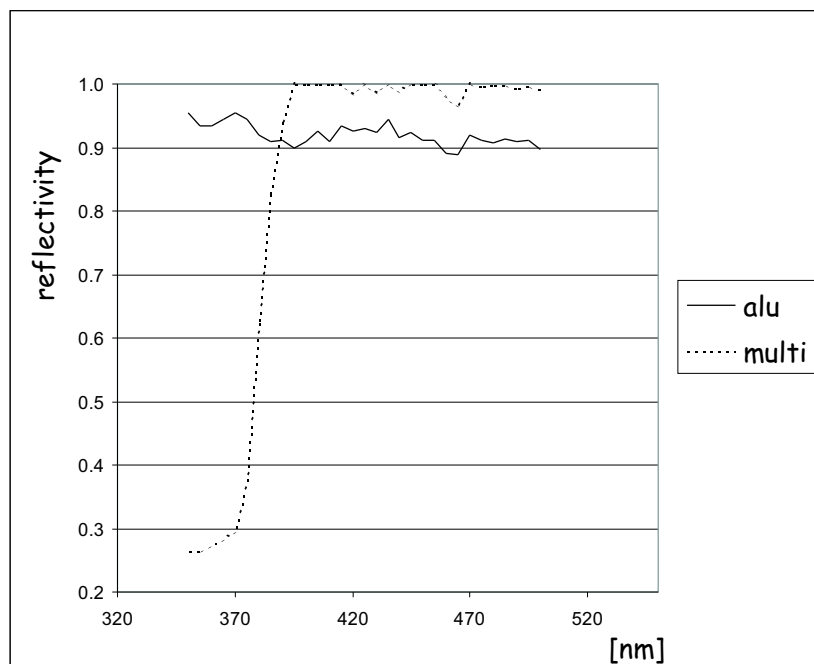


Figure 3.5: Measured reflectivity of a 3M-polymer/aluminium foil bilayer and aluminium foil.

choice because it is very clean and reflective at the same time. The small amount of Teflon needed is uncritical for the detector operation.

### Crystal mounting

The mounting of the crystals at mK temperatures needs some special attention. The contact area between crystal and holder should be small (compared to the size of the thermometer), in order to avoid parasitic thermalization of non-thermal phonons. Nonetheless the crystals have to be fixed tightly. Crystals not held tightly have been found to be very susceptible to vibrations. This can lead to spurious events and/or a warming of the detectors. On the other hand experiences with the sapphire detectors of CRESST I showed that too high pressures result in the formation of tiny cracks under the surface of the crystals. This “cracking” is seen by the thermometers and cannot be distinguished from real particle pulses [Ang02]. To make matters worse  $\text{CaWO}_4$  is a lot more fragile than sapphire.

### $\text{CaWO}_4$

For the reasons given above it is desirable to have some flexibility and thermal shrinkage compensation in the mounting. Ideally the pressure applied to the crystal by the holder at low temperatures should be the same that was adjusted at room temperature. Figure 3.6 shows a schematic view of the  $\text{CaWO}_4$  crystal mounting. The crystal is held by 6 Teflon ramps. To keep the contact area small

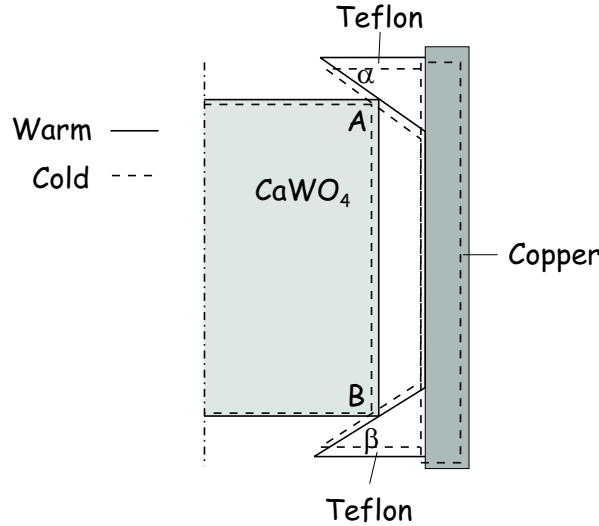


Figure 3.6: Schematic section of the  $\text{CaWO}_4$  mounting in the holder

the Teflon supports only touch the crystal at its edges. The radial and longitudinal contraction compensation is achieved by choosing the correct angles  $\alpha, \beta$ . The

stronger contraction of the copper (0.33 %) in comparison to the  $\text{CaWO}_4$  (0.2 %) is counterbalanced by the contraction of the Teflon (2.7 %<sup>6</sup>). When the holder cools, the contact points A, B “slide” along the Teflon ramps without losing contact or being pressed more strongly. The Teflon ramps can be fixed to the copper holder with screws and spring washers to provide some flexibility.

### Light detector

For the mounting of the light detector in close proximity to the  $\text{CaWO}_4$  crystal one has two different possibilities. Either the light detector is **outside** the reflector and the light is guided/focused onto the detector, or the detector is **inside** the reflector and the light detector directly absorbs the light.

The first alternative would allow a small, conventionally mounted<sup>7</sup> detector. But simulations have shown that it is not possible to focus the emitted photons onto a small detector<sup>8</sup>. Enclosing the crystals in an ellipsoid with the  $\text{CaWO}_4$  and light detector in the two focal points is no option because of the large amount of space needed for such an arrangement to be effective. Secondly a detector mounted outside can only absorb with part (front side) of its surface. A detector mounted inside can be almost fully exposed. In the case of a thin substrate this increases the active surface by a factor of 2. Simulations in a later section (6.1) will look at this argument in detail. For mounting the detector inside the reflector a new holding scheme had to be developed, because Copper would efficiently absorb the (blue) scintillation light photons.

In the prototype module the light detector is held by four thin Teflon sheets. Each corner of the detector rests in a small hole in the Teflon. This ensures a small contact area and a fully exposed surface of the detector. The Teflon applies enough force to hold the detector and still provides some flexibility at low temperatures<sup>9</sup>. Additionally this way of mounting the detector makes it possible to “lift” it from the surface. The backside is exposed and adds to the effective absorbing area (see figure 3.7).

---

<sup>6</sup>Contraction coefficients from [Pob92].

<sup>7</sup>Copper frame and sapphire balls

<sup>8</sup>The phase space for the photons is conserved. An optics that concentrates the photons onto a smaller area only has a limited acceptance angle at its entrance aperture. In the case of photons with directions randomly distributed in  $4\pi$  no effective concentration can be achieved.

<sup>9</sup>The exact force the Teflon applies to the detector at low temperatures is not known. Too big forces may lead to the before mentioned pulses due to “cracking” of the sapphire. For this reason a glued, tension free mounting [Pet02] is being tested.



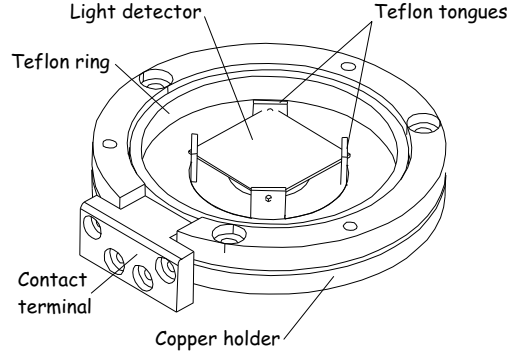


Figure 3.7: Technical drawing of light detector endcap

### Space considerations

For the second phase of CRESST a total target mass of 10 kg is projected. This means 33 modules of 300 g each have to fit into the existing cryostat. Secondly servicing and exchanging individual modules must be possible with all 33 modules mounted. These requirements put some upper limits on the dimensions of the holders: about 8 cm for the height and 7 cm for the diameter. It is planned to arrange the detectors in 11 towers of 3 modules each. Each tower can be mounted and wired independently of the rest.

### 3.3.2 Design

The holder for the absorber crystal ( $\varnothing 40 \text{ mm} \times 40 \text{ mm}$ ) consists of two copper rings and three copper rods (figure 3.1). Inside this structure a layer of highly reflective polymeric foil [Web00] serves as a light reflector (not shown in figure 3.1). Six Teflon ramps, three on each side, hold the crystal in place.

The light detector is mounted in one endcap of the holder. It is held at its corners by four thin Teflon sheets (figure 3.7). The endcap with the light detector can be assembled independently of the rest of the module. The maximum size for the light detectors is about  $3 \times 3 \text{ cm}^2$  for square substrates. The thermometers on the crystals are heat sunk by a gold wire bonded to a gold pad on the detector and to the copper holder. Both endcaps of the holder are covered with reflective foil to fully enclose the setup in the light reflector. The interface between the endcaps and the cylindrical reflector around the crystal is provided by overlapping Teflon rings. Small gaps between these rings and the foil provide access for the electrical connections of the detectors (figure 3.8). The open copper structure was chosen to increase the chance of multiple scattering in different  $\text{CaWO}_4$  crystals for background photons. In a multi detector setup this opens another possibility of background rejection during data analysis. This method was already exploited

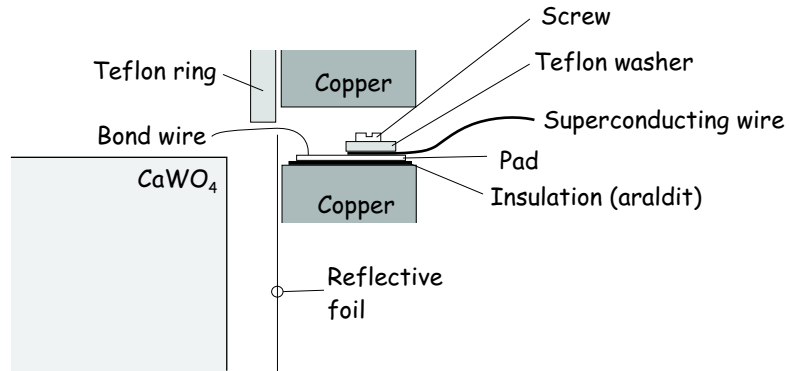


Figure 3.8: Schematic view of contact pad and feedthrough of bond wires.

with the sapphire detectors [Sis99, Coz02a, Alt01].

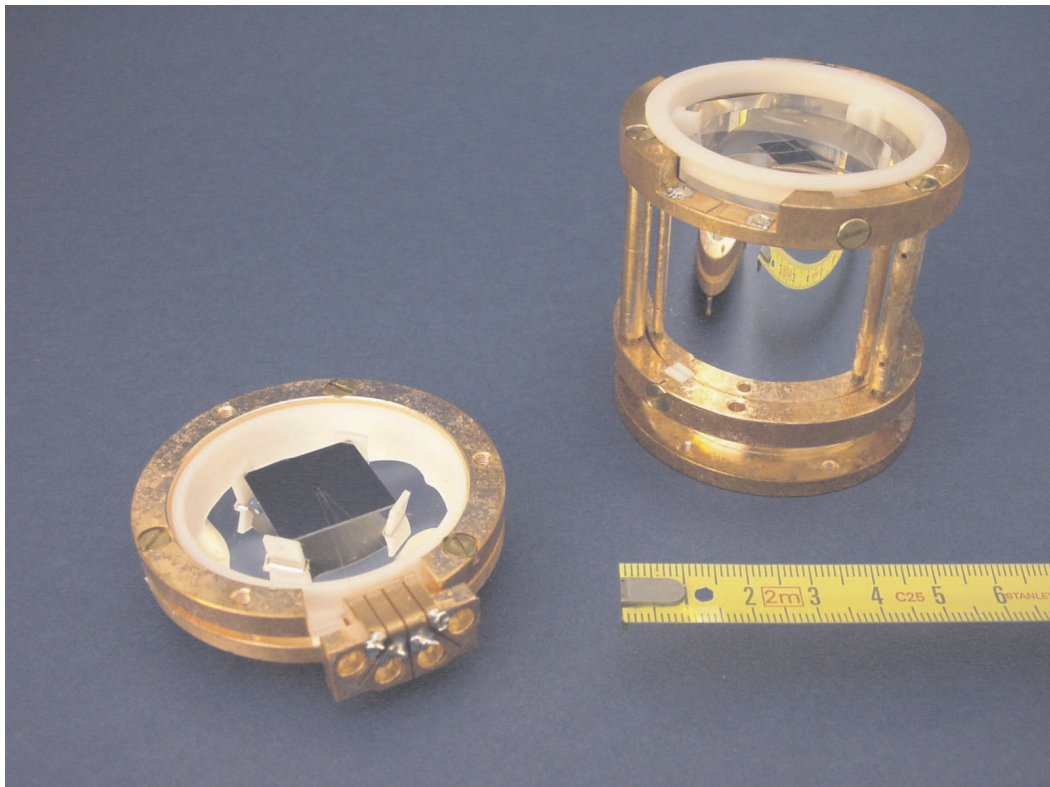


Figure 3.9: Picture of an open detector module.

# Chapter 4

## Fabrication & Experimental Techniques

The low temperature detectors made for this work use several different absorber materials. Besides sapphire which has been well investigated for the CRESST-I detectors already,  $\text{CaWO}_4$  and silicon have been used. As a first step a tungsten film is evaporated onto one surface. This film is structured with photolithographic techniques to the size of the actual thermometer. Further photo mask and sputtering steps follow to pattern aluminium and gold pads for the electric and thermal connections. To meet the required surface cleanliness and radiopurity several cleaning steps before and during the procedure are applied.

### 4.1 Fabrication of Detectors

Prior to the evaporation of the tungsten films the sapphire substrates are cleaned in a special procedure. This is necessary to obtain reproducible transition temperatures of the films. Already small amounts of ferromagnetic contaminations (ppm range) on the surface can lower the transition temperature by 1–10 mK. The following method reduces these contaminations by a factor of 20–30 [Mei99]:

1. 5 min ultrasonic cleaning in ultra pure water
2. 20 min etching in 50 %  $\text{H}_3\text{PO}_4$  (pro analysi) @ 90–110 °C
3. 5 min ultrasonic cleaning in ultra pure water
4. 20 min etching in 1 part 65 %  $\text{HNO}_3$  (pro analysi) + 3 parts 25 %  $\text{HCl}$  (pro analysi) @ 90–110 °C
5. 5 min ultrasonic cleaning in ultra pure water

#### 6. Drying with clean nitrogen gas

This method cannot be used for the  $\text{CaWO}_4$  crystals because they are attacked by concentrated acids. Therefore they were only rinsed with ultra pure water and Acetone. The whole process is done in special Teflon beakers which are only used for this purpose.

### 4.1.1 Evaporation of Films

For evaporation of the tungsten film the crystals are mounted in an ultra high vacuum system. After a 24 h baking cycle a pressure of some  $10^{-11}$  mbar is reached. A titanium sublimation pump and liquid nitrogen shields further reduce this pressure. During the evaporation the substrates are heated with a radiative heater to 450–550 °C. This ensures a good epitactical growth of the W-films on a specially orientated crystal surface (r-plane) of sapphire [Col95a]. As evaporation material tungsten single crystals with a purity of 99.99 % are being used. The single crystals are evaporated with a 4 kW e-gun. Typical evaporation parameters are rates about 2 Å/s, and a final film thickness of 2 kÅ. A detailed description of the evaporation system can be found in [Col92].

Typical transition temperatures for films evaporated in this process are  $\approx 15$  mK. On  $\text{CaWO}_4$  substrates however, W-films have transitions at 30–60 mK. This was attributed to interdiffusion of substrate and film. A layer of  $\text{Al}_2\text{O}_3$  or  $\text{SiO}_2$  evaporated prior to tungsten, suppressed this effect and leads to reproducible transitions at 15 mK [Ang01].

### 4.1.2 Structuring of Detectors

After the evaporation the films have to be structured. This is done with a positive photolithographic process and wet chemical etching with the following steps.

1. Ultrasonic cleaning of film and crystal in Acetone (pro analysi) and ultra pure water
2. Application of positive photo resist (AZ 4562) and spinning for 30 s @ 5000 U/min
3. 30 min bake in oven or 5 min on hot plate (thin substrates) @ 95 °C
4. 1 h cool down (5 min for thin substrates)
5. 1 min structure exposure to UV light
6.  $\approx 2$  min developing in 1 part AZ developer and 1 part water

7. Etching with 30 %  $\text{H}_2\text{O}_2$  or a solution of  $\text{K}_3\text{Fe}(\text{CN})_6$  &  $\text{C}_2\text{H}_8\text{N}_2$  [Col95b]
8. Removal of photo resist in Acetone
9. Ultrasonic cleaning of film and crystal in Acetone (pro analysi) and ultra pure water

The long times for the bake are needed for large substrates only. Here a bake in the oven leads to more reproducible results. Thin slides can be baked on a hot plate. The cooldown time of 1 h is required for the  $\text{CaWO}_4$  crystals. These are prone to crack when temperature gradients occur in the crystal. Therefore setting the crystals on cold surfaces or transferring them into cold liquids has to be avoided. The critical step for the structuring is the etching. It removes all parts of the tungsten film that is not covered by photo resist. Using  $\text{H}_2\text{O}_2$  as etching solution takes up to 10 min for 2 kÅ (depending on the age of the  $\text{H}_2\text{O}_2$  solution). Usually the photo masks do not stick on the substrate for long enough and have to be redone several times. The second solution works a lot faster ( $\sim 1$  min) but contains potassium. This may contaminate the surface of the detectors. For future use we will therefore replace it by the chemically similar sodium which works in the same way [Ang01]. After the etching, the crystals are rinsed thoroughly to stop the process and avoid underetching.

### Contact Pads

The contact pads are structured with a lift off process. Photo resist covers the whole substrate except the places where the pad should be. After the sputtering or evaporation of Al/Au the photo resist can be removed with Acetone. The deposited material on top of the photo resist will be removed in this step as well. The Al/Au only stays in places that were not covered by resist.

The standard process for negative photo masks is as follows.

1. Ultrasonic cleaning of film and crystal in Acetone (pro analysi) and ultra pure water
2. Application of negative photo resist (ma-N 440) and spinning for 30 s @ 2000–4000 U/min
3. 30 min bake in oven or 6 min on hot plate (thin substrates) @ 95 °C
4. 1 h cool down (5 min for thin substrates)
5. 2 min structure exposure to UV light
6. 30–60 s developing in ma-N 333 developer

7. Rinsing with ultra pure water
8. Drying with clean nitrogen gas

Again the long cool down times are only needed for the  $\text{CaWO}_4$  crystals. The developer removes all areas that have not been exposed to UV light. The time needed can vary slightly. As soon as all parts are fully removed the substrate must be taken out of the developer and thoroughly rinsed with water to stop the process. Otherwise the underetching of the edges can get to large.

### Sputtering System

The pads for electrical and thermal connections as well as Au heater strips can be deposited in a sputtering system. If the aluminium pads should act as phonon collectors the quality of these films is not sufficient. The aluminium pads must be evaporated in this case.

The setup used in this work is a Magnetron sputtering system. It has three fixed targets (W,Au,Al) and an ion gun for cleaning the substrates prior to deposition. The samples can be placed on 6 different tables that can be rotated under the targets. The sputter operation itself is controlled by a timer module. The first step of a deposition process is always the cleaning of the surface with the ion gun to remove surface contaminations and improve the adhesion between film and substrate. Then a thin additional adhesion layer (if needed) and the actual pad/heater strip are deposited.

In this system the sputter positions are horizontal tables with the targets on top of them. The samples can be placed without any additional holding structure which allows to coat samples of almost any shape and size. However the height is limited to  $\approx 4$  cm because of the clearance below the shutter. Before placing the sample on the table it is wrapped in aluminium foil that only leaves a window around the actual deposition area. In this way the sides of (high) samples are protected against accidental coating. To ensure reproducible results the samples should be placed on a table designated for the selected sputter material. Secondly only one deposition per run should be made to avoid cross contamination.

### Ion Gun

After pumping the system to  $p < 1 \cdot 10^{-6}$  mbar the planet with the sample is positioned one spot before the ion gun and the shutter in position 1 or 3. All knobs on the ion source panel must be turned fully counter clockwise (off), the mode selector in position **manual** and source and beam **off**. The planet rotation should be **on** to ensure a uniform result. Now the ion gun can be started.

1. Switch on cooling and Ar-gas
2. Open 'Ion gas' and adjust pressure with needle valve to  $p = 2 \cdot 10^{-4}$  **Torr**
3. Switch on **Main** and **Source**
4. Adjust 'Discharge voltage' to 40 V
5. Adjust 'Cathode current' to 6 A (cathode light stops blinking)
6. Switch on **Beam**
7. Adjust 'Accelerator voltage' to 100 V
8. Adjust 'Beam voltage' to 500 V
9. Adjust 'Beam current' (5–10 mA) using the **Cathode knob**
10. Adjust 'Neutralizer emission current' to match beam current

Now all control lamps should be illuminated. The planet with the sample can now be moved in front of the ion gun. After the desired cleaning time (4–10 min) the planet can be rotated away before stopping the ion gun. To switch off the ion gun the steps above should be done in reverse order.

### Sputtering

For sputtering the sample is brought under the required target. The system can perform an automatic pre-sputter (sputter/pre-sputter selector on the timer module in pre-sputter position). In this case the shutter must be in the position before the selected target. After the pre-sputter time has elapsed the system will rotate the shutter one position and thus open the target. If no pre-sputter should be performed the sputter/pre-sputter selector must be set to sputter and the shutter opening must be under the target. It is always recommended to do a pre-sputter to remove a possible oxide layer or other contaminants from the target. This ensures reproducible films.

1. Switch on cooling and Ar-gas
2. Switch off ion gauge
3. Turn on GP 310 and set to 10 mTorr range
4. Press **System gas** & **Throttle**
5. Adjust pressure with needle valve to 7.5 mTorr



6. Switch on ‘Circuit breakers’ on K4A power supply and select required target
7. Select pre-sputter and sputter times on timer module
8. Press **Start** button
9. Turn up ‘Power control knob’ until plasma ignites then adjust desired current

The sputter and pre-sputter times have to be selected on the timer that is in the slot which corresponds to the required target (1: W, 2: Au, 4: Al). At the end of the selected sputter time the power supply switches off automatically. The ‘Power control knob’ can now be turned down, all valves closed and the water cooling switched of.

Because of the multitarget multiposition layout there is no rate monitor in the system. This means the deposition rate can not be measured during the process but had to be calibrated before by measuring the resulting film thickness under varying deposition conditions. The dependence between deposition rate and power is approximately linear for a constant argon pressure. By choosing the power<sup>1</sup> and the time the final thickness can be adjusted. But as the deposition rate can influence the film quality, usually the power is kept constant and the thickness adjusted by varying the deposition time.

### Adhesion Layer

For aluminium the process above is sufficient. For gold films an additional layer is needed between substrate and gold to enhance the adhesion. A thin (50 Å) tungsten layer has proved to be suitable for this purpose. The tungsten and the gold layer are fabricated in one process. To keep the time between the two depositions short (and thus ensure a good contact between the layers) the pre-sputters for both targets were done before the tungsten layer was deposited. In this way only a very brief pre-sputter for the gold deposition is needed in order to start the target and adjust the power.

Tables 4.1 & 4.2 summarize the process parameters for the different types of pads and structures.

### Aluminium evaporation

For phonon collectors the quality of sputtered films is not sufficient. Therefore an aluminium evaporation system was used. The system at the MPI [Loi99] was

---

<sup>1</sup>In fact one adjusts the current and multiplies with the displayed voltage

	process	time	parameters	result
	cleaning	5 min	5 mA/500 V	
Al	pre-sputter	2 min	0.7 A/270 V	2 Å/s
	sputter	40 min		5000 Å

Table 4.1: Parameters for aluminium pads

	process	time	parameters	result
	cleaning	5 min	5 mA/500 V	
Au	pre-sputter	4 min	0.3 A/370 V	3 Å/s
W	pre-sputter	4 min	0.4 A/250 V	1 Å/s
	sputter	50 sec		50 Å
Au	pre-sputter	10 s	0.3 A/370 V	
	sputter	4 min		700 Å
		30 min		5300 Å

Table 4.2: Parameters for Gold heaters/pads

not available for this purpose during the time of this work. The 4-chamber tunnel junction setup in Garching was used instead. It has a low energy Kaufmann ion gun for cleaning the surface of the substrates. For evaporation it features a 2 kW e-gun. During the evaporation the samples can be heated to improve the film quality. The deposition rate can be measured online with a light transmission method. Typically a final thickness of 10 kÅ at a rate of 10 Å/s was deposited. With this evaporation technique aluminum films with a RRR (residual resistance ratio) of up to 100 can be deposited. A more detailed description can be found in [Joc94, Het98].

### 4.1.3 Absorption Layers

The light detectors on sapphire substrates need an extra layer on the backside for the light absorption. This layer was sputtered after the structuring process of the thermometer film. For this purpose a multi target sputtering system at the TUM was used (see figure 4.1).

Before mounting the detector in the vacuum chamber it has to be cleaned thoroughly with Acetone and water. Then a protective layer of positive photo resist is placed over the thermometer film. If the absorption layer is deposited on the opposite side of the substrate (see figure 4.2) the entire substrate surface with the thermometer can be covered<sup>2</sup>. The bake and cooldown of the resist can be a

<sup>2</sup>Special care has to be taken to keep the surface for the absorption layer clean of photo

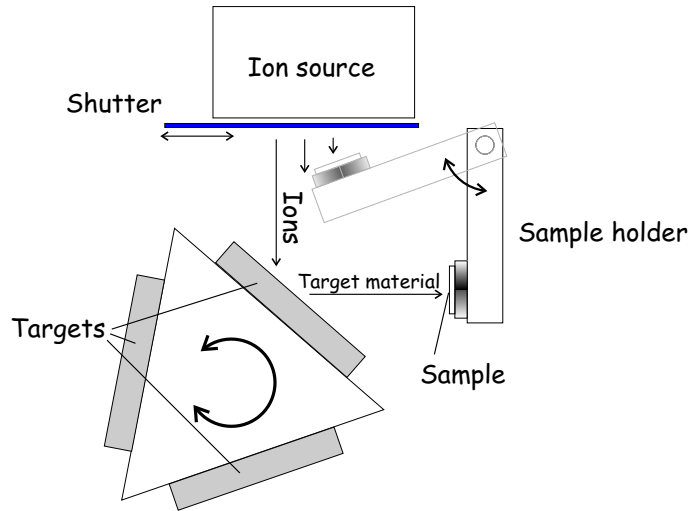


Figure 4.1: Schematic view of sputtering system in Garching (E15)

bit longer than described in section 4.1.2. Otherwise it may happen that small solvent remnants in the resist cause bubbles and long evacuation times. If the absorption layer should be on the same surface as the thermometer a photo resist patch that covers the thermometer only, has to be structured according to section 4.1.2.

After the cleaning and putting the protective resist cover, the substrates are clamped onto the sample holder and mounted in the vacuum system. After the

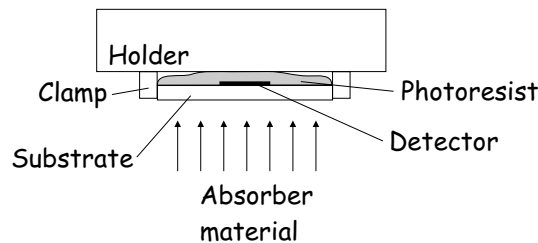


Figure 4.2: Mounting of light detectors for the absorption layer deposition.

detector is mounted on the holder and the chamber closed, the following steps describe the operation of the system:

1. Pump recipient with roughing pump to 50 mbar
2. Open cryo pump and wait until pressure is at  $5 \times 10^{-5}$  mbar
3. Switch on 'Ar' gas

---

resist. It is therefore best not to use the spinner but a pipette to apply a thin layer of resist.

4. Switch on pressure controller  $\rightarrow$  filament on  $\rightarrow$  control close
5. Close shutter
6. Target & high voltage cooling on
7. Isolation transformer on
8. High voltage on, adjust to 250 V
9. Neutralizer & suppressor on, set suppressor to 200 V
10. Increase high voltage to 1100 V
11. Magnet on  $\rightarrow$  adjust current to 60–80 mA
12. Neutralizer on ( $\approx 1$  kV)

The sample holder is positioned below the ion gun and the shutter opened for 5 s to clean the surface. The short time is a compromise between cleaning and damaging the surface. Ion gun cleaning destroys the surface structure of the substrate. This disturbs the phonon propagation in the substrate and thus degenerates the performance of the detector if used on a large surface. No ion gun cleaning on the other hand lead to bad adhesion and unreproducible films.

After this cleaning the holder is moved into the lower position and the shutter opened again to start the sputter process. Generally thicknesses between 4 and 6 kÅ for Si and 5 kÅ for SiO were deposited. To reduce the heating up of the samples during sputtering the process can be interrupted after 2–3 kÅ.

To shut the system down the instructions must be carried out in reverse order. After the sample is taken out, the system must be closed and evacuated again.

### Absorption measurements

To be able to compare the absorption quality of the different substrates and surface treatments a simple “integrating sphere” was built. It basically consists of a hollow Teflon cube with a blue LED and a small photodiode inside. One wall has a  $1.5 \times 1.5$  cm<sup>2</sup> hole for the test samples (figure 4.3). A little circuit board was designed, that integrates the power supply for the LED and the amplifier for the photodiode.

The working principle is quite simple. The LED emits blue light that simulates the emission spectrum of CaWO<sub>4</sub>. A Teflon screen in front of it ensures a homogeneous (diffuse) distribution of the light in the cube. The light intensity in the cube is sensed by a photodiode. A sample in front of the opening will absorb/reflect the light according to its absorption and thus change the intensity

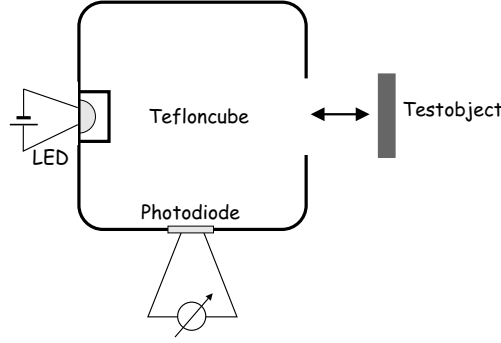


Figure 4.3: Setup for measuring the absorption of light detectors

in the cube. The measured signal from the photodiode is amplified and can be displayed using a common multimeter.

With this method two samples can be compared qualitatively. To get absolute numbers for the absorption a calibration with known samples has to be performed, e.g. Teflon pieces with various sizes of black spots. Using this method the following formula describes the relation between absorption and output signal:

$$X = \alpha \cdot \left( \ln \left( \frac{V - P_1}{P_2} \right) \right) \quad (4.1)$$

$X$  ... Absorption of sample (0–1)

$V$  ... Measured signal [V]

$\alpha$  = –0.61 (Fit)

$$P_1 = V_1 - P_2 \exp\left(\frac{X_1}{\alpha}\right)$$

$$P_2 = \frac{V_2 - V_1}{\exp\left(\frac{X_2}{\alpha}\right) - \exp\left(\frac{X_1}{\alpha}\right)}$$

$V_{1/2}, X_{1/2}$  ... Measurements of known samples

To fix the parameters  $V_{1/2}, X_{1/2}$  two measurements of known samples have to be made at the beginning. For example multilayer foil (1 % absorption) and “open” hole with a black cover over it (100 % absorption). Table 4.1.3 compiles the results of some measured materials.

## 4.2 Setup in Cryostat

For the measurement of the detectors three dilution refrigerators with base temperatures of 10–15 mK were available. They were each equipped with 2–3 SQUID

Sample	Absorption ( $\pm 2\%$ )
Multilayer foil	1 %
polished Silicon	60 %
etched Silicon[DiS02]	70 %
Silicon monoxide	67 %
Silicon on Sapphire (front)	56 %
Silicon on Sapphire (back)	80 %

Table 4.3: Results of absorption measurements

systems for the detector readout and 2 resistance bridges for the thermometry. A CAMAC crate connected to the ether net was used for the data acquisition. Various programs were available for data handling and analysis. The measurements presented in this work were mainly done in a self made cryostat ('cryostat I'). The setup will be described in detail in the following paragraphs.

### 4.2.1 Cryostat & Data Acquisition System

Figure 4.4 shows the principal setup of the different components. The vertical divisions indicate the temperature levels and positions of the parts.

#### Cryostat

The used cryostat is a self made dilution refrigerator that reaches a base temperature of 10 mK. It is situated in a Faraday cage to isolate it from electromagnetic interferences. The electronics for the operation of the cryostat and the experiments (current sources, resistance bridges, SQUID electronics, pulse generator) are inside the cage. The signals are passed outside to the CAMAC crate via low pass feedthrough filters in the Faraday cage wall. The control panels, pumps, cold traps etc needed for the operation of the refrigerator are outside the Faraday cage in the annexes. The cryostat itself rests on air dampers to isolate it from vibrations of the building.

#### Experiment setup

The experiments are set up at the lowest point of the cryostat where it reaches its base temperature, the so called mixing chamber (see figure 4.4). It acts as the heat sink for the setup. Usually the mechanical connection is done in a thermally isolated way (Nylon screws). A thermal link (copper wire) provides a well defined thermal coupling to the heat sink. The mixing chamber reaches a base

temperature of 10 mK in continuous operation. To stabilize it at a desired higher temperature it has a temperature sensor and a resistive heater. The temperature sensor is a carbon thermistor that is read out by a four point AC resistance bridge. The resistance signal is passed to a PID controller which compares it with the set point and generates the current for the heater. The lines for the thermometer and the heater have low pass filters at 4 K to reduce the influence of pickup noise. A stability of  $\pm 10 \Omega$  or  $\pm 7 \mu\text{K}$  can be reached hereby. The shunt box that contains the biasing circuit for the detector readout (section 2.1) is directly connected to the mixing chamber to benefit from the lower Johnson noise of the bias resistor at base temperature.

The detector holder is weakly coupled to this heat sink. In this way a further reduction of residual temperature fluctuations of the mixing chamber can be achieved. The holder is the temperature reference for the detector. A gold bonding wire or a thin gold film strip defines the coupling of the detector to this reference. Every detector has a film heater attached to the thermometer for an independent temperature stabilization of the detector and the injection heater pulses for the calibration. For a one detector setup this heater is not strictly necessary as the mixing chamber can be stabilized at the operating point of the detector. If two (scintillating module) or more detectors have to be run simultaneously the operating points will in general not be at the same temperature. The mixing chamber has then to be set below the lowest operating point and the detectors are stabilized with their individual heaters.

The electrical connections of the detectors are done with twisted pairs of superconducting wires. The wires for the readout have an additional Cu-Ni shielding.

### Readout scheme

The bias current for the detector readout is provided by a floating current source at room temperature. It consists of two ground referenced current sources providing identical currents with opposite sign. The current is adjusted with a potentiometer or a externally provided voltage. At 20 mK an H-type low pass filter (cutoff: 10 kHz) is inserted in the lines to reduce high frequency noise before it enters the shunt box. From the filter downwards the superconducting twisted pair runs in a superconducting shield to prevent pickup noise. In the shunt box the shunt resistor can be selected (5–50 m $\Omega$ ). From the box two shielded twisted pairs go to the detector and the SQUID (Applied physics SQUID system). The SQUID sensors are located in the liquid helium bath at 4.2 K. The processed signal goes to a  $\times 1$  differential amplifier (to avoid ground loops and to match the impedance of the Faraday cage feedthrough filters) before it leaves the Faraday cage.

The film heater of the detector is used to stabilize the detector and/or send test pulses for calibration. It is connected to a feedback unit. This feedback unit is

basically a summing amplifier followed by an analog square-rooter at the output to linearize the dependence of input and heating power<sup>3</sup>. The heating power and thus the long-time baseline stability is regulated by a computer controlled DAC (Digital Analog Converter) connected to the summing amplifier. The DAC output is provided by a computer programmed PID controller (see CONTROL program). The signal is filtered with a 10 s low pass filter to remove any influence from the switching in the DAC. For short time baseline stability ( $< 10$  s) the SQUID signal can directly be fed back to the feedback unit via an attenuator AC-coupled to the summing amplifier (shown with dashed lines in figure 4.4). The AC coupling is necessary to be independent of the flux quantum state of the SQUID. As a second effect this feedback shortens the pulse length which helps to avoid pile up, to improve the long term control of the baseline in the case of a high pulse rate. A pulse generator is connected to the summing amplifier to be able to inject test pulses into the detector. They provide the means to calibrate and linearize the detector.

In the case of two detectors the setup for the second channel is identical to the one described above.

## Data acquisition

The data acquisition system is located outside the Faraday cage. The signals from the resistance bridges and the DC level of the feedback are read out by a digital voltmeter (DVM). The SQUID signals are filtered with a programmable low pass filter amplifier (cutoff 100 Hz–50 kHz). The cutoff is set below half of the sampling frequency of the transient recorder (typically 2–10  $\mu$ s) to avoid anti aliasing problems. The signal after the filter is passed to a transient recorder and the trigger generator. Between the filter amplifier and the trigger generator a  $\times 10$  or  $\times 100$  amplifier is inserted. A second filter amplifier can be added to allow a shaping of the signal before the trigger. The trigger starts the read out cycle of the transient recorder and resets a clock that measures the time since the last trigger. In a read out cycle the transient recorder typically records 1024 or 2048 channels and sends a read out request to the computer. An external timer prevents another trigger until the required pre-trigger channels for the next event have been acquired.

---

<sup>3</sup>This is necessary if the same heater is used for the test pulses and the stabilization. Without square rooter the pulser energy would depend on the offset heating power. Taking the square root of the current removes this dependency.



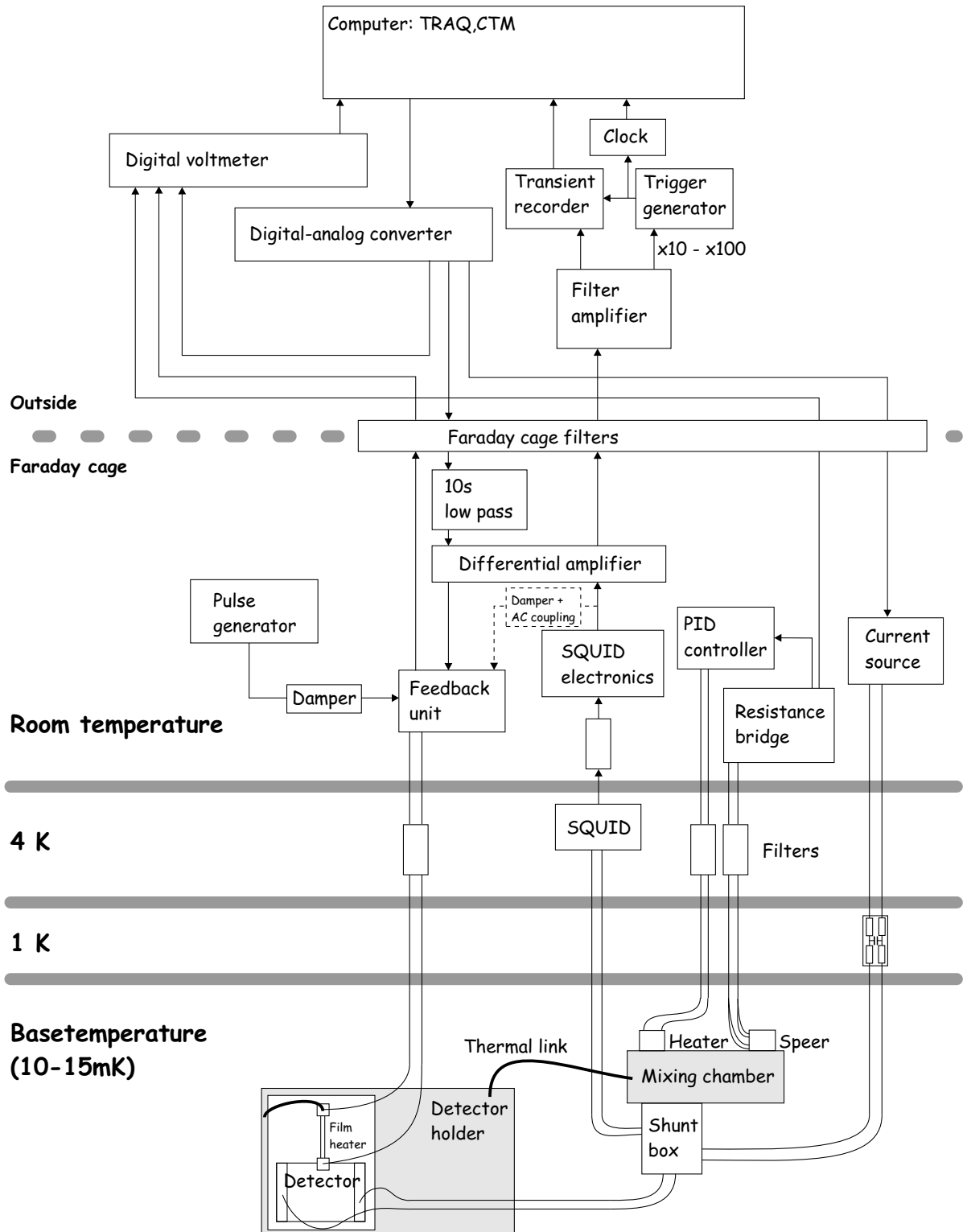


Figure 4.4: Schematic view of setup in the cryostat and the data acquisition system

### Computer control

For the control of the detectors and the data handling TRAQ and its subprograms can be used. They allow the setting of all parameters for the amplifiers, transient recorders and ADC channels. The CTM program reads out and displays selected DVM channels and thus can monitor the cryostat and detector operation. Additionally it can perform continuous sweeps of a chosen ADC channel to e.g. automatically scan a range of operating points of a detector.

### Control

One main problem when operating very sensitive detectors is the stabilization of the operating point ( $R_{op}$ ). If only one detector is run at a time it is usually sufficient to stabilize the temperature of the heat bath and use the bias current to heat the detector into the operating point<sup>4</sup>. But if two or more detectors with largely different operating temperatures<sup>5</sup> have to be run simultaneously this method may not be practical. Each detector has then to be stabilized independently.

The most sensitive measure for the operating point is the baseline of the detector itself. A direct feedback that takes the baseline and controls the film heater would assure a stable operation. However this method has to deal with two problems. Flux quantum losses, which basically occur when signals exceed the dynamical range of the SQUID, lead to ambiguous signals. Secondly the high pulse rates obscure the baseline. Therefore it is difficult to implement a hard wired solution that would lead to satisfactory results. For a software PID controller on the other hand, it is relatively easy to overcome these problems. The signal change for a flux quantum loss is well defined and can thus be ‘removed’ before further processing. Depending on the pulse duration and the pulse rate there is a chance of taking a sample of the baseline during a pulse in the detector. As the baseline has to be controlled to a fraction of the typical pulse height, this would degrade/prevent the stabilization. The control program therefore ‘freezes’ the baseline during a pulse in the detector. For each baseline sample taken, the control program reads out the clock to check the time since the last trigger. If this time is shorter than the blocking time (pulse duration) the sample was taken during a pulse and is rejected. If the elapsed time since the last trigger is longer than the blocking time the new sample is compared with the old sample. If the difference is a multiple of  $\Phi_0$  the program assumes that one or more flux quanta have been lost since the last sample and removes this offset<sup>6</sup>.

---

<sup>4</sup>In this case it is desirable to have negative electrothermal feedback ( $R_{op} > R_{shunt}$ ) to profit from the self stabilizing effects.

<sup>5</sup>In this work the transition temperatures of the  $\text{CaWO}_4$  detectors were 30–40 mK higher than the ones of the sapphire or silicon detectors

<sup>6</sup>The stability of the operating point from one sample to the next must be better than

With a sampling rate of  $> 1$  Hz a very good stability of the baseline can be achieved.

The control starts to break down when the pulse rate in the detector gets too high. If a new pulse comes before the previous one ended (pile-up) the time between valid samples can get very large. In this case the situation can be improved with the direct feedback mentioned in the section before. By introducing a fast feedback loop (dashed arrow in figure 4.4) the pulse duration can be shortened and pile-up effects reduced.

## 4.2.2 Holders & Sources

To measure the different detectors and their properties a variety of holders and sources was used. For the light detector measurements the 5.9 & 6.5 keV X-ray lines of manganese, as well as the 1.5 keV line of aluminium and the 4.5 & 4.9 keV lines of titanium were used. To excite scintillation light in the  $\text{CaWO}_4$  crystals and to measure the  $\text{CaWO}_4$  detectors  $^{57}\text{Co}$  (122 & 136 keV photons),  $^{60}\text{Co}$  (1.17 & 1.33 MeV photons) as well as  $^{241}\text{Am}$  (5.5 MeV  $\alpha$ s & 60 keV photons) were utilized.

### Scintillation Holders

To check the scintillation properties of the  $\text{CaWO}_4$  crystals and the different materials for the holders a simple scintillation holder was constructed. It consists of a white Teflon beaker for the crystal that serves as a diffuse reflector, and a cap for the light detector (see figure 4.5). In the beaker are a couple of Teflon supports to fix crystals of different shapes. A copper spring tip ensured thermal contact of the  $\text{CaWO}_4$  to the heat bath. Electrical connections for a thermometer on the  $\text{CaWO}_4$  crystal were not possible. On the inside thin reflective materials could be introduced to measure their reflective properties. The Teflon cap can be screwed onto the beaker to fully close the setup. In the cap a light detector can be mounted and electrically contacted. The light detector either rests on sapphire balls or is directly clamped between Teflon tongues. The Teflon enclosure has little holes to provide access for low energetic sources and alpha particles.

This holder is suited for small  $\text{CaWO}_4$  crystals ( $1 \times 2 \times 1 \text{ cm}^3$  max) and small light detectors ( $1 \times 2 \text{ cm}^2$  max). For bigger crystals and light detectors the holder described in chapter 3 was used.

---

$\pm 0.5\Phi_0$  for this algorithm to function properly.

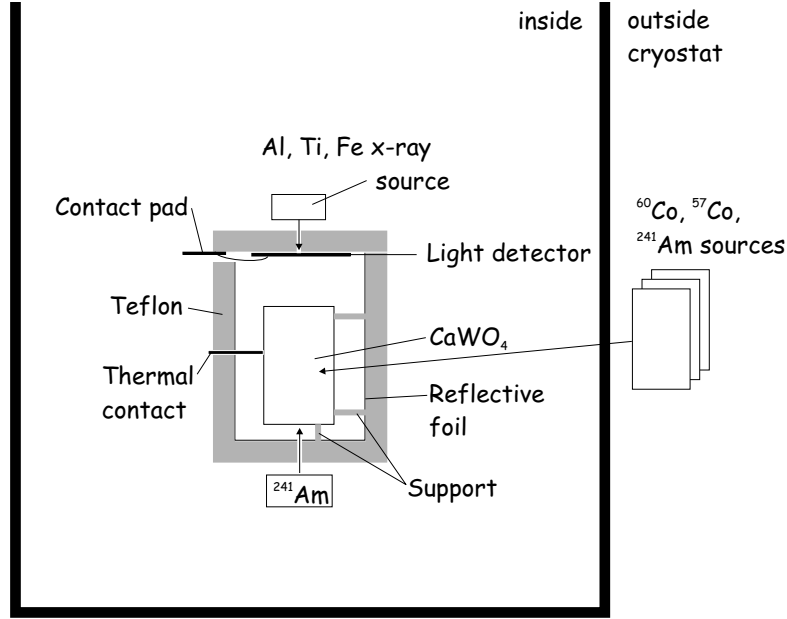


Figure 4.5: Holder and source setup for scintillation measurements

### Light Detector Holders

To test the light detectors stand alone with a low energy X-ray source and no scintillation light, a special variable copper holder was used (see figure 4.6). Four

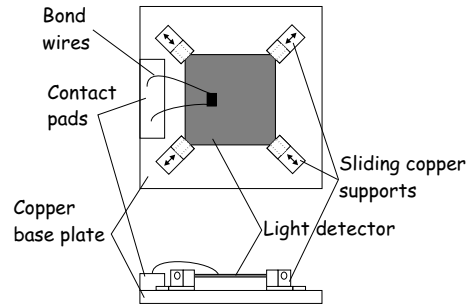


Figure 4.6: Holder for varying detector sizes (1–4 cm side length)

sliding copper supports fix the light detectors. To provide some flexibility and contraction compensation copper beryllium spring washers can be added underneath the supports.

For standard sized detectors ( $2 \times 1 \text{ cm}^2$  and  $2 \times 2 \text{ cm}^2$ ) the usual sapphire ball holders can be used. The slide rests on 3 sapphire balls. A spring loaded tip with a 4<sup>th</sup> sapphire ball presses down from the top to fix it (see fig 4.7).

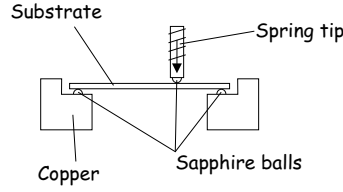


Figure 4.7: Schematic view of sapphire ball holder

## Sources

Figure 4.5 shows the principal arrangement of the sources. The low energetic sources for the calibration of the light detectors were mounted inside the cryostat directly illuminating the detector. Sometimes an alpha source was used to excite scintillation light in the  $\text{CaWO}_4$  crystal. This source also had to be mounted inside the cryostat next to the crystal. The other sources with high energy photons could be used from the outside. This has the advantage that they can be turned ‘on’ and ‘off’ and the rate can be varied during the experiment.

For the calibration of the light detectors the 6 keV X-rays from an iron source were usually too energetic. For this reason an Al/Ti fluorescence source was set up [Col95a]. Figure 4.8 shows a schematic view of it.  $^{55}\text{Fe}$  X-rays shine onto an

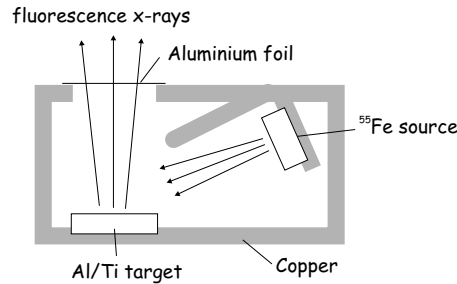


Figure 4.8: Fluorescence source setup.

aluminium target at a shallow angle. Photo absorption causes holes in the electronic shell of the target atoms and subsequent emission of characteristic X-rays (1.487 keV). The Al target has some titanium inlays to produce the corresponding X-rays (5.509 & 4.932 keV). The area ratio of Al to Ti was chosen to get similar count rates from both materials. At the exit window a thin aluminium foil ( $10\text{ }\mu\text{m}$ ) absorbs the emitted photo and Auger electrons that would otherwise cause a high background. Elastic scattering of the primary photons (Rayleigh scattering) lead to a certain amount of  $^{55}\text{Fe}$  X-rays in the spectrum.

# Chapter 5

## Results

### 5.1 Light Collection

To optimize the collection of the emitted light several tests of the individual parts were made. Different holders, materials and sizes of the crystals and detectors were measured. The absorption/reflectivity of the used materials and light detectors could be measured with a spectrometer and the setup described in section 4.1.3. But to get the absolute numbers of detected light for a holder/light detector combination, it had to be tested in a cryostat. For these measurements the  $\text{CaWO}_4$  crystals were installed in the holder and thermally attached to the heat sink. The scintillation light was excited with gamma and alpha sources. In this way the energies of the interactions causing the scintillation light were known and no thermometer for the phonon signal in the  $\text{CaWO}_4$  was needed. The light detector was connected to a SQUID to measure the light signal arising from the absorbed scintillation light. For energy calibration the light detector was illuminated with 6 keV photons from a  $^{55}\text{Fe}$  source (see figure 4.5). The following sections will discuss the investigated effects.

#### 5.1.1 Trapped light

Scintillation light in a crystal with  $n > 1$  can be totally reflected at the surface, depending on the angle of incidence. For simple geometries as a cuboid or a cylinder and only geometric propagation, this can happen at all surfaces (for a given photon). In a perfect crystal this photon is trapped and would be lost for the detection. In a real crystal however, scattering on the surfaces and in the bulk can change the direction of the photon. This will eventually lead to an ‘untrapping’. This happens at the cost of long paths of the light in the crystal. During this time the light can be absorbed. If it is absorbed before it can escape the light was

‘quasi trapped’. The effect is the same as if it was really trapped. This means that in a real detector crystal eternally trapped light does not exist, but photons can be absorbed before they can escape. The ratio of ‘quasi trapped’ versus ‘escaped’ is determined by the competition of elastic (scattering) and inelastic (absorption) interactions in the crystal.

In the case of  $\text{CaWO}_4$  with  $n = 1.92$ , a large fraction of the light is potentially trapped. In a cuboid this is a constant part of about 60 % of the initially emitted light. To check which part of these 60 % is absorbed in the crystal, the light output of a  $2 \times 1 \times 0.5 \text{ cm}^3$  cuboid and a special shaped  $\text{CaWO}_4$  (see figure 5.1) were compared. In the second  $\text{CaWO}_4$  no infinite light paths exist, that means

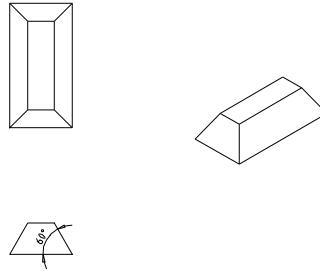


Figure 5.1:  $\text{CaWO}_4$  with a special shape that allows no infinite light paths in the crystal (trapped light).

every photon can be totally reflected 3 times at most before it hits a surface at an angle that allows it to escape. A comparison of the measured light yields of the two crystals gave no significant difference. This means the scattering dominates over the absorption and no ‘quasi trapped’ light exists in the crystal.

A second independent test of this fact was done with the 4 cm cylindric crystals that will be used for the real detector modules. In a cylinder the trapped light fraction depends on the radial position of the light emission in the crystal. It varies from  $\approx 1/3$  on the axis to  $3/4$  close to the cylinder wall. This spatial dependence can smear out the energy resolution in the light channel. To test this effect different sources were used to excite the  $\text{CaWO}_4$ . The 122 keV (136 keV) gammas of a  $^{57}\text{Co}$  source have a range of a few mm in the crystal. By changing the position of this source one can probe different spots on the surface. Points on the cylindric wall and on the axis of the crystal showed no difference within the resolution (16 %). To double check a  $^{60}\text{Co}$  source with 1.17 MeV and 1.33 MeV was used. These gammas have a penetration depths of a few centimeters in  $\text{CaWO}_4$  and thus illuminate the entire crystal. A resolution of  $\approx 10\%$  for the peaks was found, indicating no significant spatial dependence due to trapped light.

The resolution of the gamma lines in the light detector is a combination of the intrinsic resolution of the light detector (3–5 %), photon statistics of the collected scintillation light (depends on energy:  $\approx 5\%$  for 122 keV) and remnant spatial

dependence in the crystal or the collection efficiency of the holder. To account for the measured resolution the combined effect can be estimated to be in the order of  $\approx 8\%$  for the used crystals and holders. The simulations of the holder in chapter 6 indicate a spatial dependence in the crystal in the order of a few %. The collection efficiency of the holder is almost independent of the position. Therefore the contribution of spatial effects to the resolution is most likely to be due to slight ‘trapped light’ effects in the crystal.

The light yield can not only vary within a crystal but also from one crystal to another. This can be due to a larger/smaller absorption in the crystals or a different scintillation efficiency for each crystal. For the tested  $\text{CaWO}_4$  differences of up to a factor of 2 were found [Kee01, Don01].

### 5.1.2 Reflector

Once the light has left the crystal it must be collected in the light collector. As already pointed out in a previous section, focusing is not an option. One therefore has to rely on a good low loss reflector that reflects the photons until they eventually get absorbed the light detector. Teflon and a special multilayer mirror foil were tested for this purpose. Teflon makes a low loss reflector but can not be used in excessive amounts in our detectors (see chapter 3). Therefore it is used for parts of the holder that mechanically hold the crystals and extend inside the reflector. The main part of the reflector consists of a mirror foil that reflects better than 98 % for all angles and polarities. The foil used in this work had a cut off at 390 nm and thus covered only 87 % (of the energy) of the scintillation light peak of  $\text{CaWO}_4$ . Figure 5.2 shows the results of a new prototype foil with good reflectivity down to 350 nm wavelength. This will increase the collection efficiency for the higher energetic scintillation photons. An increase of  $\approx 15\%$  of the detected energy can be anticipated by this.

### 5.1.3 Absorption

After collecting the light it has to be absorbed in the light detector in order to be detected. To optimize this detection process the light detector absorber has to be as ‘black’ as possible for the scintillation photons. Silicon and sapphire wafers have been tried as absorbers. The standard sapphire wafers are transparent for the scintillation light and need a special absorption layer.

A standard untreated silicon wafer absorbs 60 % of the light. Measurements with an ‘integrating sphere’ (see section 4.1.3) confirm this number. A special surface treatment [Kin91] can cut the reflectivity by a factor of two and thus increase the absorption to 80 %. With a wet etching solution the surface of the substrate



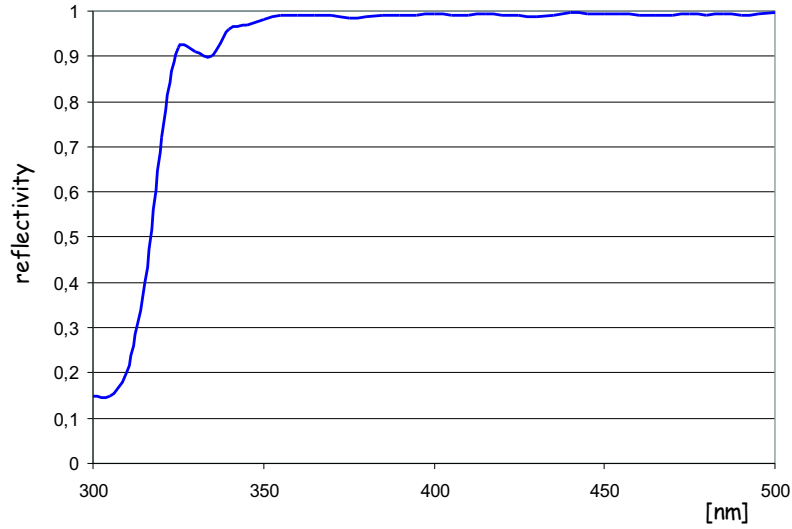


Figure 5.2: Measured reflectivity of a prototype mirror foil currently under development at the 3M company. It has a reflectivity of 97 % or better for wavelengths  $> 350$  nm [Mir02].

is roughened. The etching works preferably along the crystal axes and in this way creates tetraedric shapes on the surface. Now an incident photon that gets reflected the first time usually hits the silicon a second time. This enhances the chances of the photon being absorbed. Direct measurement of the absorption gave a value of 70 %. A comparison of treated and untreated light detectors [DiS02] in the real detector module with a 300 g  $\text{CaWO}_4$  gave an even slightly better result (see table 5.1 setup 5 & 6).

Sputtered silicon layers on the sapphire wafers gave a slightly worse absorption (56 %) than a pure silicon wafer. When measuring the absorption through the sapphire (see figure 5.3) this value increases to 80 %. An incident photon that is not absorbed, but diffusively reflected on the silicon layer with a new direction can be totally reflected on the sapphire surface. It then has a second chance to be absorbed in the silicon layer. In the real detector setup both sides of the light detector absorb the light, with the side facing the  $\text{CaWO}_4$  being dominant (see section 6.1). The average absorption thus can be estimated to be around 70 %. But measurements showed (see table 5.1 setup 4) that the detected light signal was even smaller than for a pure silicon wafer. This indicates that the high frequency phonons created in the absorption layer partially decay in this layer before they can escape into the sapphire slide. A dedicated measurement to confirm this has yet to be carried out.

For the sapphire light detectors other absorption layers than silicon have been considered as well.  $\text{SiO}$  is a good candidate. It is easy to sputter and showed good

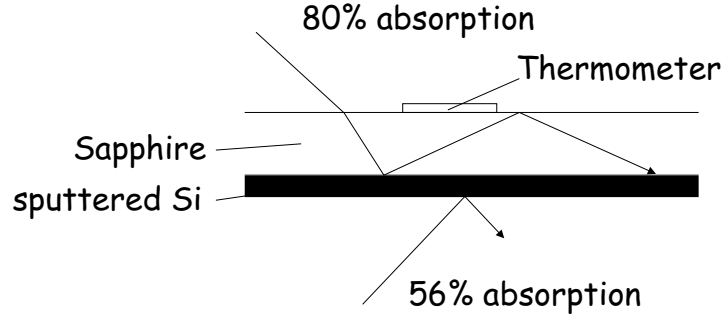


Figure 5.3: Absorption of a sputtered silicon layer on a sapphire substrate. A non specular reflection of the silicon layer can greatly increase the absorption observed from the ‘sapphire side’.

adhesion. Tested  $1.7\ \mu\text{m}$  thick  $\text{SiO}$  films on glass substrates showed an absorption of up to 90 % in the required range. Thinner films ( $0.5\ \mu\text{m}$ ) on sapphire light detectors absorbed slightly below 70 %. But so far detectors with such an absorption layer have lost their transitions. The reasons for that are not understood, but it might be that the amorphous films have a very big heat leak that prevents the detectors from cooling to the required temperature. That is supported by the observation that a detector where the  $\text{SiO}$  was removed started working again.

Other absorption layers particularly from photovoltaic applications could be possible candidates. But usually they require complicated processes and/or high temperatures. Requirements that can spoil the radiopurity or the transitions of the detectors.

From the absorption point of view the silicon light detectors are superior. The absorption layers needed on sapphire detectors have a high potential<sup>1</sup> but introduce additional processing steps during the manufacturing, and an additional boundary for the phonons.

Table 5.1 compiles the results of the various measurements of different setups. Setup I is the proof-of-principle measurement [Meu99]. It was done with a  $2 \times 1 \times 0.5\ \text{cm}^3$   $\text{CaWO}_4$  crystal with a glued W-thermometer. A  $2 \times 1\ \text{cm}^2$  sapphire slide with a Si light absorption layer served as light detector<sup>2</sup>. The entire setup was housed in a copper holder. Two Al mirrors opposite of the light detector improved the light detection. In this way 0.8 % of the energy deposited in the  $\text{CaWO}_4$  crystal could be detected in the form of scintillation light. Number II was done in a different holder. Instead of having two mirrors for the light collection the holder was made of Teflon and fully enclosed the  $\text{CaWO}_4$  and the light detector.

<sup>1</sup>One can add layers on a silicon slide as well to further improve the absorption, but would suffer from the same disadvantages as in the case of sapphire.

<sup>2</sup>The holding structure covered part of the detector. In table 5.1 the (smaller) effective area is given.

setup	reflector	light detector [ $mm^2$ ]	detected light
I	Al-mirrors	sapphire $20 \times 10$	0.8%
II	Teflon	sapphire $13 \times 10$	1.2%
1	Teflon	sapphire $13 \times 10$	0.33%
2	Teflon	sapphire $20 \times 10$	0.52%
3	Teflon&foil	sapphire $20 \times 10$	0.68%
4	foil bilayer	sapphire $20 \times 20$	0.5%
5	foil bilayer	silicon $20 \times 20$	0.55%
6	foil bilayer	silicon $20 \times 20$ etched	0.7%
7	foil bilayer	silicon $30 \times 30$	1.3%

Table 5.1: I,II measured with 6 g  $\text{CaWO}_4$ , the rest with two different 300 g  $\text{CaWO}_4$ , detected light is the fraction of the total energy deposited in the  $\text{CaWO}_4$  that is detected in the light detector.

This improvement of the reflector lead to a 50 % increase of the detected light energy.

Measurements 1–7 were made with the 4 cm cylindric crystals in the holders that will be used for the detector modules at Gran Sasso. It is apparent, that a silicon light detector detects more light energy than a sapphire of the same size with a silicon layer on one side. Especially if the surface of the silicon is etched to reduce the reflectivity. The absolute maximum fraction of the total energy seen in the light channel was achieved with a  $3 \times 3$  cm silicon detector.

Between measurement 3 and 4 the  $\text{CaWO}_4$  crystal was changed. A comparison of the detected light and the detector sizes reveals that the light output of the second crystal was a lot smaller. Cross checks with different reflector setups and  $\text{CaWO}_4$  crystals confirmed that supposition. The light output for crystals of different quality changed by a factor of two. Whether crystals of minor quality create less light in the first place or absorb more of their own scintillation is not 100 % clarified. Optical tests show that some crystals clearly are less transparent<sup>3</sup>. Nonetheless the total effect can be a combination of the two.

## 5.2 Light Detectors

The important properties of a light detector, besides the absorption, are the minimum amount of energy that can be measured (threshold) and the uniformity of the response in the thin substrates (energy losses due to phonon decay). To measure the threshold detectors were irradiated with low energetic X-rays (1.5–

---

<sup>3</sup>Part of this can be due to scattering in the crystal rather than absorption

6 keV). With the signal height for a known energy one could extrapolate down to the observed noise and determine the threshold. Another possibility is to calibrate electric heater pulses against the X-rays. Then it is possible to inject heater pulses of very low energy and observe when they start to rise above the noise. In this way it is possible to directly measure the threshold. To determine the losses in the substrates the light detectors were irradiated in two/three spots with different distances to the thermometer. By comparing the pulse heights and resolutions of the different positions the losses in the substrates can be derived.

### 5.2.1 Uniformity

In thin substrates the phonons created by an event far from the thermometer need to scatter on the surfaces many times before they reach the thermometer. Each scattering can lead to a decay of the non-thermal phonons. The non-thermal phonon flux from events far from the thermometer will thus be reduced and lead to a non-uniform response of the detector.

The first test was made with a  $40 \times 40 \times 0.4 \text{ mm}^3$  sapphire detector, with a  $^{55}\text{Fe}$  source illuminating three different spots. One close to the center and the thermometer, one close to the rim about 2 cm from the center, and one in between. The sizes of the collimating holes were different to be able to associate peaks in the spectrum with the position on the sapphire slide. Figure 5.4 shows the sum spectrum of all holes. The  $k_\alpha$  and  $k_\beta$  lines have a FWHM of 148 eV. Within the

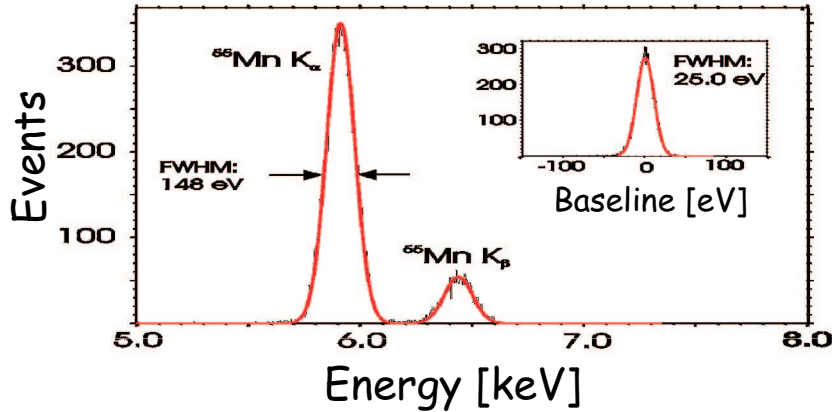


Figure 5.4:  $^{55}\text{Fe}$  spectrum of a  $40 \times 40 \times 0.4 \text{ mm}^3$  sapphire detector irradiated at three different positions. The insert shows the baseline noise amplitude.

limit of this resolution the contributions from the different holes could not be separated. This means the losses for an event 2 cm from the thermometer are less than 2.5 % of the total energy.

The tests were repeated with a  $20 \times 20 \text{ mm}^2$  sapphire detector with silicon absorption layer and a silicon detector, respectively. The two illuminated spots were about 1 cm apart.

In both cases two sets of  $k_\alpha, k_\beta$  lines for the holes can be found. In the sapphire detector the resolution for the  $k_\alpha$  line from one hole is about 180 eV. The two sets are 600 eV or 10 % of the pulse height apart. Compared with the situation on the blank sapphire this is a  $\geq 8$  fold increase of the losses in the absorber. The effect on the resolution is only about 30 %. In the silicon detector the spatial dependence was slightly larger. The sets were separated by 700 eV or 12 % of the pulse height. The resolution for one hole was 300 eV. From these numbers it is obvious that the absorption layer on the sapphire increases the losses. This may be due to the sputtered silicon layer itself or to the altered surface of the sapphire. To get a reasonable adhesion of the silicon the sapphire has to be cleaned with the ion gun prior to the sputtering. This ion bombardment destroys the crystalline structure of the surface and can lead to an increased decay rate of the surface scattered phonons. Still the losses are less severe than in the case of a silicon substrate. The implications of this spatial dependence on the (maximum) detector size and the performance of the entire module will be investigated in section 6.1

### Scintillation time

When comparing the pulse shapes from different events in the light detector it becomes apparent, that the rise time for light events is a lot longer than for X-ray hits (figure 5.5). The rise time of the X-ray hits is in the order of some  $15 \mu\text{s}$ , whereas the scintillation light signal has a rise time of about  $75 \mu\text{s}$ . This is attributed to the slow scintillation decay time in  $\text{CaWO}_4$ . The result was found independently of the used light detector. In the past decay times between  $0.5 \mu\text{s}$  [Gil49] and  $20 \mu\text{s}$  [Bel50] have been reported. The light emission of the  $\text{CaWO}_4$  crystals at mK temperatures is even slower. This must be taken into account for the design of the light detectors. The decay time of the signal must be considerably longer than  $75 \mu\text{s}$  in order to integrate the energy of the incoming photon flux.

### 5.2.2 Threshold

The threshold of a detector is determined by the baseline noise. The noise is a combination of the different sources, e.g. Johnson, phonon and SQUID noise. For a given detector the amplitude of the baseline noise can be measured and expressed in energy. The insert in figure 5.4 shows the distribution of the baseline noise for a  $40 \times 40 \text{ mm}^2$  sapphire detector. The distribution is well represented by a Gaussian centred around zero with a FWHM of 25 eV. Experience with the sapphire detectors from CRESST I showed that a value of  $5\sigma$  of this baseline

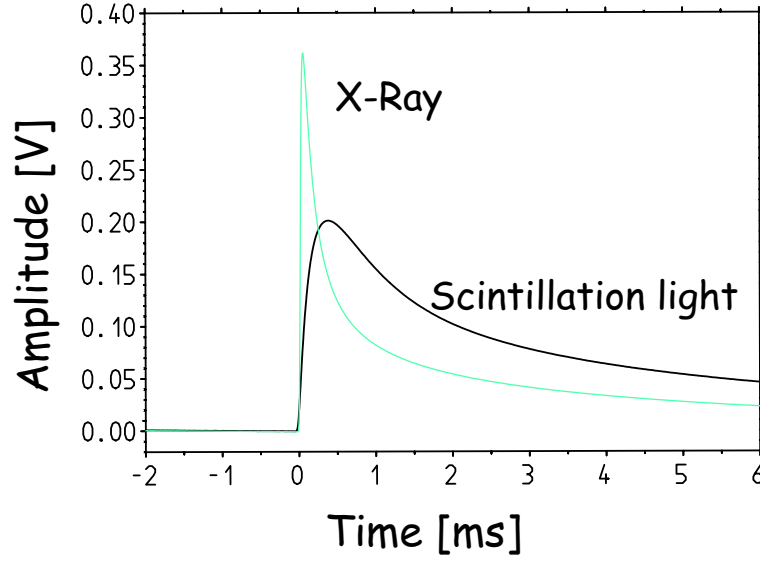


Figure 5.5: Pulses in the light detector. The pulse with the fast rise and decay time is due to the direct hit of calibration X-ray. The pulse with the slow risetime is caused by scintillation light.

noise is a realistic threshold. Triggering at this level well separates noise and pulses. For the light detectors this  $5\sigma$  level will be used as the threshold stated.

The noise sources can be separated into two groups, the current like noise and the energy like noise. Current like noise originates in the readout circuit and the SQUID. They form a constant noise level. Energy like noise directly originates in the detector itself, like phonon noise. Making a detector more sensitive and thus increasing the signal height will improve the situation with respect to the current like noise. The noise stays the same and the relative importance drops as the signal amplitude increases. Energy like noise on the other hand is amplified in the same way as the signal and the signal to energy like noise will remain on the same level. However the contribution from phonon noise is only some 2 eV for detectors of a few  $\text{mm}^2$  at mK temperatures. A better threshold can therefore be expected by an increased sensitivity.

### Concept

The idea for the new, more sensitive, light detectors is the use of phonon collectors. In this way one can keep the size of the thermometer and thus the absorbed amount of non-thermal phonons constant and at the same time reduce the heat capacity. The reduced heat capacity of the thermometer will then lead to a higher temperature signal. To be able to keep the standard design and manufacturing processes of the thermometers, the phonon collectors are done by enlarging the

aluminium pads needed for the electrical connections. The aluminium pad together with the underlying tungsten film forms a proximity bilayer with a transition temperature close to the one of pure aluminium. At the mK operating temperatures of the sensor the heat capacity of this bilayer negligible. To give the small thermometers a long enough thermal time constant a new coupling scheme was developed. A thin gold film defines the thermal coupling strength of the detector to the heat bath. A second problem for thermometer films with a very low heat capacity is the bond wire heater usually used for the CRESST detectors. It will dominate the heat capacity. It was therefore replaced by film heaters [Mei99].

### Detector ‘Film heaters’

The concept of film heaters and film coupling was tested with a thermometer with the geometry and dimensions shown in figure 5.6. The film heaters are located

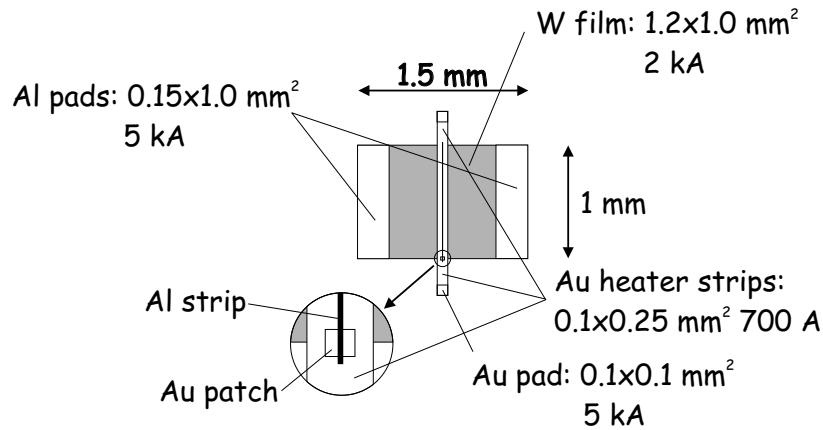


Figure 5.6: Sketch of the test detector for the film heaters and coupling design. Both gold films act as heaters. For the coupling a gold bond wire is bonded to the pad at the end of one of the strips.

on both sides of the tungsten thermometer<sup>4</sup>. They are electrically contacted by aluminium wires bonded to the gold pads at each film heater. In this way the heater current is drawn from one side of the thermometer to the other. The readout current for the thermometer runs perpendicular from one aluminium pad to the other. To avoid crosstalk of the heater and the readout current a thin aluminium strip was evaporated across the tungsten film. This strip eliminates any voltage drop between the heaters across the film and thus avoids a coupling

<sup>4</sup>In reality the heaters are one single gold strip, with the part on top of the tungsten thermometer being electrically shortened by an aluminium strip. In this way only the two parts extending besides the thermometer are resistive and are treated as two individual heaters.

of the heater current into the readout loop. One of the two heaters acts as the coupling to the heat sink. A gold wire bonded to the pad and the copper holder heat sinks the pad to the holder. The gold wire has a much higher thermal conductance, therefore the coupling strength is determined by the resistance of the gold strip at the operating temperature of the detector.

Figure 5.7 shows the transition of the detector with two heater strips. The left transition curve is recorded with zero heating current through the film heaters and a varying heat sink temperature. The x-axis is calibrated in temperature. The second transition is recorded at a fixed heat sink temperature and a varying

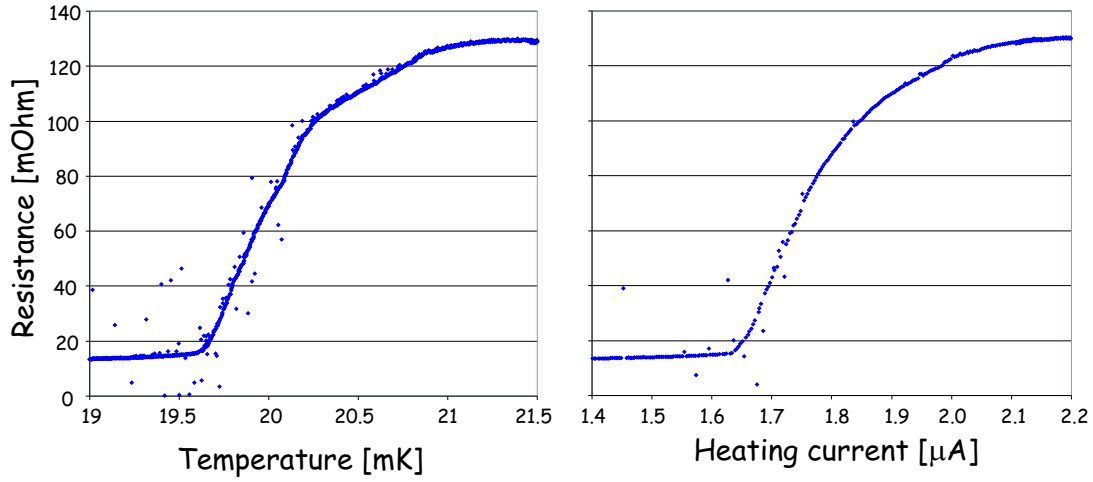


Figure 5.7: Transition curves of the ‘Film heater’ detector recorded with  $1 \mu\text{A}$ . The left curve was recorded by sweeping the heat sink temperature, the right curve by sweeping the heating current (heat sink stabilized at  $17.3 \text{ mK}$ ).

heating current through the film heaters. The x-axis shows the heating current. The first graph allows to judge the quality/width of the transition and provides an absolute calibration of the temperature excursions caused by an energy deposition. The second graph is useful to choose a point for the operation of the detector. During the operation the detector is run with a constant heat sink temperature and the stabilization is achieved with the film heaters. From the two graphs the actual heater resistance can be estimated. With the temperature difference between the heat sink and a given point in the transition plus the known heating current to achieve this difference one can derive the resistance<sup>5</sup>:

$$R_H = \sqrt{\frac{L}{\alpha I_H^2} (T_{Th}^2 - T_B^2)} \quad (5.1)$$

<sup>5</sup>The heating power and the flow to the heat sink have to be in equilibriums. The heat flow through a cross section of the heater to the heat sink has to be the dissipated heating power ‘on the other side’ of this cross section:  $-A\kappa \frac{dT}{dx} = I_H^2 R (\alpha^* + \frac{L-x}{L})$ . Integrating this equation and using the Wiedemann-Franz law gives the above relation.



$R_H$	...	Heater resistance
$L$	...	Lorenz number
$I_H$	...	Heater current
$T_B$	...	Bath temperature
$T_{Th}$	...	Thermometer temperature
$\alpha$	...	Geometry factor. 1: one heater; 2: separate heater and coupling; 3: two heaters

For this detector the heater resistance is about  $0.5\ \Omega$ . The room temperature resistance is roughly  $2\ \Omega$ <sup>6</sup> yielding an RRR<sup>7</sup> of 4. To avoid systematic errors due to self heating of the thermometer film, the readout current should be as low as possible.

In figure 5.8 an averaged 1.5 keV X-ray pulse is shown. The insert shows a heater pulse of the same energy. The decay time constant of the particle pulse is  $1.4(2)$  ms the one of the heater pulse about 30 % shorter. The calculated time constant at the bottom of the transition is  $\tau = C/G$  is 0.8 ms. This is in agreement with the heater pulse time constant. The longer time constant of the X-ray pulse originates

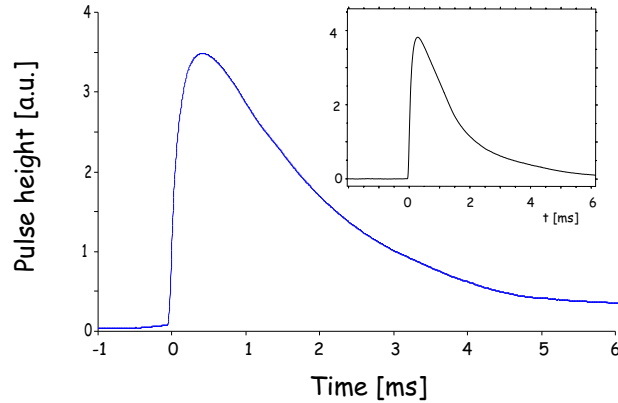


Figure 5.8: Averaged 1.5 keV X-ray pulse of the ‘Film heater’ detector. The insert shows a heater pulse of the same energy.

from the thermal signal from the sapphire crystal. This part is negligible in the heater pulse, as the phonons are directly injected into the thermometer.

A measured spectrum is shown in figure 5.9. The resolutions of the lines is 125 eV @ 1.5 keV and 175 eV @ 6 keV. The baseline has a width of 48 eV. Using the 1.5 keV line for calibration, a linear extrapolation results in a 10 % error for the

<sup>6</sup>The calculated resistance using the bulk resistivity of gold is  $0.8\ \Omega$ .

<sup>7</sup>Residual Resistance Ratio

Mn lines. This is due to non-linearities and a beginning saturation for the high energetic lines.

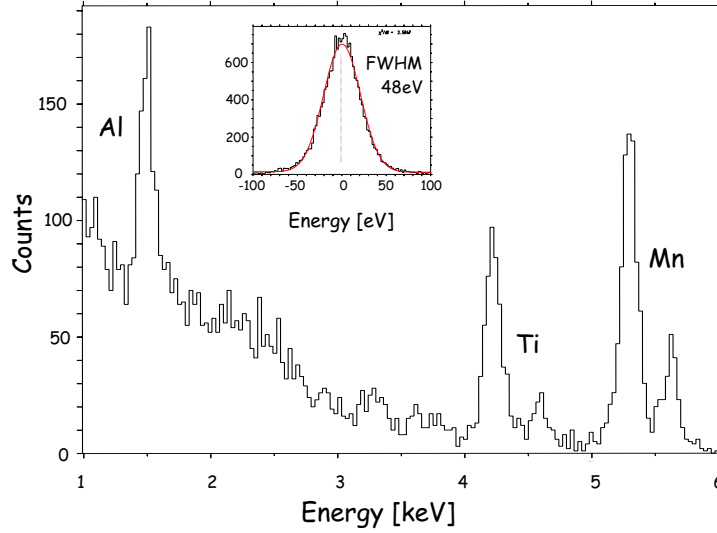


Figure 5.9: Spectrum taken with fluorescence source shining on detector. The insert shows the width of the baseline in eV.

A main disadvantage of evaporated film heaters over bond wire heaters is the direct contact to the substrate. Via this contact area and the Kapitza coupling the heater not only injects phonons into the film, but into the substrate as well. Past experiments [Mei99] have shown a dependence of this coupling strength on the injected energy. High energies mean a ‘hot’ heater and thus a stronger thermal coupling to the substrate. This coupling may also be varied by fluctuations of the heat sink temperature. The stabilization requires a change of the heater current and therefore leads to a different heater temperature. To check the importance of this effect at energies ( $< 1$  keV) relevant for the light detectors, the detector was stabilized in its working point using the film heaters. At the same time the heat sink temperature was swept up and down between 13 and 18 mK. Figure 5.10 shows the amplitude of a 1.5 keV pulser against the heat sink temperature. Within the resolution no change of amplitude or pulse shape could be observed. For the actual operation of the detector with remnant heat sink temperature fluctuations in the order of  $\mu\text{K}$  and pulser amplitudes of  $< 1$  keV the effect of the variable coupling of the heater to the substrate can be neglected.

### Detector ‘Phonon collectors’

After this proof of the feasibility to use sputtered gold films as heaters and coupling, the next step was to reduce the heat capacity of the thermometer. Figure

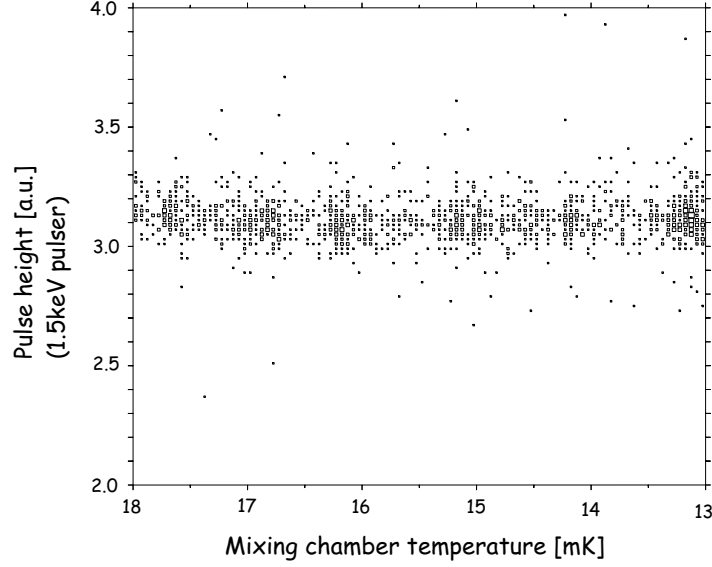


Figure 5.10: Heater amplitude with varying mixing chamber temperature.

5.11 shows the altered geometry. The aluminium pads for the electrical connection have been enlarged and act as phonon collectors. The heater/coupling gold strips were replaced by a single strip of greater length. The total heat capacity of the tungsten film and the gold strip is  $0.05 \text{ pJ/K}$  which is a factor of five lower than for the previous thermometer with the same outer dimensions. The length of the coupling gold strip was increased accordingly to obtain the same time constant.

The aluminum pads and the underlying tungsten film form a proximity bilayer with a vanishing heat capacity at the operating temperature. The geometry of the remaining tungsten layer yields lower resistance than the commonly used thermometers. The shunt was therefore replaced by a  $5 \text{ m}\Omega$  resistor. The transition of the detector is shown in figure 5.12. The 10%–90% width of the transition is about  $0.3 \text{ mK}$ . The heater resistance was calculated with equation 5.1 to be  $2.4(2) \Omega^8$ .

The heat capacity together with the transition width limited the dynamic range of this detector. Energies higher than this dynamic range heat the thermometer all the way through its transition. The pulse height saturates and no information about the energy can be obtained from the pulse height. The information about the energy is still contained in the pulse shape, e.g. the time it takes for the pulse to return to the baseline, and can be extracted. Other groups have already demonstrated the feasibility of this method [Fig00]. With bias currents of a few  $\mu\text{A}$  the maximum energy measurable before the detector was heated through the

<sup>8</sup>The resistance at room temperature is  $9.2 \Omega \rightarrow \text{RRR} = 3.8$

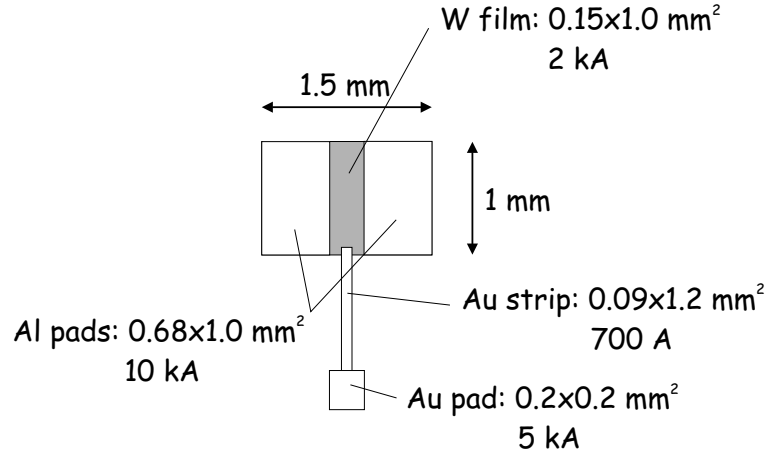


Figure 5.11: Dimensions of detector with collector pads. The ‘twosided’ film heater was replaced by a single strip.

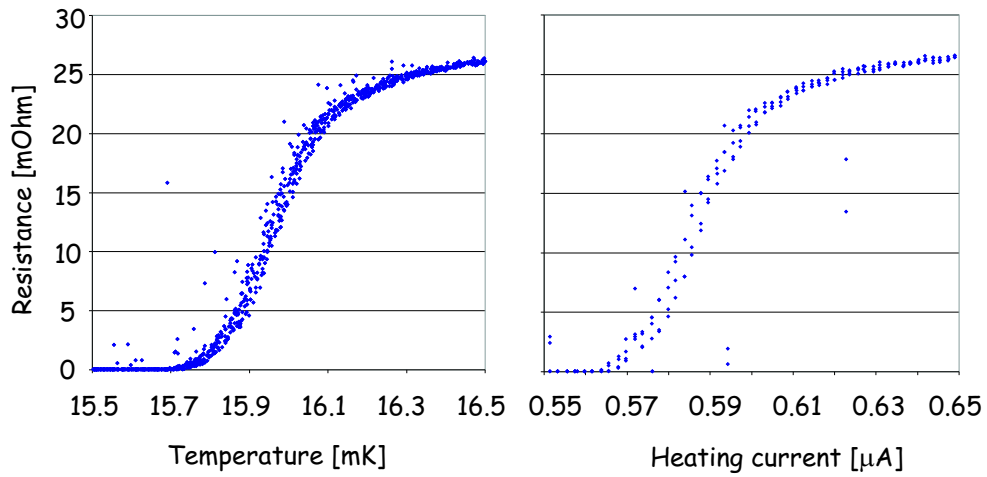


Figure 5.12: Transition curves of the ‘Phonon collectors’ detector recorded with  $1 \mu\text{A}$ . The left curve was recorded by sweeping the heat sink temperature, the right curve by stabilizing the heat sink at 12.9 mK and sweeping the heating current.

transition was  $< 1.5$  keV. To be still able to measure higher energies and calibrate the heater without using this technique the baseline of the detector was stabilized below the transition. Now only the peaks of the pulses appear in the transition. Figure 5.13 shows a measured 6 keV spectrum. The resolution of the  $k_\alpha$  line is 175 eV. In this operation mode the real baseline of the detector is not visible in

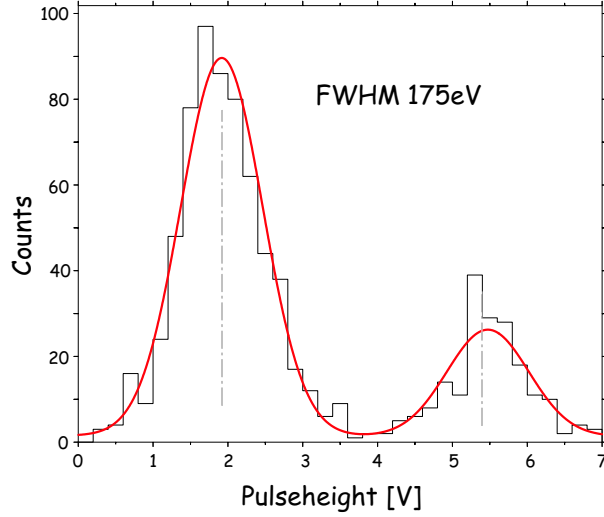


Figure 5.13: 6 keV spectrum recorded with  $1 \mu\text{A}$ .

the pulses and fluctuations of the detector directly map into the peak width. The ‘real’ resolution of the detector might therefore be better than the measured one.

Running the detector in the transition and applying the before mentioned method to determine the pulse height by just taking the pulse duration yields worse results. An improved approach with calibrated pulse shapes for all different energies as suggested in [Fig00] requires a careful scan of the desired dynamic range with heater pulses. These heater pulses have to exactly match the particle pulses and serve as calibration. Figure 5.14 shows that the particle and the heater pulses do not have the same shape for this detector. Therefore this method can not be used without ‘designing’ special heater pulse shapes, so that the resulting heater pulses exactly resemble the particle pulses. On the other hand it has to be said, that a dynamic range of below 1 keV is well sufficient for a dark matter run. Energy deposits in the order of the expected WIMP recoils of some 20 keV result in a few 100 eV of measured light signal (for background gammas). A higher threshold would only be desirable for the calibration of the detector modules and for the (easy) identification of high energetic background.

Looking at the low energy part of the spectrum one finds a baseline resolution of 25 eV and a resolution of 33 eV for a 100 eV pulser (both FWHM). These values were obtained when measuring the detector with a bias current of  $4 \mu\text{A}$ . Decreasing the bias current to  $0.1 \mu\text{A}$  improves this to 14 eV for the baseline and

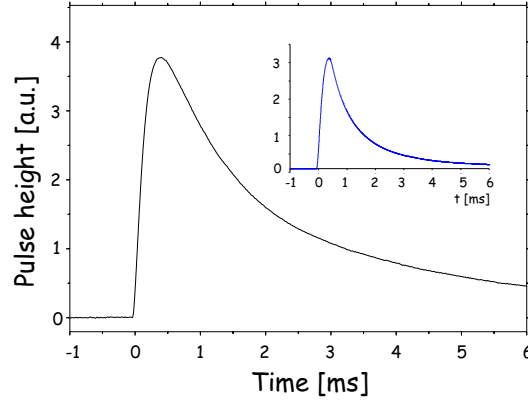


Figure 5.14: Averaged 1.5 keV pulse for the ‘Phonon collectors’ detector. The pulses were recorded with a bias current of  $30 \mu\text{A}$  to broaden the transition and give a sufficient dynamic range. The insert shows a averaged 1.5 keV pulser event. The decay time is again shorter than the one of the particle pulse.

13 eV for the pulser (figure 5.15). This seems to indicate a certain bias current dependent excess noise in the thermometer.

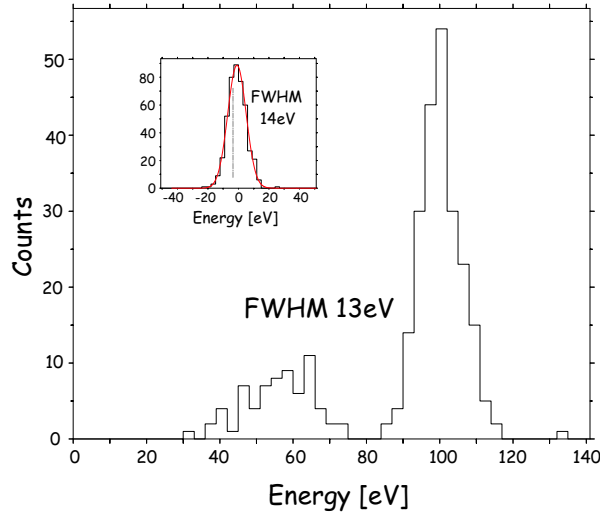


Figure 5.15: 100 eV pulser and baseline (insert) recorded with  $0.1 \mu\text{A}$  bias current.

The disadvantage of very low read out currents is a very narrow transition. Figure 5.16 shows the transition recorded with  $0.1 \mu\text{A}$ . The 10 %–90 % width is  $0.07 \text{ mK}$ . The measured temperature increase for a 100 eV event is  $33(3) \mu\text{K}$ . This results in a dynamic range of about 200 eV.

As a conclusion one can say that the light detectors with a gold film as coupling and heater and enlarged aluminium pads as phonon collectors work very good.

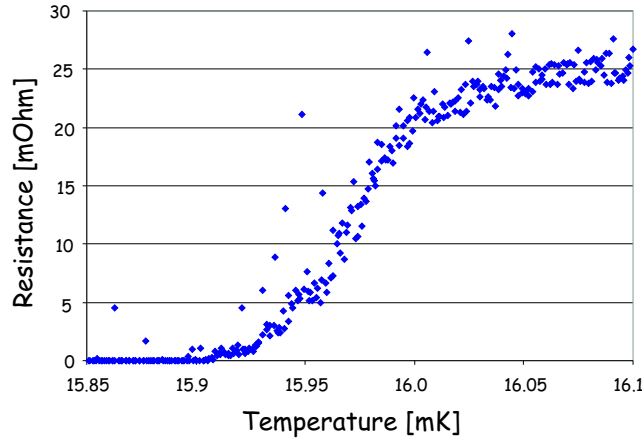


Figure 5.16: Transition recorded with a bias current of  $0.1 \mu\text{A}$ . The transition width is  $0.07 \text{ mK}$  (10 %–90 %).

The coupling of the detectors can easily be designed. At the same time the gold film provides a heater that allows to inject pulses into the thermometer to monitor the stable operation over extended periods. The phonon collectors increase the temperature excursions caused by a given energy. The gain of the detector with collectors compared to the one without is almost a factor of 7. This is even more than the decrease of a factor of 5 in heat capacity. This can be explained by the better absorption of the phonons in the collectors (100 %) compared to the tungsten film ( $\approx 30 \%$ ) [Loi99]. The improvement in threshold as in respect to previous detectors was not as much as expected if the detectors were dominated by current like noise (Johnson and SQUID noise). Energy like excess noise must be present in the detectors. The  $5\sigma$  threshold of the detector with the phonon collectors was determined to be  $30 \text{ eV}$ . For a complete module with 1.3 % of the total energy in the light channel (table 5.1) this corresponds to a threshold of  $2.3 \text{ keV}$ !

The energy like excess noise found in the detectors was not investigated. There are hints that part of it may be connected to the read out current of the thermometer. Another source may be long lived excitations in sapphire. These are since long expected to limit the resolution achievable with sapphire substrate based detectors and have been found in other works [Höh98]. Phonons created in sapphire after an energy deposition excite some long lived states and in this way are lost for the measurement. But this process not only is a drain for phonons, it is a source as well. When the excitations eventually relax back, they release the bound energy and are a source of energy that disturbs the baseline.

As next steps to further improve the performance of the detectors other substrates may be tested with this thermometer design. This could shed some light on the subject of the excess noise. Secondly non-transparent substrates like Silicon may

prove a more natural choice for a light detector. They do not need any additional absorption layers and their performance is comparable (phonon losses) or even better (absorptivity) than sapphire. To match the resistance of the thermometer to the shunt resistors used in the setup at Gran Sasso, the W-film geometry could be altered, e.g. by changing the width-length ratio and/or making the W-film thinner. Another improvement may be a separation of heater and coupling. By having two individual Gold films one could change the coupling without affecting the heater resistance. A similar response of the detectors can be an advantage if multiple detectors have to be run at the same time.

### 5.3 Phonon & Light

To determine the performance of the two detector channels combined to a detector module, several coincident measurements with the 300 g  $\text{CaWO}_4$  crystals were done in Munich (figure 5.17). All of these measurements were still done using

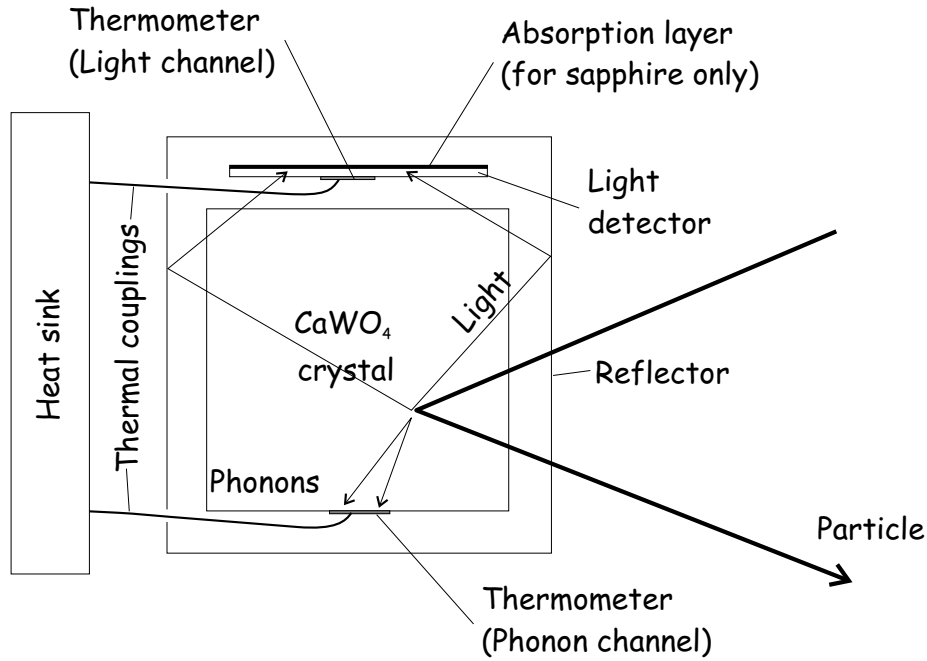


Figure 5.17: Sketch of the setup used for coincident measurements of the phonon and light signal. The mechanical support of the two detectors inside the reflector (not shown) was done with teflon, to thermally insulate the detectors from the heat sink. The only (defined) thermal coupling is provided by the gold bond wires between the detectors and the heat sink.

light detectors with the old detector layout, i.e. no phonon collectors and normal



bond wire heaters and coupling. The  $\text{CaWO}_4$  crystal was equipped with a W-film in the usual CRESST I design with a transition temperature of  $\approx 50$  mK. The recent developments of phonon collectors for the light detectors and phonon detectors [Sta], and transition temperature decreasing evaporation techniques for the W-films on the  $\text{CaWO}_4$  were not available at this time. Figures 5.18 and 5.19 show the  $^{60}\text{Co}$  spectra recorded with a complete module. Figure 5.18 was recorded with the thermometer on the  $\text{CaWO}_4$  crystal. It has a resolution of  $60.7(4)$  keV (4.6 %) for the cobalt lines and a baseline of  $10.3(2)$  keV.

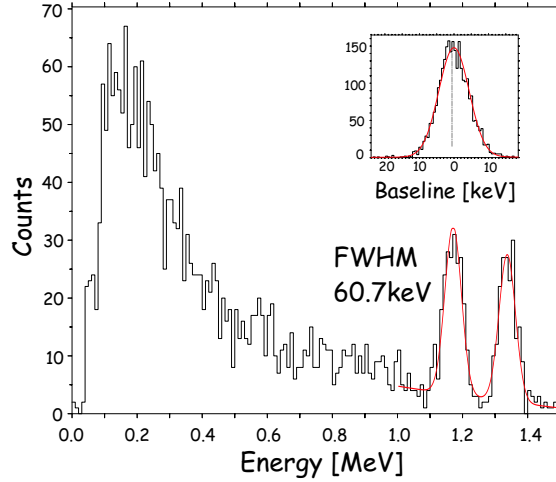


Figure 5.18:  $^{60}\text{Co}$  Spectrum recorded with a  $4\text{ cm} \times \varnothing 4\text{ cm}$   $\text{CaWO}_4$ . The insert shows the baseline noise in keV. The FWHM of the  $^{60}\text{Co}$  lines is  $60.7(4)$  keV, the FWHM of the baseline  $10.3(2)$  keV.

Figure 5.19 shows the  $^{60}\text{Co}$  spectrum recorded with the light detector while the source was still irradiating the  $\text{CaWO}_4$  crystal. The resolution of the lines is  $116(5)$  keV (10 %), while the baseline has a FWHM of  $24.9(2)$  keV. This resolution is comparable to the resolutions obtained with photomultipliers by other groups with crystals of similar type ( $\text{CdWO}_4$ ) and dimensions [Bur96, Kin94].

### 5.3.1 Coincident Measurements in Munich

Plotting the energy deposited in the  $\text{CaWO}_4$  (phonon channel) against the ratio of energy in the light channel and phonon channel<sup>9</sup> the events group in a horizontal band (see figure 5.20) that broadens towards lower energies. The measurements in Munich proved the feasibility of the holder concept. But as there was no shielding against radiation from the surrounding, the rates in the big  $\text{CaWO}_4$  crystal were

<sup>9</sup>The ratio for  $\gamma$ -interactions is normalized to 1.

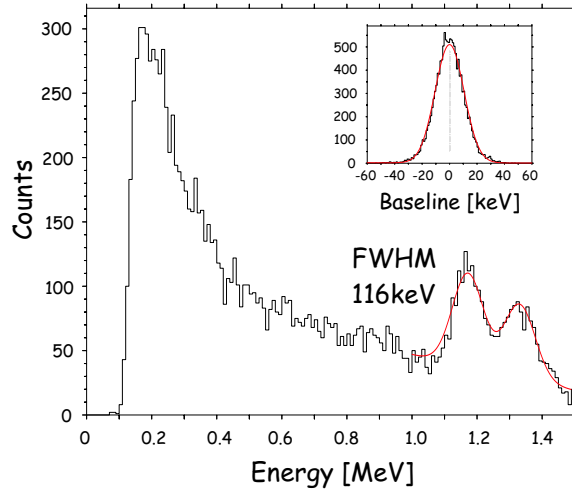


Figure 5.19: Scintillation light spectrum of a  $^{60}\text{Co}$  source shining on a  $4\text{ cm} \times \varnothing 4\text{ cm}$   $\text{CaWO}_4$  crystal, recorded with a  $2 \times 2\text{ cm}^2$  sapphire light detector. The insert shows the ‘pulse height’ of the baseline. The FWHM of the  $^{60}\text{Co}$  lines is  $116(5)\text{ keV}$ , the FWHM of the baseline  $24.9(2)\text{ keV}$ .

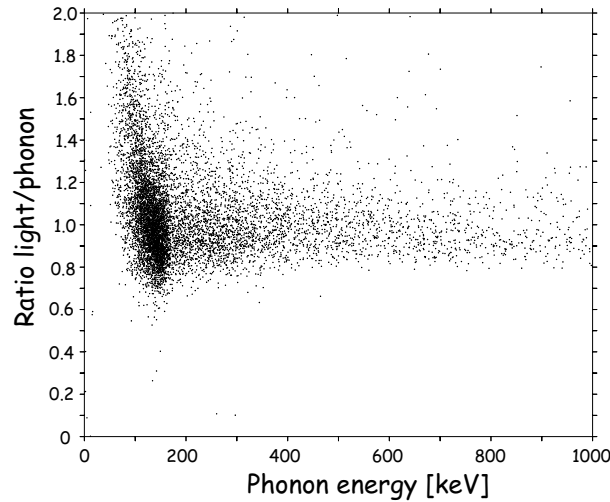


Figure 5.20: Energy in phonon channel versus ratio of light/phonon energy. The  $\text{CaWO}_4$  crystal was irradiated with a  $^{57}\text{Co}$  source.

very high. This led to significant pile up and very unstable detectors. To really determine the performance the setup has to be measured at the underground site at Gran Sasso.

### 5.3.2 Measurements at Gran Sasso

The first run of a complete detector module at Gran Sasso was done with the same  $\text{CaWO}_4$  crystal and light detector that was used for the above mentioned measurements. Unfortunately the light detector did show large oscillations of the baseline<sup>10</sup> and was useless below energies of several hundreds of keV. The phonon channel on the other hand showed almost linear response from 10 keV up to a few MeV. This large dynamic range is due to the high transition temperature of the thermometer film itself and the high Debye temperature of  $\text{CaWO}_4$ , which leads to a large heat capacity and a slow phonon velocity and thus energy flux into the thermometer. This dynamic range is not needed for a dark matter run but is very useful to identify contaminations in the crystal (see further down in this section).

The problem with such a large dynamic range is the calibration. The usual CRESST method is to use the 122 keV line from  $^{57}\text{Co}$  to calibrate the heater on the thermometer. After this one can use heater pulses of different (known) amplitudes to calibrate the entire range. To get a reliable calibration the pulse shape of the heater should be the same as for particles for all energies. Figure 5.21 compares a heater pulse of about 2 MeV and a particle pulse of the same energy. It is apparent that the heater shows a faster decay than the particle pulse but flattens out after that, and only decays very slowly from there. Apart from this difference in pulse shape that is present at all energies the relative amplitudes of the fast and the slow component of the pulse change with energy. The scatter plot 5.22 shows the fraction of the fast component in the particle pulses and the heater pulses. For the particle pulses the fraction stays constant, whereas for the heater pulses it is lower from the beginning and decreases towards higher energies. If one identifies the two components in the usual way as the heating up of the thermometer (fast component) and the entire detector (slow component), this means the high energetic heater pulses start to heat up the entire absorber more and more. This behaviour was already observed in the past [Mei99]. It was interpreted as a temperature dependent coupling of the heater to the substrate. At the high injected energies the heater and the contact area to the absorber heat above the temperature of the rest of the detector. The electron-phonon coupling in this point increases the coupling of absorber and heater and the heater injects a larger fraction of the phonons into the absorber. This causes the observed still

---

<sup>10</sup>These oscillations seemed to originate from mechanical vibrations of the long bond wires needed for the electrical connection of the thermometer.

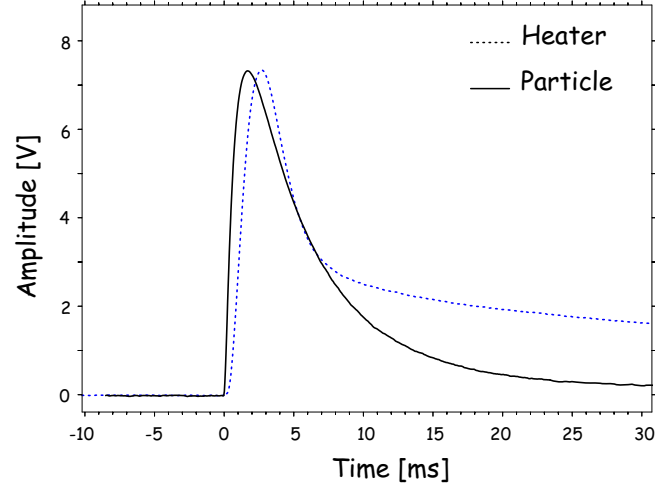


Figure 5.21: Particle and heater pulse of the phonon channel.

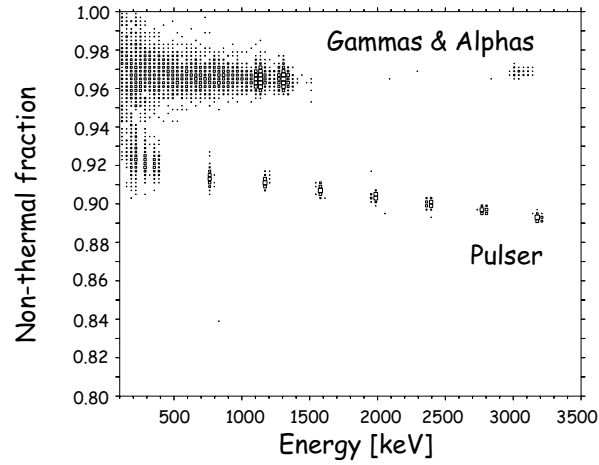


Figure 5.22: Fraction of the fast component in the signals of the particle and heater pulses of the phonon channel.

relatively moderate change of the response of the detector. Depending on what parts of the detector heat up, the measured temperature signal can be different for the same injected total energy. The calibration at high energies therefore gets unreliable. Figure 5.23 illustrates the almost constant difference of the decay

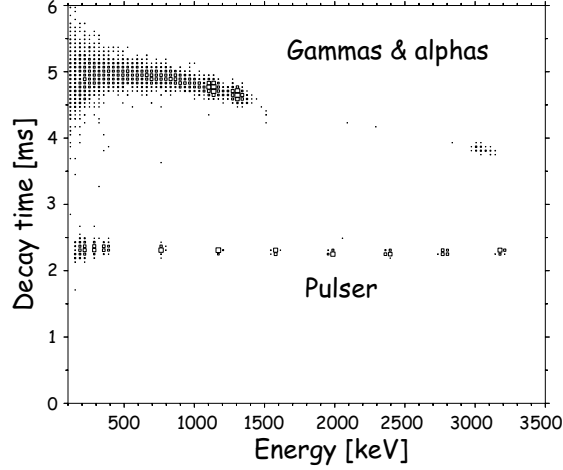


Figure 5.23: Decay time of the fast component in the pulses.

times of the fast components of the pulses. Towards higher energies the particle pulses get a bit faster. The low energy heater pulses are more than a factor of 2 faster than the particle pulses.

The  $5\sigma$  baseline noise of the phonon channel of this detector was 11.93(12) keV. The baseline noise of the light channel could not be determined due to the oscillation on the baseline.

The second run with a full module at Gran Sasso was done with a different  $\text{CaWO}_4$  crystal and light detector. The  $\text{CaWO}_4$  did not reach the sensitivity of the previous run. The light detector was replaced by a  $3 \times 3 \text{ cm}^2$  silicon light detector with a standard CRESST thermometer. Figure 5.24 shows the light and heater pulses in this light detector. Here the pulse shapes agree very well over the entire energy range. The insert shows the baseline of the light detector in keV normalized to  $\gamma$  interactions in the  $\text{CaWO}_4$  absorber. The  $5\sigma$  baseline noise for this light detector in conjunction with this  $\text{CaWO}_4$  was 10.2(4) keV. This is consistent with the pulser resolution of 4.9 keV<sup>11</sup>.

Although the signal quality in the phonon channel was not excellent some background data was taken to identify possible sources of contamination. Figure 5.25

<sup>11</sup>As there is no separate calibration for the light detector the resolution and baseline can not be given in absolute energy on the light detector, but in the corresponding energy for a electron recoil in the  $\text{CaWO}_4$ .

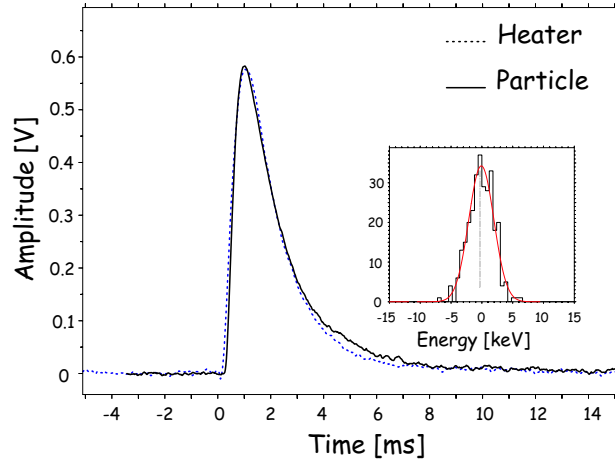


Figure 5.24: Particle and heater pulse in the light detector.

shows the energy measured in the phonon channel versus the ratio of the light and phonon energy. Apart from the  $\gamma$ 's at a ratio of 1 an  $\alpha$  population at an energy of  $\approx 2.6$  MeV and ratio of 0.178(2) (quenching  $\approx 5.6$ ) can be identified. The count rate was  $\approx 16$  counts/h in the 2.6 MeV  $\alpha$  peak and slightly below 10

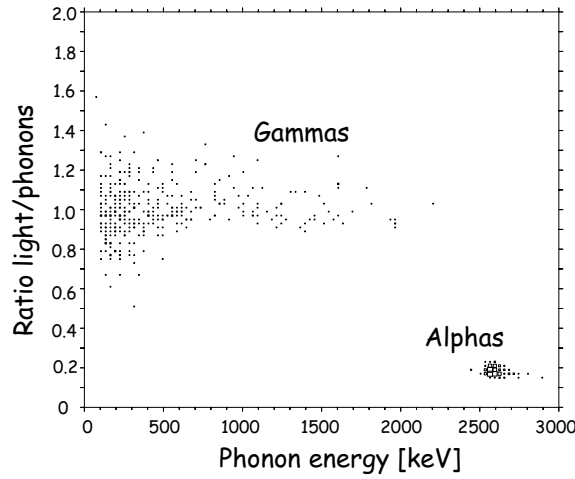


Figure 5.25: Ratio of light to phonon energy versus energy in phonon channel.

counts/kg/keV/day of background around 10 keV. This is still about a factor of 10 higher than proposed for CRESST-II. The exact origin of this contamination has yet to be clarified.

Another interesting fact is the different pulse shape observed in the light detector depending on the type of interaction in the  $\text{CaWO}_4$ . In figure 5.26 the quality of

the template fit is plotted versus the energy. The events group in three bands.

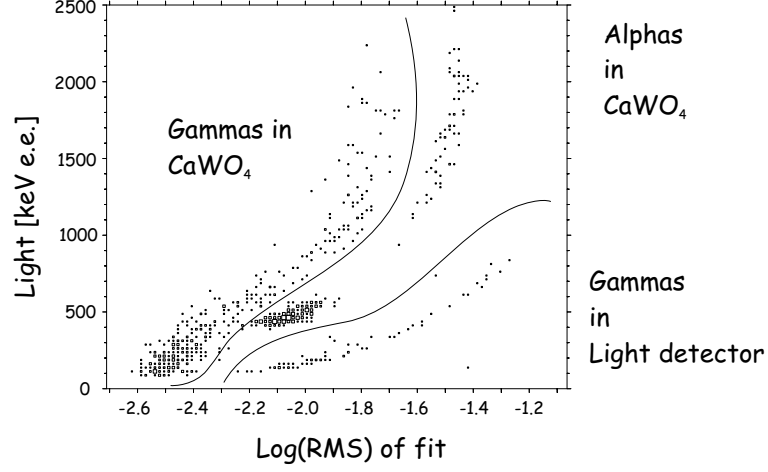


Figure 5.26: Goodness of template fit versus energy in the light channel.

The pulses for the template were chosen from pulses that were caused by  $\gamma$  interactions in the CaWO<sub>4</sub>. Trivially these events give the best fit and form the first band. The second band close by is due to the  $\alpha$ 's in the CaWO<sub>4</sub>. These have a slightly slower rise and decay time than the  $\gamma$  events. This is due to a slower emission of the scintillation photons after an  $\alpha$  interaction. At room temperature this effect is commonly used to identify the interaction in a scintillator. At mK temperatures these differences are slowed down enough to be measurable with our detectors. The third (well separated) band are no-scintillation light events but direct interactions in the light detector. Their time structure is much faster and they can be clearly separated with this technique.

# Chapter 6

## Simulation

### 6.1 Detector Simulation & Possible Performance

For future developments it is very important to know which parts of the detector contribute in which way to the overall performance. With this knowledge one can quantify the possible gain of improvements and thus concentrate on crucial parts. For this purpose two Monte Carlo simulation programs have been written to simulate the scintillation module. The first program traces the scintillation photons of an event in the  $\text{CaWO}_4$  crystal until they get absorbed in the light detector or any other part of the holder. All photons that are absorbed in the light detector result in the measured light signal. After calibrating this simulation with existing data, the probability for a single scintillation photon to be absorbed in the light detector can be calculated. Usually this is not a number but a distribution that reflects spatial dependencies, trapped light effects and parasitic absorptions in the holder. With this distribution a second program calculates a phonon versus light discrimination plot for electronic and nuclear recoils. From this plot one can derive the threshold down to which a separation of electronic and nuclear recoils is possible.

#### 6.1.1 Geometry

The raytracing program simulates the actual geometry with all material properties. Figure 6.1 shows the dimensions of the setup in the program. Basically it consists of a cylindrical  $\text{CaWO}_4$  crystal with a cylindrical reflector around. The reflector is mainly specularly reflecting. Teflon parts in the real module are represented by diffuse reflecting areas. A light detector of variable size is placed at one end of the reflector. The four Teflon tongues holding it are modelled by diffuse reflecting rectangles. The Teflon ramps that fix the  $\text{CaWO}_4$  crystal are



approximated by a partial diffuse reflection of photons crossing the hatched area in figure 6.1.

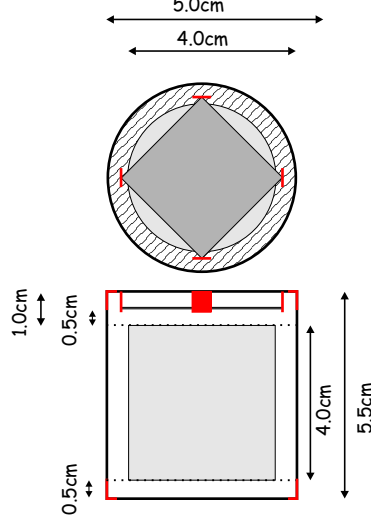


Figure 6.1: Sketch of simulated geometry.

For the actual simulation a random position in the  $\text{CaWO}_4$  crystal is generated. According to the energy of the event a number of photons is launched in  $4\pi$ . Their trajectories are calculated taking different materials and properties into account. All photons from one event that end up in the light detector are added up and “detected”. The light detector is characterized by an energy threshold plus a linear dependence of the resolution with energy, and a loss term. The loss term defines how much of the energy of a photon is lost, depending on the spot where it hits the absorber<sup>1</sup>. The resolution of the detector for low energies is dominated by the threshold, whereas for higher energy depositions it approaches the limit given by the linear dependence, which was found for practical detectors [Sis01].

### 6.1.2 Parameters

Most of the parameters that enter into the simulation were measured in independent experiments or could be taken from the literature. Only the light yield and the absorption length of the  $\text{CaWO}_4$  crystal were determined by fitting the simulated spectra to a measured one.

The transparency of the  $\text{CaWO}_4$  crystal was measured with a spectrometer (figure 6.2). This number is a combination of scattering ( $l_{sc}$ ) and absorption ( $l_{abs}$ ) in the

<sup>1</sup>For the lack of an accurate knowledge of the ‘loss-function’, losses are assumed to be linear in distance.

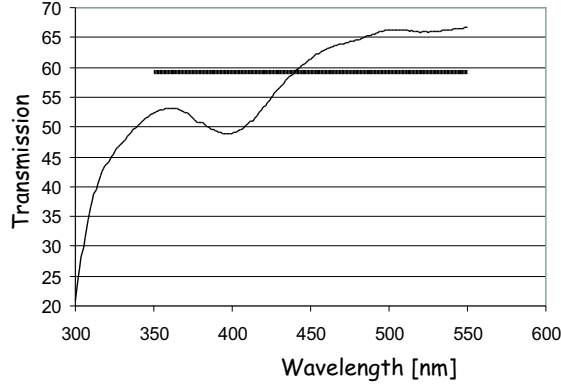


Figure 6.2: Measured transparency of a 4 cm  $\text{CaWO}_4$  crystal. As an average 59.0 % of the light was detected. The losses are due to reflections at the material boundaries (10.0 % for each transition), elastic (scattering) and inelastic interactions (absorption) in the crystal. A free path (scattering+absorption) for photons with 350–550 nm of 17.9 cm can be calculated for this crystal.

crystal. Fixing one of the two thus determines the other. The line resolution of the simulated spectra depends sensitively on the ratio of  $l_{sc}$  and  $l_{abs}$ . If the absorption dominates, spatial dependencies in the crystal (due to trapped light effects) are enhanced and result in a bad resolution in the light detector. In a scatter dominated crystal, (almost) no trapped light effects occur. Figure 6.3 shows a simulated and a measured spectrum. The resolution and the peak height

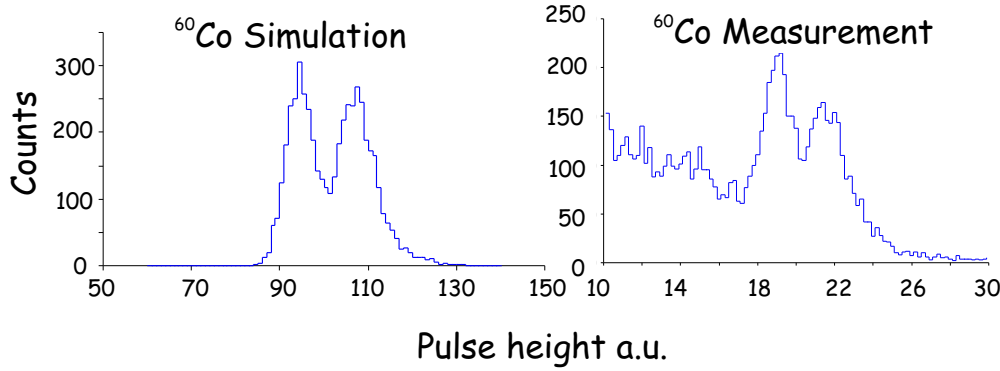


Figure 6.3: Simulated and measured  $^{60}\text{Co}$  spectrum. The background visible on the real spectrum is due to Compton scattering. This was not simulated.

ratio of the simulation match the measured spectrum. The Compton background that is visible on the real spectrum was not simulated.

The light yield on the other hand mainly affects the absolute energy that is detected in the light detector. Fitting the peak position to the experiments (table

5.1) gave a light yield of 3.5 % for a good crystal at mK temperatures. This is about 30 % of the value for NaI(Tl) at room temperature. Other authors ([Bea60]) found a value of 10 % (room temperature) for “cloudy” crystals. In our setup  $\text{CaWO}_4$  crystals with a slight whitish appearance gave a factor two less light (15 % of NaI(Tl)). Together with the 1.5 fold increase of light yield at 4 K [Kee01] the numbers are compatible.

The reflectivity of the reflector is a combination of the reflectivity of the multilayer foil (99 %) and gaps (1 cm<sup>2</sup>, 100 % absorption) in the reflector needed for the feedthrough of the electrical connections. The total area of all gaps sums up to about 1 cm<sup>2</sup>. This is about 0.8 % of their inner surface of the detector holder. This results in a total reflectivity of 98 % for the reflector.

In table 6.1.2 all parameters used for the simulation are compiled.

parameter	value	source
<b>Holder:</b>		
dimensions		technical drawing
reflectivity of foil	99 % (above 390 nm) 25 % (below 390 nm)	measured, [Web00]
reflectivity of reflector	98 % (above 390 nm)	calculation
<b><math>\text{CaWO}_4</math>:</b>		
size	h: 4 cm $\varnothing$ : 4 cm	
free path for light in $\text{CaWO}_4$	$l_{\text{free}} = 17.9$ cm	measured (figure 6.2)
absorption length in $\text{CaWO}_4$	$l_{\text{abs}} = 250$ cm	fit to data
scatter length in $\text{CaWO}_4$	$l_{\text{scatter}} = 19.3$ cm	$l_{\text{scatter}}^{-1} = l_{\text{free}}^{-1} - l_{\text{abs}}^{-1}$
emission peak of scintillation	425 nm (FWHM 90 nm)	[Kee01]
refraction index	1.93	[Gil49]
light yield	3.5 %	fit to data
quenching	7.4 for nuclear recoils	measurement [Meu99]
threshold	$\sigma = 1$ keV	measurement [Sta01]
<b>Light detector:</b>		
size	$3 \times 3$ cm <sup>2</sup> silicon waver	
resolution	$\delta E/E = 0.05$	measurement (see 5.2)
threshold/baseline	$\sigma = 10$ eV	measurement (see 5.2)
absorption	silicon: 60 % sapphire: 55 %	measurement (4.1.3)
energy loss in substrate	silicon: 12 % per cm sapphire: 10 % per cm	measurement (see 5.2)

Table 6.1: Parameters used for the simulation.

### 6.1.3 Results

The parameters given in table 6.1.2 will from now on be the standard parameters for the setup with this specific  $\text{CaWO}_4$  crystal. To directly see the effects of changes of various parameters, ‘probability’ spectra were made. They show the probability of an individual photon that is generated in the  $\text{CaWO}_4$  to be absorbed in the light detector. In a perfect setup this probability would be independent of the position where the photon was emitted, and the probability would be a simple number. In reality however, the probability depends on the position. This leads to a certain distribution in these plots. Figure 6.4 shows the calculated probability distribution for the standard parameters. Roughly 41 % of all photons are detected in the light detector. The width of the peak in this distribution reflects the spatial dependence in the crystal. In a perfect cylindrical  $\text{CaWO}_4$  crystal with no absorption and no scattering a significant fraction of the scintillation light would undergo total reflection on the surface and be trapped in the crystal. For photons generated on the axes of the cylinder this fraction would be 37 %, for photons close to the cylindrical wall 75 %. In real crystals scattering

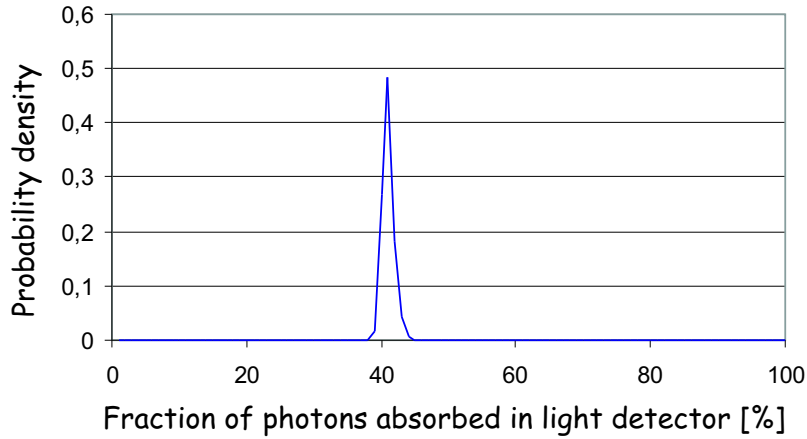


Figure 6.4: Probability of an individual photon to be absorbed in the light detector. Calculated with the standard parameters. The mean value is 41 %. The width of the peak is due to the spatial dependencies in cylindrical crystals.

and absorption compete. When the scattering dominates trapped photons can change their direction and get out before they are absorbed. In figure 6.5 this effect is clearly visible. A stronger absorption in the crystals leads to less light output and a stronger spatial dependence.

Another important part of the holder is the reflector. Photons that get out of the crystal must efficiently be collected in the light detector. As it was mentioned before (section 3.3) the photons can not be focused onto the detector. One has to rely on a good reflector that efficiently reflects the photons around until they

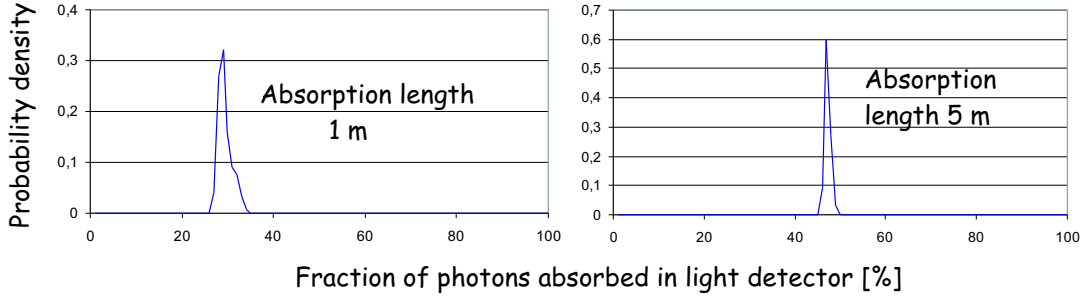


Figure 6.5:  $\text{CaWO}_4$  crystals with 1 & 5 m absorption length. The scattering length was adjusted accordingly to keep the free path  $l_{free} = 17.9$  cm constant.

finally get absorbed in the light detector. Figure 6.6 compares two reflectors of

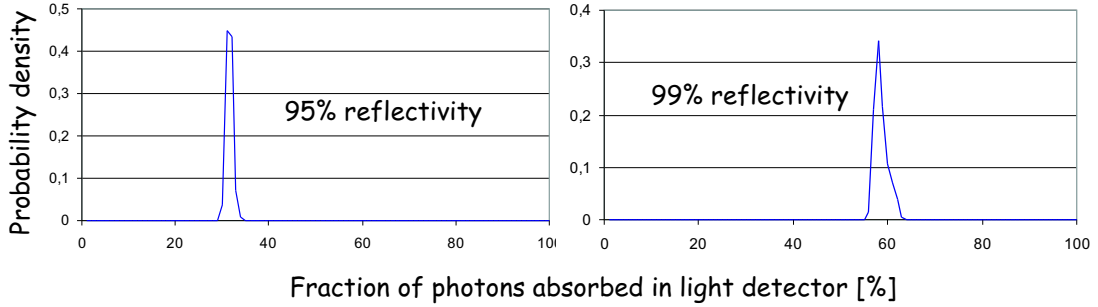


Figure 6.6: Comparison of reflectors with 95 % and 99 % reflectivity. The bandwidth is 390–550 nm in the first case and 300–550 nm in the latter.

different quality. The first one reflects with 95 % in a range of 390–550 nm, the second covers the entire emission peak of  $\text{CaWO}_4$  (300–550 nm) with 99 %. The gain is almost a factor of 2. The maximum fraction of the light that can be collected is again governed by the absorption in the  $\text{CaWO}_4$ . Photons that got out of the crystal initially do not get trapped again but can get absorbed during the process of being reflected around in the holder. In the case of the 99 % reflector more than two thirds of the photons that are not detected in the light detector got absorbed in the crystal.

The area of the light detector is a parameter that has a significant influence on the performance. The larger the detectors the more light they absorb<sup>2</sup>. On the other hand phonon losses in the substrates get more pronounced in large area detectors. As long as only a small fraction of the total light is detected the

<sup>2</sup>A larger light detector means a photon has to be reflected fewer times before it hits the detector and gets absorbed. Therefore it has a smaller probability of getting absorbed in the crystal or the reflector.

absorbed energy almost scales linearly with the surface area of the light detector. When the absorbed fraction of the scintillation light increases, the gain-per-area starts to decrease. Above a certain size a further increase in area will then lead to a decreasing overall sensitivity due to phonon losses and/or reduced sensitivity in the light detector.

Simulations and experiments have shown that the maximum size ( $3 \times 3 \text{ cm}^2$  for square substrates) that can be fit into the holder give the best performance. They absorb the maximum amount of light without suffering already from significant losses. The absolute maximum size that can be fit into the existing design would be a round substrate with 5 cm diameter. It would fully cover one end of the holder. It has 2.2 times the size of the aforementioned detector, but simulations revealed that it only absorbs 10 % more photons. The performance in terms of discrimination between  $\gamma$ 's and nuclear recoils (see next section) was not improved at all. This has several reasons. The square shaped detectors are held in a way that both sides are exposed (figure 3.7). About 30 % of all absorbed photons hit the  $3 \times 3$  detector from the backside. In the case of a round full size detector only one side is active. This means the gain in effective area is smaller than the gain of total surface. Secondly loss processes in the substrates get more severe in big light detectors. In total the detected energy does not increase with a full size detector in comparison to a  $3 \times 3$  detector.

#### 6.1.4 Performance

The above results can be used to simulate the low energy regime around the threshold, to determine down to which energy one can discriminate between electronic and nuclear recoils. Nuclear recoils give less light per deposited energy. The ratio  $E_{\text{light}}/E_{\text{phonon}}$  thus identifies the interaction. Plotting this ratio versus  $E_{\text{phonon}}$  results in a scatter plot like figure 6.7. The two types of interactions form two horizontal bands. Because of the limited resolution of the detectors and the statistics of the absorbed photons the two bands merge towards small energies. This energy defines the discrimination threshold.

In a more quantitative picture one limits the fraction that may leak into the other band, for example to 0.3 %. Down to the energy where this limit is reached a discrimination of 99.7 % or better is achieved. Figure 6.8 shows a discrimination plot that was calculated using the parameters of the previous section. In this picture not every individual simulated event is marked but lines that indicate the boundaries of the bands. The light grey lines represent the  $2\sigma$  level. Between the upper pair of grey lines there are 95.4 % of the electron recoil events, under the lower grey line there are 95.4 % of the nuclear recoil events. The dashed black lines indicate the average value of all events in the band. The dark grey lines show the level where 99.7 % of the events are above (electron recoil band) or below (nuclear

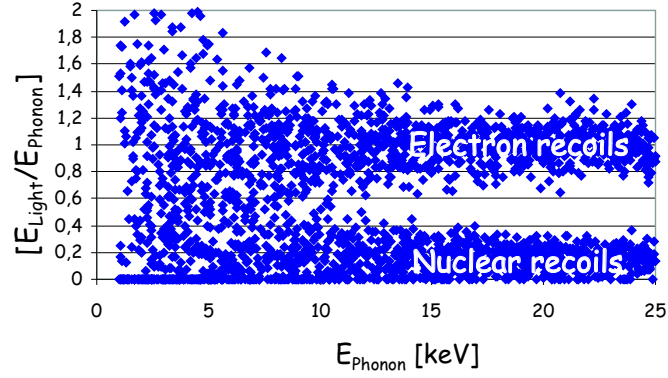


Figure 6.7: Scatter plot of electronic and nuclear recoils. The events group in two bands for nuclear recoils and gammas. The y-axis is normalized to  $\gamma$  interactions.

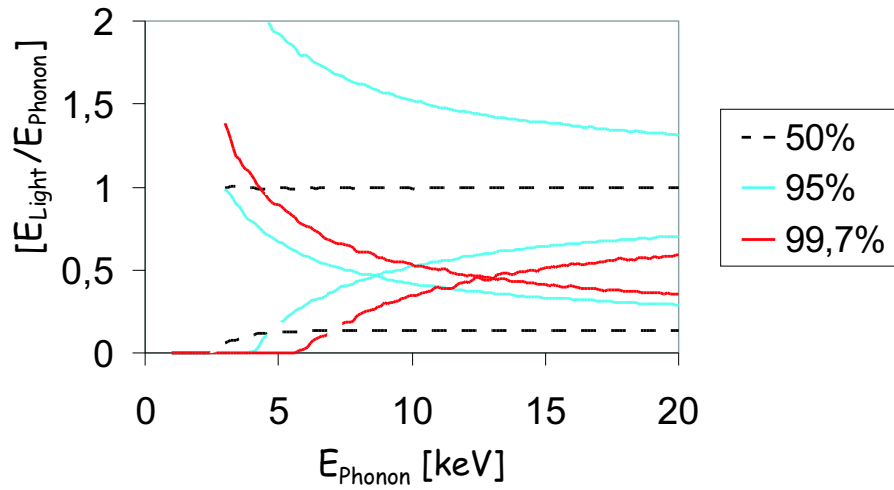


Figure 6.8: Simulated discrimination plot for “real” detector. The discrimination threshold is  $\approx 13$  keV. The dark grey lines indicate the 99.7 % level. Their crossing defines the threshold of the module.

recoil band). Down to the energy where they cross a discrimination of 99.7% or better is possible. This intersection is roughly at 13 keV. This performance is already better than proposed in [pro01]. Measurements with the prototype detector have yet to confirm these simulations.

Although the required discrimination can be achieved with the present setup improvements can and should be made. By calculating discrimination plots for the different parameters one can estimate the influence and potential gain of changes. The width of the bands is mainly given by the resolution of the light detector and the statistics of the absorbed photons. The threshold and resolution at low energies are dominated by the baseline noise of the detector. Decreasing the threshold of the light detector will thus separate the two bands better and lead to a better discrimination. Figure 6.9 used the same parameters as before but a light detector with a factor two lower threshold. A discrimination is now possible down to 10 keV.

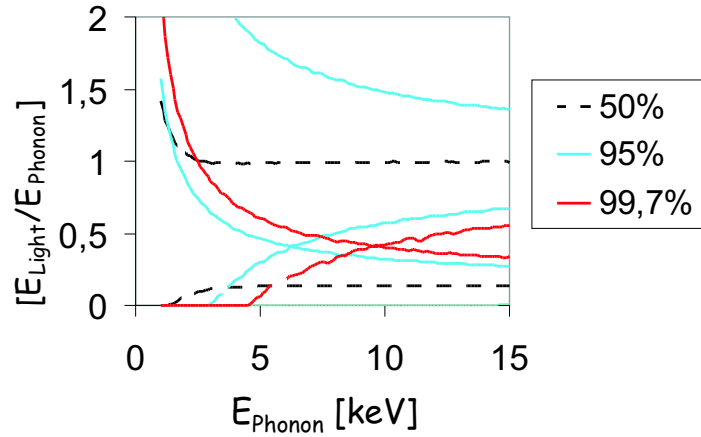


Figure 6.9: Discrimination plot calculated with a light detector threshold of 25 eV ( $5\sigma$ ). A discrimination of 99.7 % is now possible down to 10 keV.

The photon statistics can be improved by collecting more photons<sup>3</sup>. Assuming that the scintillation yield for a given crystal type is constant the maximum number of photons that can be detected is determined by the absorption in the crystal (absorption length) and the reflector (reflectivity). In the present setup 23% of the initially created photons are absorbed in the crystal, 35% in the reflector. The remaining 41% end up in the light detector. This means that more than half of the scintillation light is lost in the collection process. At the moment the crystal quality can only be influenced by choosing the best crystals of a

<sup>3</sup>At the same time this will increase the total energy of the detected light and thereby decrease the discrimination threshold



batch. This can be done with transmission measurements in a spectrometer, an integrating sphere or with a photomultiplier setup to directly see the light output of the tested crystals<sup>4</sup>. Changing the absorption length in the crystal has a large impact on the discrimination threshold. Assuming 1 m absorption length instead of 2.5 m moves the 99.7 % point to 17 keV.

One third of the created photons are lost in the reflector. Part of it is due to the cutoff of the used foil at 390 nm. About 10 % of the scintillation light photons have a shorter wavelength. A new foil with a wider range is currently under development at 3M. Reducing the gaps for the feedthrough of the electrical con-

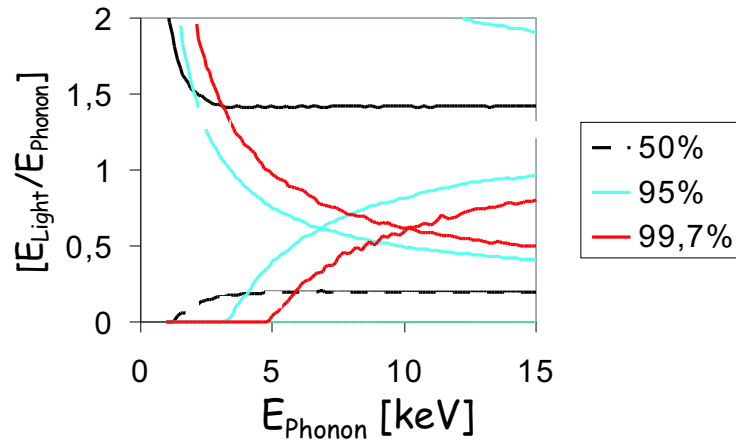


Figure 6.10: Setup with wide band reflector foil and 99 % total reflectivity of reflector.

nections one can reach a reflectivity of 99 % for the entire scintillation light peak. Figure 6.10 shows the performance that can be expected with such a reflector. The detected light energy goes up by about 40 %. This leads to a better separation of the two bands and a better photon statistics and thus improves the discrimination threshold to  $\approx 10$  keV as compared to  $\approx 13$  keV with the standard reflector (figure 6.8).

As mentioned before the size of the light detector substrates has an influence on the amount of collected light. For large light detectors this gain is counterbalanced by the phonon losses in the substrates.  $3 \times 3 \text{ cm}^2$  substrates gave the best results. Alternatively simulated setups with light detectors that covered the entire end of the holder, absorbed more light but did not improve the threshold of the module. New substrates (e.g. thicker) that reduce phonon losses could change

<sup>4</sup>A combination of the methods can answer the question if the initially created number of photons (Photons/MeV) is constant or varies between the crystals or even shows a spatial dependence in a single crystal.

this situation in favour of bigger light detectors. For detectors larger than the endcap, mounting and assembling could be simplified as well.

### 6.1.5 Conclusions

With a simulation it is possible to combine the results of different independent measurements and determine unknown parameters (light yield, absorption length). This knowledge is important for future optimization. One fact that is not yet included in the simulation is the quenching factor for different nuclei of  $\text{CaWO}_4$ . The quenching factor used here was measured with a neutron source. For neutrons the main contribution comes from recoils on oxygen, whereas WIMPs mainly scatter on the heavy tungsten nuclei. These recoils may produce less light<sup>5</sup>. A neutron experiment to measure these (different) quenching factors is currently under construction at the TUM [Jag]. Once known they should be included in the simulation, as they might have some effect on the no-light events.

The threshold of the light detector is one of the main factors that determines down to which energy a discrimination is possible. A 50 eV ( $5\sigma$ ) threshold is sufficient to reach the planned discrimination, but a lower threshold may be desired with respect to no light events. The left graph in figure 6.11 shows the expected fraction of events for which no light above 50 eV can be measured. At 15 keV almost 10 %

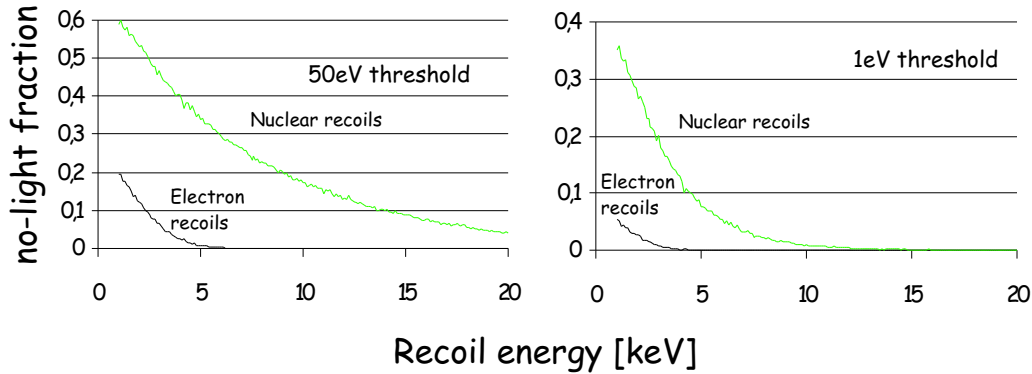


Figure 6.11: The plots show the expected fraction of events that have no co-incident light signal, for electron recoils and nuclear recoils. The first plot was calculated with a threshold of 50 eV, the other one with 1 eV (single photon efficiency).

of the nuclear recoils (possible WIMP signal) show no light. At 5 keV (the  $5\sigma$  threshold of the phonon detector) this fraction goes up to one third. For the real

<sup>5</sup>The heavy tungsten nuclei move slower than oxygen with the same energy and therefore may lead to a less effective light production.

dark matter runs it would be desirable to always have a coincidence between the two detectors. Real events can then be distinguished from spurious events by the proper ratio of phonons to light. The graph on the right hand side shows the same setup with a “perfect” light detector with single photon sensitivity. Still some 8 % of the recoils at 5 keV show no light signal, simply because not a single photon got absorbed in the light detector. This emphasizes the necessity of a good light collection.

A good light collection requires a good reflector and a good crystal. Measurements have shown up to a factor of two difference in the light output of different crystals. For the future this means the parameters that decide the crystal quality during the production process have to be found out and controlled accordingly.

The threshold of the phonon detector is secondary for the discrimination of electron and nuclear recoils, but crucial for the discrimination of real and fake events. For a low energetic signal in the phonon channel that is not accompanied by a light signal, the shape is the only information available. Fake events due to electrical interference or vibrations are not expected to have the same well defined shape as real signals. The smaller the noise (threshold) of a measured signal the better the shape information can be extracted.

Figure 6.12 shows the projected performance of a setup with optimized reflector and light detector. A discrimination threshold of 9 keV seems possible. The assumed parameters for reflector, crystal and light detector <sup>6</sup> have already been attained for individual components.

In Figure 6.13 the influence of the photon statistics and light detector threshold and resolution are shown. The plot on the left side was calculated with the same parameters as figure 6.12, but with no photon statistics. The threshold improves to 6.6 keV. In the other plot the light detector threshold and resolution were set to ‘0’ eV. This only improves the threshold to 7.6 keV. This means with a light detector with 30 eV threshold and 1.8 % (for  $\gamma$ ’s) of the total energy detected in the light channel, the main contribution to the discrimination threshold comes from the statistics of the detected photons and the remnant spatial dependence in the  $\text{CaWO}_4$  crystal. This emphasizes the necessity of high quality crystals with a high light output.

Overall the results of the simulations should be reconfirmed and fine tuned by future measurements. Especially new quenching factors for recoils on different nuclei can change the amount of no-light events. This is particularly interesting as the tungsten recoils are expected to yield the smallest amount of light. Therefore low energetic tungsten recoils would have the highest probability to have no accompanying light signal. On the other hand these recoils will contribute

---

<sup>6</sup>An even lower threshold of 23 eV was accomplished on a light detector design without heaters [Sch01].

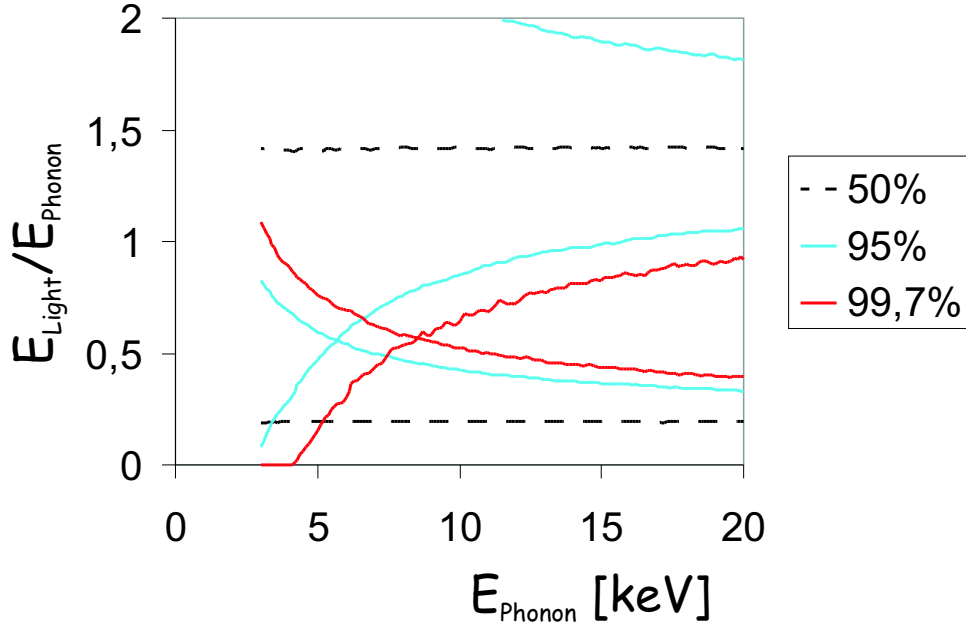


Figure 6.12: Performance achievable with a wide band (300 nm–600 nm, 99 % reflectivity) reflector and a 30 eV light threshold. A discrimination of 99.7 % is possible down to  $\approx 8.7$  keV.

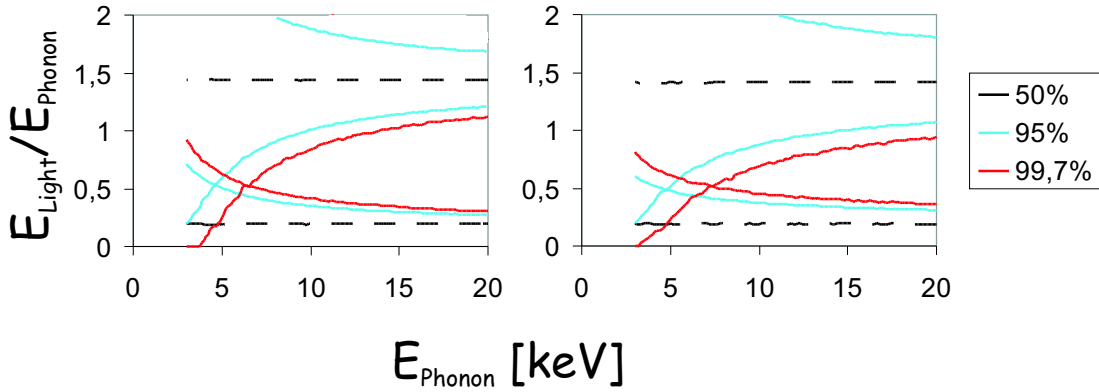


Figure 6.13: Discrimination plots calculated with the same parameters as figure 6.12, but without photon statistics (left plot) and with '0'eV threshold on the light detector. Without photon statistics the discrimination threshold is as low as 6.6 keV. With a perfect light detector it is at 7.6 keV.

the largest cross section for a possible coherent WIMP signal. A thorough understanding of the expected no-light events may be a statistical tool to verify a measured spectrum. A too large number of no-light events can mean that not only real events, but also disturbances ended up in the spectrum.

# Chapter 7

## Conclusions & Perspectives

### 7.1 Status

The main goal of this work was to develop a 300 g scintillating detector module that allows a 99.7 % rejection of  $\gamma$  and  $\beta$  background above a threshold of 15 keV. For this purpose a setup was developed that allowed an efficient collection of the scintillation light. With a  $3 \times 3 \text{ cm}^2$  silicon light detector a fraction of 1.3 % of the deposited energy in the  $\text{CaWO}_4$  scintillator could be detected. This is more than in the 6 g proof-of-principle experiment (0.8 %).

A first detector with a 300 g  $\text{CaWO}_4$  absorber was built. Despite its high transition temperature, the phonon channel showed a  $5\sigma$  threshold of 11.9 keV when run at Gran Sasso. This would already suffice to reach the projected threshold of the module.

At the same time a new concept for the thermometers on the light detectors, with phonon collectors and a designable thermal coupling, was developed. The variable thermal coupling allows to make small and sensitive thermometers with long decay times to integrate the incoming scintillation light flux. With a  $1 \times 1.5 \text{ mm}^2$  thermometer a  $5\sigma$  threshold of 30 eV could be shown. Different materials for the substrates and absorption layers were tested. Silicon and sapphire based light detectors had an almost similar performance. For application in a setup with 33 modules in total the silicon substrates may be more convenient, because they do not need the extra processing steps for the absorption layer.

Simulations of the detector module were made to evaluate the possible discrimination threshold of the full setup. Using the parameters already demonstrated for the light detector, phonon detector and holder, a 99.7 % discrimination threshold of 13 keV was inferred. This fulfils the projected sensitivity of 99.7 % down to 15 keV. The recent developments on the light detector side and a new mirror foil that will be soon available, would lower the threshold to 9 keV. Additionally to

determining the possible performance the simulation can be used to improve the detector module, as the effect of changes of different parts of the module can be investigated. In the CRESST-II experiment the exact understanding of the expected detector response to different types of interactions will be crucial to rule out any disturbances and fake events in the setup.

Three runs in the setup at Gran Sasso have been made until now. Due to technical reasons and/or a high internal background of the crystals no 'dark matter data' has been taken yet. The background is currently under investigation. In the first two runs an  $\alpha$  contamination at  $\approx 2.6$  MeV was found. The  $\gamma$  background at low energies was roughly 10 counts/kg/keV/day. The third run was done with a crystal from a different supplier that showed a very high  $\gamma$  and  $\beta$  activity of 0.3 Hz. The origin of this background has been identified to be  $^{210}\text{Pb}$  [Coz02b], presumably from  $\text{PbWO}_4$  crystals grown in the same crucible before.

## 7.2 Next Steps

The most urgent next step is the identification of the  $\alpha$  background in the detectors. The steps in the manufacturing process of the crystals or the detectors that cause this contamination have to be found out. Until now the crystal growth process is not controlled and crystals from different suppliers have vastly different contamination sources and levels.

In order to use the new thermometer design for the next generation of light detectors, the geometry (thickness, width/length ratio) should be altered to match the  $50\text{ m}\Omega$  shunt resistors in the Gran Sasso cryostat. In past runs the long bond wires needed to contact the detectors were very susceptible to vibrations. To minimize this problem thin aluminium leads could be evaporated onto the substrate and thus considerably shorten the bond wires. The results in this work suggest a large contribution of excess noise in the thermometers that cannot be explained by the basic noise sources. A systematic study of the dependence of this excess noise on the substrate, readout current and film geometry could shed some light on this issue. If this were solved a single photon efficiency for the light detector seems feasible. For the light detectors different substrates (thicker) could be used to possibly minimize the phonon losses. Some 10 % of detected energy could be gained by this. If the sensitivity of the detector is not lowered by the higher heat capacity of the substrates the threshold should go down accordingly.

## 7.3 Future

For the immediate future it is planned to run two complete modules in the cryostat at Gran Sasso to get a full understanding of the detectors and the background, and possibly test electronic components for the new 10 kg setup. At the end of 2002 the upgrade of the cryostat from 4 to 66 SQUID channels is projected. At the beginning of 2003 the number of running modules will be increased step by step up to 33 modules in total.

The final sensitivity for a WIMP signal after three years of data taking with a full 10 kg detector is shown in plot 7.1. It is similar to the CDMS experiment at the new location in the Soudan mine. The dots mark the regime of possible WIMP-neutralino candidates [Bed98]. The sensitivity of CRESST phase II covers a significant part of the MSSM<sup>1</sup> parameter space. Interesting physics results can be expected within the next few years.

---

<sup>1</sup>Minimal Supersymmetric Standard Model



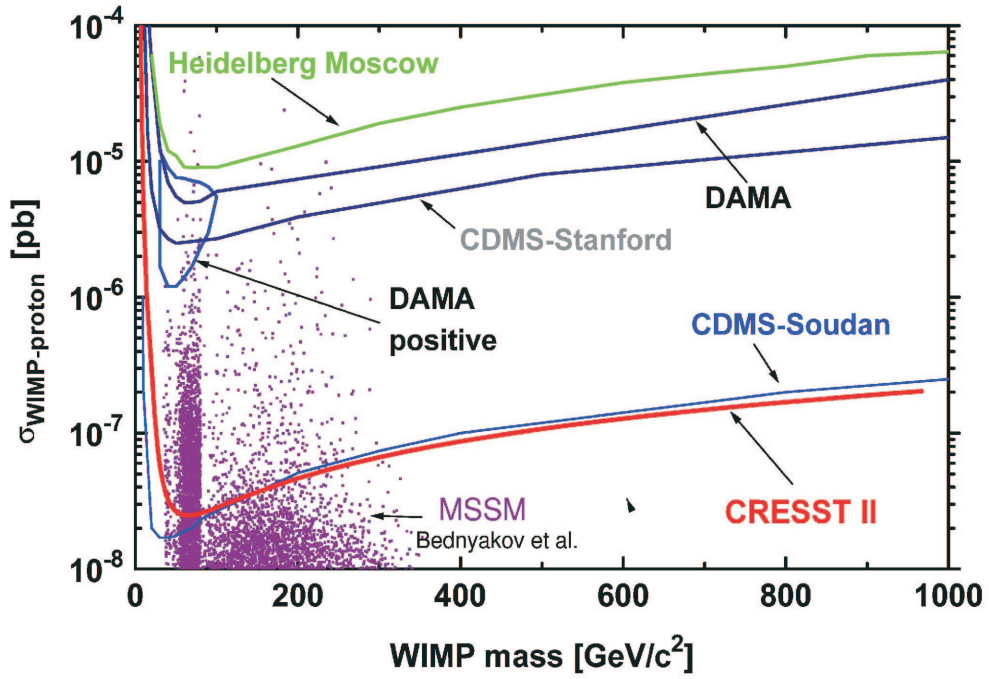


Figure 7.1: WIMP-nucleon cross section limits (90 % CL) for coherent interaction as a function of WIMP mass. The plot is based on a background level of 1 count/keV/day/kg, an intrinsic background rejection of 99.7 % above 15 keV and 30 kg years of data. For comparison the limit from the Heidelberg-Moscow  $^{67}\text{Ge}$  experiment [Bau98], the DAMA limits [Ber99] with the contour for positive evidence, the CDMS limit at the shallow underground cite in Stanford [Abu02] and the projection for CDMS in the Soudan mine [Sch99] is also shown. The scatter plot represents the expectations for WIMP-neutralinos calculated in the MSSM framework with non-universal scalar mass unification [Bed98]

# Bibliography

- [Abu02] R. Abusaidi et al., *Phys. Rev. Lett.* **84(25)** (2002) 5699–5703
- [Ahm02] Q.R. Ahmad et al., *nucl-ex/0204009 submitted to Phys. Rev. Lett.*
- [Alb82] A. Albrecht, P.J. Steinhardt, *Phys. Rev Lett.* **(48)** (1982) 1220
- [Alt01] M. Altmann et al., In *X International Symposium on Lepton and Photon Interactions at High Energies*, July 2001
- [And81] A.C. Anderson, editor, *Nonequilibrium Superconductivity, Phonons and Kapitza Boundaries*, Plenum Press, 1981
- [Ang01] G. Angloher, 2001, private communication
- [Ang02] G. Angloher et al., *Astropart. Phys.* **18** (2002) 43–55
- [Bah99] N. Bahcall et al., *SCIENCE* **(284)** (1999) 1481
- [Bar00] J.C. Barton, J.A. Edgington, *Nucl. Inst. Meth. A* **(443)** (2000) 277–286
- [Bau98] L. Baudis et al., *Phys. Rep.* **307** (1998) 301–308
- [Bea60] G.B.. Beard et al., *Nuclear Physics* **16** (1960) 591
- [Bea62] G.B. Beard et al., *J. of Appl. Phys.* **33** (1962) 144–147
- [Bed98] V. Bednyakov et al., *Z. Phys. A* **357** (1998) 339–347
- [Beg91] K.B. Begemann, A.H. Broeils, R.H. Sanders, *Mon. Not. R. Astr. Soc.* **249** (1991) 523
- [Bel50] E.H. Belcher, *Nature* **166** (1950) 742
- [Ben02] A. Benoit et al., Eprint: astro-ph/0206271
- [Ber85] H. Bernhardt, *Phys. Stat. Sol.* **91** (1985) 643

- [Ber99] R. Bernabei et al., *Phys. Lett. B* (**450**) (1999) 448–455
- [Ber00] L. Bergström, *Rep. Prog. Phys.* (**63**) (2000) 793–841
- [Bra98] M. Bravin et al., CRESST proposal, 1998
- [Buc00] C. Bucci, 2000, private communication
- [Bur96] S.Ph. Burachas et al., *Nucl. Inst. Meth. A* **369** (1996) 164–168
- [Cal88] D.O. Caldwell et al., *Phys. Rev. Lett.* (**61**) (1988) 510
- [Car96] R.G. Carlberg et al., *Astrophys. J.* **462** (1996) 32
- [Col92] P. Colling, Master’s thesis, Technische Universität München, 1992
- [Col95a] P. Colling, PhD thesis, Technische Universität München, 1995
- [Col95b] P. Colling et al., *Nucl. Inst. Meth. A* **354** (1995) 408
- [Coz02a] C. Cozzini, PhD thesis, Ludwig-Maximilians-Universität München, 2002, in preparation
- [Coz02b] C. Cozzini, private communication, 2002
- [dB01] P. de Bernardis et al., Eprint: astro-ph/0105296
- [Deb12] P. Debye, *Ann. Phys.* **39** (1912) 789
- [DiS02] P. DiStefano et al., A textured si calorimetric light detector, *to appear in J. Appl. Phys*
- [DiT92] J.F. DiTusa et al., *Phys. Rev. Lett.* **68** (1992) 1156
- [Dix60] W.R. Dixon, J.H. Aitken, Pulse shape discrimination and energy response of calcium tungstate crystals, *Nucl. Inst. Meth.* **9** (1960) 419–232
- [Don01] J. Dončev, 2001, private communication
- [Don04] J. Dončev, PhD thesis, Technische Universität München, 2004, in preparation
- [Dru86] Drukier et al., *Phys. Rev. D* (**33**) (1986) 3495
- [Eis76] W. Eisenmenger et al., *Appl. Phys.* **11** (1976) 307
- [Ell84] J. Ellis et al., *Nucl. Phys. B* (**238**) (1984) 453
- [Faz98] T. Fazzini et al., *Nucl. Inst. Meth. A* (**410**) (1998) 213–219

- [Fer96] P. Ferger, PhD thesis, Technische Universität München, 1996
- [Fig00] E. Figueroa et al., Optimal filter analysis of energy-dependent pulse shapes and its application to TES detectors, *Nucl. Inst. Meth. A* **444** (2000) 453–456
- [For93] G. Forster, PhD thesis, Technische Universität München, 1993
- [Fra93] M. Frank, PhD thesis, Technische Universität München, 1993
- [Fra02] T. Frank et al., In *LTD-9 conference proceedings*, Seite 501, 2002
- [Fuk98] Y. Fukuda et al., *Phys. Rev Lett.* (**82**) (1998) 2644
- [Gai] R.J. Gaitkell et al., *Nucl. Phys. B (Proc. Suppl.)* 51
- [Gal91] J.C. Gallop, *SQUIDS, the Josephson Effects and Superconducting Electronics*, 1991
- [GB99] J. Garcia-Bellido, *Casta-Papiernicka 1999, High-energy physics* Seiten 109–186, hep-ph/0004188
- [Ger02] G. Gerbier et al., *Neutrino 2002, to be published in Nucl. Phys. B Proc. Suppl*
- [Gil49] R.H. Gillette, *Review of Scientific Instruments* **21**(4) (1949) 294
- [GM88] L. Gonzalez-Mestres, D. Perret-Gallix, *Proceedings of LTD-2* Seite 518
- [Gut81] A.H. Guth, *Phys. Rev. D* (**23**) (1981) 347
- [Hag98] C. Hagmann et al., *Phys. Rev. Lett.* (**80**) (1998) 2043
- [Hah77] H.D. Hahlbohn, H. Lübbig, *SQUIDS and their Applications*, de Gruyter, 1977
- [Har79] J.P. Harrison, *J. of Low Temp. Phys.* **37** (1979) 467
- [Het98] P. Hettl, PhD thesis, Technische Universität München, 1998
- [Hie82] K. Hieber, N.M. Mayer, *Thin Solid Films* 90(43)
- [Höh98] J. Höhne, PhD thesis, Technische Universität München, 1998
- [Jaf01] A.H. Jaffe et al., *Phys. Rev. Lett.* (**86**) (2001) 3475–3479
- [Jag] T. Jagemann, PhD thesis, Technische Universität München, in preparation
- [Joc94] J. Jochum, PhD thesis, Technische Universität München, 1994

- [Kap76] S.B. Kaplan et al., *Phys. Rev. B* **14** (1976) 4854
- [Kee01] R. Keeling, PhD thesis, University of Oxford, 2001
- [Kin91] D.L. King et al., *Proc. 22<sup>nd</sup> IEEE Photovoltaic Specialists Conference* Seiten 303–308
- [Kin94] D.R. Kinloch et al., *IEEE Trans. Nucl.* **41(4)** (1994) 752–754
- [Kit88] Ch. Kittel, *Einführung in die Festkörperphysik*, Oldenbourg Verlag, 1988
- [Kli57] C.C. Klick, J.H. Schulman, *Solid state physics*, volume 5, Academic Press, 1957
- [Koc96] M. Koch, Master's thesis, Technische Universität München, 1996
- [Kop89] K. Kopitzki, *Einführung in die Festkörperphysik*, Teubner, 1989
- [Krö48] F.A. Kröger, *Some aspects of the luminescence of solids*, Elsevier Publishing Company, 1948
- [Kur82] M. Kurakado, *Nucl. Instr. Meth.* **196** (1982) 275
- [Lin82] A. Linde, *Phys. Lett. B* (**108**) (1982) 389
- [Lin01] M.A. Lindeman et al., In *LTD-9 conference proceedings*, Seite 203, 2001
- [Liu91] J. Liu, N. Giordano, *Phys. Rev. B* **43** (1991) 3928
- [Loi99] M. Loidl, PhD thesis, Ludwig-Maximilians-Universität München, 1999
- [Lou74] O.V. Lounasmaa, *Experimental principles and methods below 1 K*, Academic Press, 1974
- [Mar80] R.F. Markiewicz, *Phys. Rev. B* **21** (1980) 4674
- [Mar90] H.J. Maris, *Phys. Rev. B* **41** (1990) 9736
- [Mat82] J. Mather, *Appl. Optics* **21(6)** (1982) 1125
- [McC93] D. McCammon et al., *Nucl. Instrum. Methods A* **326** (1993) 157
- [McC01] D. McCammon et al., editors, *Low temperature detectors*, American Institute of Physics, 2001
- [Mei99] O.J. Meier, PhD thesis, Technische Universität München, 1999
- [Meu99] P. Meunier et al., *Appl. Phys. Lett.* **75(9)** (1999) 1335

- [Mir02] R. Mirzoyan, private communication, 2002
- [Mur98] H. Murayama et al., *Eur. Phys. J. C* **(3)** (1998) 264
- [Nag93] U. Nagel et al., *J. of Low Temp. Phys.* **93** (1993) 543
- [Nam98] S.W. Nam et al., *LTD  $\gamma$  proc.* **56** (1998) 217
- [Net02] C.B. Netterfield et al., *astro-ph/0104460*
- [Nüß99] T. Nüßle, Master's thesis, Technische Universität München, 1999
- [Oga96] I. Ogawa et al., *Phys. Rev. D* **(53)** (1996) 1740
- [Oli97] K.A. Olive, D. Thomas, *Astropart. Phys* **(7)** (1997) 27
- [Pec77] R. Peccei, H.R. Quinn, *Phys. Rev. Lett.* **(38)** (1977) 1440
- [Pet02] F. Petricca, 2002, private communication
- [Pet04] F. Petricca, PhD thesis, Technische Universität München, 2004, in preparation
- [Pin93] E. Pinnotti et al., *Nucl. Inst. Meth. A* **326** (1993) 85
- [Pip55] A.B. Pippard, *Phil. Mag.* **46** (1955) 1104
- [Pob92] F. Pobell, *Matter and Methods at Low Temperatures*, Springer, 1992
- [Prö95] F. Pröbst et al., *J. of Low Temp. Phys.* **100** (1995) 69
- [pro00] Proposal to the gran sasso laboratory for a second phase of the cress dark matter search, March 2000
- [pro01] Update of the proposal to the lngs for a second phase of the cress dark matter search, February 2001
- [Prö02] F. Pröbst, private communication, 2002
- [Raf97] G.G. Raffelt, *Proceedings of the 1997 European School of High-Energy Physics*, Eprint hep-ph/9712538
- [Rei85] F. Reif, *Statistische Physik und Physik der Wärme*, de Gruyter, 1985
- [Rub82] V.C. Rubin, W.K. Ford, Jr., N. Thonnard, D. Burnstein, *Astrophys. J.* **261** (1982) 439
- [Sal97] P. Salucci, A. Sinibaldi, *Astron. Astrophys.* **(323)** (1997) 1
- [Sar96] S. Sarkar, *Rep. Prog. Phys.* **(59)** (1996) 1493

- [Sch96] J. Schnagl, Master's thesis, Technische Universität München, 1996
- [Sch98] D.N. Schramm, M. Turner, *Rev. Mod. Phys.* **(70)** (1998) 303
- [Sch99] R. Schnee, at TAUP conference, 1999
- [Sch01] J. Schnagl, PhD thesis, Technische Universität München, 2001
- [Sis99] M. Sisti, PhD thesis, Ludwig-Maximilians-Universität München, 1999
- [Sis01] M. Sisti et al., *Nucl. Inst. Meth. A* **466** (2001) 499–508
- [Sta] M. Stark, PhD thesis, Technische Universität München, in preparation
- [Sta01] M. Stark, 2001, private communication
- [Ste02] F. Steinbügel, Master's thesis, Technische Universität München, 2002
- [Sto01] R. Stompor et al., *Astrophys. J. Lett.* **(561)** (2001) L7–L10
- [Str01] R. Strharsky, 2001, private communication
- [Tam84] S. Tamura, *Phys. Rev. B* **30** (1984) 849
- [Tam85a] S. Tamura, *Phys. Rev. B* **31** (1985) 2574
- [Tam85b] S. Tamura, H.J. Maris, *Phys. Rev. B* **31** (1985) 2595
- [Tie90] U. Tietze, Ch. Schenk, *Halbleiterschaltungstechnik*, Springer, 1990
- [Tie01] W.M. Bergmann Tiest et al., In *LTD-9 conference proceedings*, Seite 199, 2001
- [Tin79] M. Tinkham, *Introduction to Superconductivity*, R.E. Krieger Publishing Company, 1979
- [Tre79] S.D. Tremaine, J.E. Gunn, *Phys. Rev. Lett.* **(42)** (1979) 407
- [Tri73] B.B. Triplett et al., *J. of Low Temp. Phys.* **12** (1973) 499
- [Tri87] V. Trimble, *Ann. Rev. Astron. Astrophys.* **25** (1987) 425
- [Web00] M.F. Weber et al., *SCIENCE* **(287)** (2000) 2451–2456
- [Zwi33] F. Zwicky, *Helv. Phys. Acta.* **(6)** (1933) 110

# Danksagung

Prof. Dr. Norbert Schmitz danke ich für die Möglichkeit meine Doktorarbeit im Rahmen des CRESST Experiments anfertigen zu können.

Besonderer Dank gilt Dr. Franz Pröbst für die Betreuung und sein stetes Interesse am Fortschreiten der Arbeit. Seine Erfahrung und sein Wissen waren immer von unschätzbarem Wert für mich.

Dr. Wolfgang Seidel hatte immer wieder gute Tips bezüglich Technik und Physik parat. Ausserdem machte er mit dem fristgerechten Umzug des Experiments das schier Unmögliche möglich. Dies erlaubte noch einige letzte Messungen am Gran Sasso vor dem Ende dieser Doktorarbeit. Dafür herzlichen Dank.

Meine Komplizen Cristina, Stefan, Antonio, Federica & Jelena beim täglichen Experimentieren sorgten für so manches Aha-Erlebnis sowie gelungenen Versuch und sind somit mitverantwortlich für das Gelingen dieser Arbeit. Danke und weiterhin viel Erfolg.

Allen weiteren derzeitigen, ehemaligen und „beinahe“ Mitgliedern der CRESST Gruppe Manfred, James, Gode, Peter, Hans S., Dieter, York, Hans K., Philippe, Sergey, Daniele, Dušan, Michi A., Thomas für die Hilfe, Diskussionen, Keks & Kuchen Versorgung, W/Al/Au -Filme, außerphysikalische Aktivitäten, Witze, Fragen, gute Atmosphäre ... vielen Dank.

Den Werkstätten des MPIs herzlichen Dank für die (oft kurzfristige) Herstellung meiner manchmal fertigungsunfreundlichen (Fehlkonstruktionen?) Teile.

Den E15ern Michi S., Michi H., Thomas, Tobi, Josef vielen Dank für die Zusammenarbeit und Hilfe während der letzten drei Jahre.

Matthias, Thomas, Birgit, Stefan, Paul mussten sich vor allem gegen Ende immer wieder ungefragt „doktorarbeitstechnische“ Probleme anhören. Danke für die Geduld und die aufmunternden Worte.

Den Korrekturen ein extra Dankeschön ...

Und ein ganz besonderer Dank geht an meine Eltern für ihre Unterstützung und Geduld, bis der Junge endlich nach seiner Ausbildung auf eigenen Füßen steht.

✂